Mechanisms and Sources of Mantle Metasomatism: Major and Trace Element Compositions of Peridotite Xenoliths from Spitsbergen in the Context of Numerical Modelling

DMITRI A. IONOV[1,2]*, JEAN-LOUIS BODINIER[3], SAMUEL B. MUKASA[4] AND ALBERTO ZANETTI[5]

[1]DEPARTMENT OF EARTH AND ENVIRONMENTAL SCIENCES, UNIVERSITÉ LIBRE DE BRUXELLES, CP160/02, B-1050 BRUSSELS, BELGIUM

[2]DEPARTMENT OF GEOLOGY, NIIGATA UNIVERSITY, 2-8050 IKARASHI-NINOCHYO, NIIGATA, 950-2181, JAPAN

[3]LABORATOIRE DE TECTONOPHYSIQUE (UMR 5568 CNRS), ISTEEM, UNIVERSITÉ MONTPELLIER 2, CASE 049, 34095 MONTPELLIER CEDEX 05, FRANCE

[4]DEPARTMENT OF GEOLOGICAL SCIENCES, UNIVERSITY OF MICHIGAN, ANN ARBOR, MI 48109-1063, USA

[5]CNR–ISTITUTO DI GEOSCIENCE E GEORISORSE (IGG), SEZIONE DI PAVIA, 27100 PAVIA, ITALY

Mineral and whole-rock chemical data for peridotite xenoliths in basaltic lavas on Spitsbergen are examined to reassess mechanisms of melt–fluid interaction with peridotites and their relative role versus melt composition in mantle metasomatism. The enrichment patterns in the xenoliths on primitive mantle-normalized diagrams range from Th–La–Ce 'inflections' in weakly metasomatized samples (normally without amphibole) to a continuous increase in abundances from Ho to Ce typical for amphibole-bearing xenoliths. Numerical modelling of interaction between depleted peridotites and enriched melts indicates that these patterns do not result from simple mixing of the two end-members but can be explained by chromatographic fractionation during reactive porous melt flow, which produces a variety of enrichment patterns in a single event. Many metasomatized xenoliths have negative high field strength element and Pb anomalies and Sr spikes relative to rare earth elements of similar compatibility, and highly fractionated Nb/Ta and Zr/Hf. Although amphibole precipitation can produce Nb–Ta anomalies, some of these features cannot be attributed to percolation-related fractionation alone and have to be a signature of the initial melt (possibly carbonate rich). In general, chemical and mineralogical fingerprints of a metasomatic medium are strongest near its source (e.g. a vein) whereas element patterns farther in the metasomatic 'column' are increasingly controlled by fractionation mechanisms.

KEY WORDS: *Spitsbergen; lithospheric mantle; metasomatism; trace elements; theoretical modelling*

INTRODUCTION

Peridotite xenoliths brought to the surface by alkali basaltic magmas on the island of Spitsbergen represent continental upper mantle located at present in the vicinity of oceanic spreading centres in the North Atlantic and Arctic basins. Much of the earlier work on these xenoliths focused on carbonates and related interstitial phases believed to have formed as a result of interaction between

*To whom correspondence should be addressed at present address: Laboratoire de Tectonophysique, ISTEEM, CNRS & Université Montpellier 2, case 049, 34095 Montpellier cedex 05, France. Telephone: +33-467143602. Fax: +33-467143603. E-mail: ionov@dstu.univ-montp2.fr

mantle rocks and carbonate-rich melts during entrainment and transportation to the surface by the host magmas (Amundsen, 1987; Genshaft & Ilupin, 1987; Ionov *et al.*, 1993*b*, 1996). The interstitial carbonates, which are rare in mantle xenoliths elsewhere, attracted particular attention as direct evidence for carbonate-rich melts in the mantle. In particular, trace element compositions of acid-leached interstitial material from several xenoliths (Ionov *et al.*, 1993*b*) and *in situ* analyses of carbonates and associated interstitial clinopyroxene and silicate glass (Ionov *et al.*, 1996; Ionov, 1998) were used to infer geochemical signatures of mantle metasomatism by carbonate-rich fluids.

Previous studies have also addressed the petrography of the xenoliths and provided a limited amount of data on the compositions of minerals apparently unrelated to the late-stage interstitial material (Furnes *et al.*, 1986; Ionov *et al.*, 1996). Analyses of coarse clinopyroxene grains by proton probe (Ionov *et al.*, 1996) indicated metasomatic enrichments in Sr. Furthermore, laser-ablation microprobe (LAM) inductively coupled plasma mass spectrometry (ICP-MS) analyses in three samples showed that abundances and elemental ratios in the coarse clinopyroxene are distinct from those in clinopyroxene from interstitial carbonate- and glass-bearing pockets (Ionov, 1998). Some xenoliths were found to contain texturally equilibrated amphibole, apatite and phlogopite (Ionov *et al.*, 1993*b*, 1996). Altogether, the earlier work has yielded unequivocal petrographic and chemical evidence for modal and cryptic metasomatism that took place before the formation of the silicate glass and carbonate-bearing material. However, the data are not sufficient to unravel the nature and evolution of the mantle beneath Spitsbergen.

In this work we establish major and trace element signatures of the peridotite mantle beneath Spitsbergen through analysis of whole-rock xenoliths and of minerals that largely control the incompatible trace element inventory in the mantle. These data, together with theoretical modelling, are used to understand the sequence of upper-mantle processes recorded in the xenolith suite. The major goal of this study is to further constrain mechanisms of mantle metasomatism and define the nature and sources of the metasomatic components responsible for enrichment of the lithospheric mantle in incompatible elements. We focus on characterizing metasomatic and other events that pre-date those related to the late Cenozoic volcanic activity that brought the xenoliths to the surface.

Petrographic and chemical studies of mantle rocks worldwide have found a variety of mineralogical associations and trace element enrichment patterns that appear to result from interaction of depleted peridotites with magmas and fluids (e.g. Frey & Green, 1974; Menzies & Hawkesworth, 1987; McDonough & Frey, 1989;

Bodinier *et al.*, 1990; Johnson *et al.*, 1996; Mukasa & Wilshire, 1997; Yaxley *et al.*, 1998; Ionov *et al.*, 1999*a*). It has become apparent that the enrichment phenomena generally referred to as mantle metasomatism may be implemented through a large number of processes (e.g. batch crystallization, melt fractionation in conduits and chambers, melt or fluid percolation). These mechanisms can be identified and constrained based on trace element distributions in natural samples compared with results of theoretical modelling.

Another widely debated topic of mantle geochemistry is the provenance (sources) of melts and fluids responsible for metasomatism in the continental mantle. It has been suggested that the metasomatic media may originate within the lithospheric mantle, convecting asthenospheric mantle, deep-mantle plumes, or subducted oceanic lithosphere (Beccaluva *et al.*, 2001; Churikova *et al.*, 2001; Downes, 2001 and references therein). Furthermore, mantle metasomatism may involve a variety of media (silicate and carbonate melts, water- and CO_2-rich fluids) that are derived from different sources. Particular attention has recently been given to metasomatism by carbonate-rich melts, which seem to have a strong enrichment potential and impose specific trace element signatures (e.g. Green & Wallace, 1988; Yaxley *et al.*, 1991; Dautria *et al.*, 1992; Hauri *et al.*, 1993; Ionov *et al.*, 1993*b*; Rudnick *et al.*, 1993; Downes, 2001).

Overall, mantle metasomatism has been attributed to a variety of: (1) processes, (2) sources, and (3) melt–fluid compositions. Which factors dominate in creating specific metasomatic signatures in the continental lithospheric mantle remains widely debated. For example, trace element patterns earlier seen as evidence for metasomatism by carbonate-rich melts have been recently interpreted as source signatures or the result of fractionation processes (Bedini *et al.*, 1997; Blundy & Dalton, 2000; Laurora *et al.*, 2001). Addressing these complex issues necessitates comprehensive geochemical investigation of a representative sample series, which has been undertaken in this study, and in the accompanying paper that addresses Sr–Nd–Pb isotope composition of the same sample series (Ionov *et al.*, 2002).

GEOLOGICAL SETTING

Spitsbergen is the largest island of the Svalbard archipelago off Norway, which is the subaerially exposed corner of the Barents–Kara shelf between the North Atlantic and Arctic (Eurasian) oceanic basins (Fig. 1a). Tectonic reconstructions indicate that Svalbard was contiguous with Greenland until the northward progression of the North Atlantic opening produced Late Cretaceous–Neogene separation of Eurasia and North America (Blythe & Kleinspehn, 1998). At present, Spitsbergen is
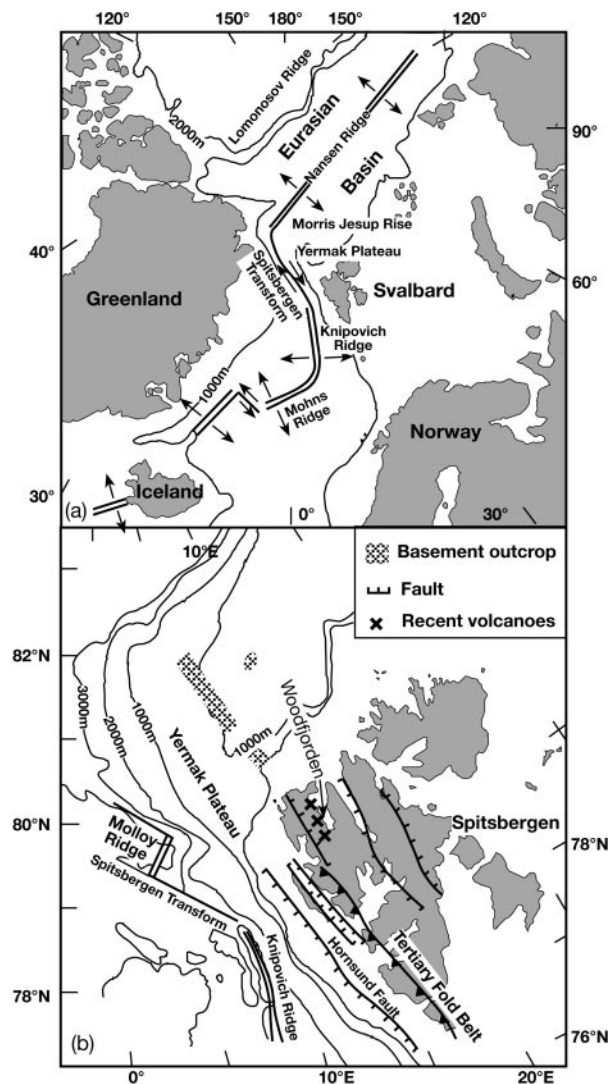
Fig. 1. A sketch map of the North Atlantic (a) and Svalbard Archipelago (b) showing major tectonic features and location of the recent volcanoes sampled for xenoliths and basalts [modified from Amundsen *et al.* (1987)].

located at a distance <200 km from the North Atlantic mid-ocean ridge (MOR) (Fig. 1b).

The xenoliths for this study have been collected in hawaiitic to nepheline basanitic lavas at three Quaternary volcanic centres on the western side of Woodfjorden in NW Spitsbergen (Fig. 1b): Sverre, Halvdan and Sigurd. Tholeiitic lavas, 9–12 Myr old, from nearby areas do not contain mantle xenoliths. Relevant data on geology, tectonic setting and geophysical results for this region have been summarized by Amundsen *et al.* (1987) and Yevdokimov (2000). Additional information on xenoliths from these localities has been provided by Furnes *et al.* (1986), Genshaft *et al.* (1992) and Ionov *et al.* (1996).

SAMPLE PREPARATION AND ANALYTICAL PROCEDURES

Samples for this study were selected from a larger collection (Yevdokimov, 2000) to represent major peridotite rock types and modal variations. We have also tried to select fresh xenoliths that are large enough to prepare representative whole-rock samples and provide material for mineral separation. The samples are listed in Table 1, along with a summary of the petrography, modal compositions, geothermometry and other information on the analyses performed.

The xenoliths were cut using a diamond saw; central parts containing no host basalt or saw marks were crushed in a bench-top jaw crusher, which was carefully cleaned after each sample to avoid cross-contamination. Aliquots of the crushed samples were ground in an agate mortar to produce whole-rock powders. Another aliquot was sieved, size-fractioned and magnetically separated to yield sub-fractions enriched in clinopyroxene and amphibole. Ultrapure mineral separates were handpicked from these for isotope analyses (Ionov *et al.*, 2002). Several hand-picked grains (≥ 0.2–0.3 mm) from each sample were put on mounts for *in situ* analyses. The handpicked clinopyroxene grains are larger than clinopyroxene from interstitial carbonate- and glass-bearing material (Fig. 2a); the latter are therefore absent from the grain mounts. Samples of host basalts were sawn off from lava attached to the xenoliths. Basalt chips free of saw marks, weathering products and xenocryst material were leached in 6 M HCl and ground to powder in an agate mortar.

Major elements in bulk rocks were determined by X-ray fluorescence (XRF) spectrometry at Niigata University using low-dilution fused beads [see Takazawa *et al.* (2000) for analytical details] and at Michigan State University following standard protocols. Major-element compositions of minerals were determined in thin sections with a Cameca Camebax SX-50 electron microprobe (EMP) at Macquarie University, Sydney [for analytical details see Ionov *et al.* (1996)] and with Camebax SX-100 at Université Blaise Pascale, Clermont-Ferrand, France. Modal compositions were calculated from whole-rock and mineral major-element analyses using least-squares regression.

Trace elements in whole-rock peridotites were determined by solution ICP-MS at Niigata University; basalts were analysed at CODES (Hobart). At both laboratories, the instrument was an HP4500; calibration was performed against BHVO-1 using values of Eggins *et al.* (1997). As, Rh, In, Tm and Bi were used as internal standards. Several peridotites (including duplicates and acid-leached rocks) were analysed on a VG PlasmaQuad instrument in Montpellier following the method of Ionov *et al.* (1992). Reference samples BIR-1 and JP-1

Table 1: Sample list and information summary for the xenoliths

Sample no.	Location	Texture or rock type	ol	opx	cpx	spl	amph	Access. minerals	Wells	Ca-opx	Mg# in ol	Cr# in spl	LAM ICP-MS	WR ICP-MS	Sr–Nd–Pb isotopes	Enrichment type
21-5*	Halvdan	Crs					n.d.	ap, cb	900	915–930	0·914	0·236	cp, amph			2
21-6*	Halvdan	Crs					n.d.	ap, cb	944	925	0·912	0·221	cp, amph†			2
311-9	Halvdan	Mos-Eq to Crs	69·6	18·5	8·5	2·0	1·4‡		970	945	0·907	0·181	cp	+	cp	2
315-6	Halvdan	Crs-Prb	60·4	25·5	9·8	1·7	2·4	(cb)	860	890	0·904	0·124	cp, amph	+	cp, amph	1
318	Halvdan	Mos-Prb	79·4	12·3	3·0	1·1	4·2	(cb)	900	930–960	0·915	0·253	cp, amph	+	cp, amph	2
318-1	Halvdan	Crs	60·2	25·1	12·1	1·6	1·0		1035	1025	0·908	0·164	cp, amph	+	cp	2
4-90-9	Halvdan	Crs to Mos-Eq					n.d.	(cb)	980	990	0·897	0·162	cp, amph†			2
4-25-90	Halvdan	Crs to Mos-Eq	75·4	11·3	10·6	2·7	—	cb	970	1000–1015	0·910	0·204	cp	+	cp	1
4-36-90*	Halvdan	Crs to Mos-Eq	74·0	13·2	10·1	2·7	—	cb	910	950–965	0·906	0·170	cp†	+	cp	1
25	Sverre	Crs-Mos					—	cb	870	900	0·899	0·118		+		1
26a	Sverre	Crs-Prb	69·6	26·5	2·9	1·0	—	(cb)	740	1000/800	0·912	0·416	cp	+	cp	—
28b	Sverre	Crs to Mos-Prb	63·6	27·4	7·5	1·5	—	(cb)	910	940	0·905	0·133		+		1
39-86-1	Sverre	Crs to Mos-Prb	69·5	18·2	10·0	2·3	—	(cb)	—	887	0·906	0·135	cp		cp	—
39-86-2	Sverre	Crs to Mos-Prb	68·2	17·3	11·3	3·2	—	(cb)	940	930	0·905	0·125	cp		cp	1
63-90-18	Sverre	Crs to Mos-Prb	59·4	28·6	10·1	1·8	—	(cb)	840	895–910	0·901	0·136	cp		cp	1
63-90-30	Sverre	Prb	69·5	20·0	8·8	1·7	—		895	950	0·911	0·279	cp		cp	—
4-90-1	Sigurd	amph wehrlite						phl			0·890		cp, phl amph		cp, phl amph	vein
1-25-90	Halvdan	host basalt												+	WR	
3-15-90	Halvdan	host basalt												+	WR	
35	Sverre	host basalt												+	WR	

*See mineral EMP analyses of Ionov *et al.* (1996).

†See LAM-ICP-MS analyses of Ionov (1998).

‡Amphibole breakdown products.

Mg#, atomic Mg/(Mg + Fe); Cr#, atomic Cr/(Cr + Al); Crs, coarse; Mos, mosaic; Eq, equigranular; Prb, porphyroblastic; amph, amphibole; ap, apatite; cb, carbonate; cpx, clinopyroxene; ol, olivine; opx, orthopyroxene; phl, phlogopite; spl, spinel; WR, whole rock; n.d., not determined. Samples 4-25-90, 4-36-90 and 25 have highest abundances of interstitial carbonate (probably 0·5–1%); other samples contain trace amounts of carbonates (cb) and their alteration products. Modal compositions were calculated from whole-rock and mineral analyses by least-squares method. Temperature estimates are after Wells (1977) and the Ca-opx method of Brey & Köhler (1990). Core and rim *T* values, respectively, are given for xenoliths with Ca zoning in orthopyroxene. Enrichment types in the peridotites are defined based on trace element patterns specific to this xenolith suite (see text) and do not refer to rock types defined in classifications of Frey & Prinz (1978) and Kempton (1987).
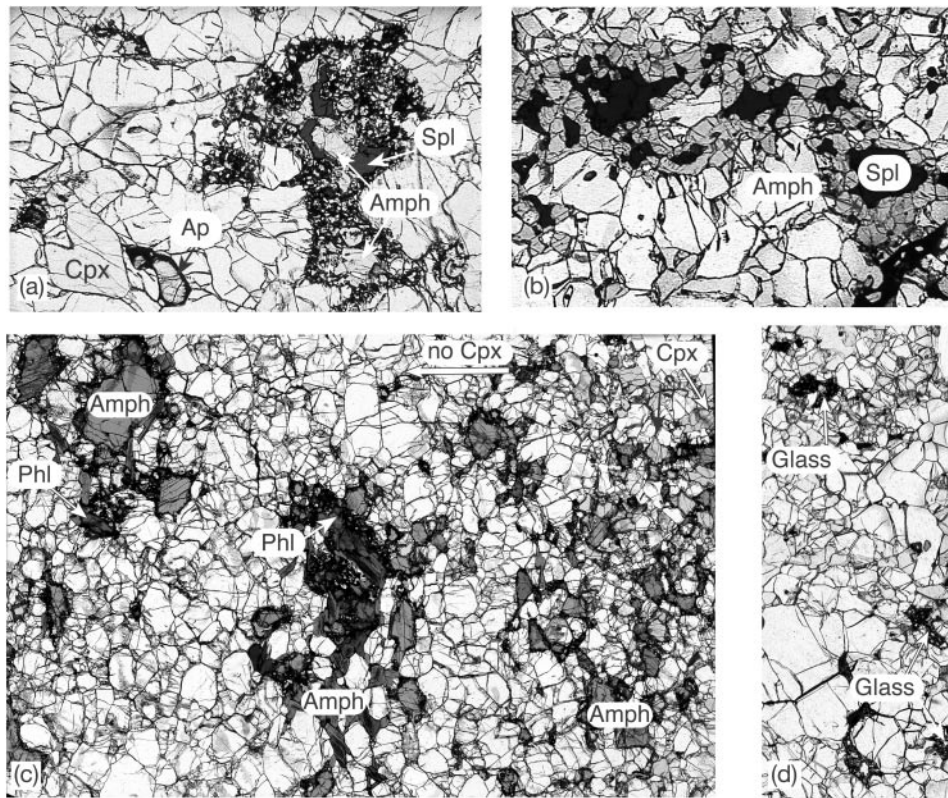
Fig. 2. Photomicrographs of Spitsbergen xenoliths in plane-polarized transmitted light. (a) Relict amphibole (Amph) in a vesicular aggregate of silicate glass, fine-grained olivine (ol), clinopyroxene (Cpx) and Cr-spinel (Spl). An apatite (Ap) grain and the large size and lack of alteration in primary clinopyroxene should be noted. Sample 21-6; field of view is 5 mm. (b) Amphibole mantling spinel in sample 318; field of view is 5 mm. (c) Mineralogical variation in composite xenolith 4-90-1. About a quarter of the field of view (4 cm) on the right is amphibole wehrlite, which grades into coarse olivine matrix with clusters of amphibole and phlogopite (Phl). No spinel or orthopyroxene has been found in this sample. (d) Small pockets of vesicular glass–cpx–ol–spl aggregates (dark) in sample 311-9 considered to be breakdown products of pre-existing amphibole; field of view is 10 mm along the long axis.

(Makishima & Nakamura, 1997) were analysed as unknowns for quality control. Trace elements in minerals were determined by LAM-ICP-MS in grain mounts and polished rock sections of 200 μm thickness in Sydney and Pavia. The instrument at Macquarie University is a Perkin–Elmer Sciex ELAN 5100 coupled with a UV (266 nm) laser [see Norman *et al.* (1996) and Ionov (1998) for details of operating conditions]. The instrument at the CNR–IGG of Pavia is a double focusing sector field analyser ('Element' Finnigan Mat) coupled with a Q-switched Nd:YAG laser source (Quantel Brilliant), whose fundamental emission in the near-IR region (1064 nm) is converted to 266 nm by two harmonic generators (Bottazzi *et al.*, 1999). Helium was used as carrier gas and mixed with Ar downstream of the ablation cell. A BCR2-g reference sample was used as an external standard, with ^{44}Ca as an internal standard for clinopyroxene and amphibole and ^{29}Si for phlogopite. Precision and accuracy (<10% and <5%, respectively) were assessed from repeated analyses of SRN NIST 612 reference sample. Trace elements were also determined in profiles across clinopyroxene and amphibole grains by SIMS (secondary ion mass spectrometry) on Cameca 4f instruments in Pavia and Montpellier following procedures reported by Bottazzi *et al.* (1994).

PETROGRAPHY AND MAJOR ELEMENT COMPOSITIONS
Petrography
Most of the xenoliths from Halvdan and Sverre are medium- to coarse-grained spinel lherzolites with low to moderate modal clinopyroxene (Table 1). Samples 26a and 318 have <3% clinopyroxene and are therefore classified as harzburgites (Streckeisen, 1976). Many of the Halvdan xenoliths contain amphibole (Table 1), whose modal abundance ranges from rare individual grains to >4%. Amphibole in samples 318 and 315-6 has textural position, grain size and shape similar to those of neoblast olivine and pyroxenes. It does not

appear to replace clinopyroxene or spinel because, in particular, spinel abundances in amphibole-rich peridotites are not noticeably lower than in amphibole-poor samples (Fig. 2b). A single sample from Sigurd (4-90-1) is a composite xenolith of amphibole wehrlite (spinel-free) grading into a coarse-grained olivine-dominated rock that contains clusters of amphibole and less abundant phlogopite in an olivine matrix (Fig. 2c). Two Halvdan xenoliths (too small for mineral separation) contain apatite in addition to amphibole (Fig. 2a). Fe–Ni sulphides are common accessory minerals. The petrography of these rocks has been presented in more detail by Ionov et al. (1996).

Some of the peridotites contain interstitial veins and pockets of fine-grained material made of silicate glass, carbonate and second-generation clinopyroxene, olivine and Cr-spinel, enclosing resorbed relict grains of minerals of the host peridotite (Fig. 2a). This late-stage fine-grained material is not considered in this work, and readers are referred to Ionov (1998) for more information. Sample 311-9 has pockets of silicate glass with micro-phenocrysts and vugs associated with spinel (Fig. 2d); no amphibole is present in the thin section available. The shapes and textural position of the glassy pockets resemble those of amphibole mantling spinel in some other Spitsbergen xenoliths; similar pockets in samples 21-5 and 21-6 enclose resorbed amphibole relics (Fig. 2a) (Ionov et al., 1996). It is most likely that xenolith 311-9 originally contained some amphibole, which broke down shortly before or during the eruption of the host basalts, as has also been inferred for certain types of glass-bearing pockets in mantle xenoliths worldwide (e.g. Yaxley et al., 1997). We therefore classify sample 311-9 as amphibole-bearing to properly characterize its modal composition before the late-stage melting events.

Whole-rock compositions

Whole-rock major element compositions are given in Table 2 and illustrated in Fig. 3. The xenolith suite can generally be characterized as moderately depleted in basaltic components (Al, Ca, Na, Ti). Most of the samples plot in the middle of compositional fields of basalt-borne, off-cratonic peridotite xenoliths and massif peridotites worldwide on covariation plots vs MgO and Mg# [molar Mg/(Mg + Fe) ratio] (Fig. 3; McDonough, 1990). Two samples (including an amphibole-rich peridotite) have high MgO and low CaO and Al_2O_3 similar to some xenoliths from kimberlites; however, they differ from typical cratonic mantle peridotites by higher FeO and lower Mg# (Fig. 3a and b). A few samples plot above the MgO–CaO trend on Fig. 3c, consistent with the presence of <1% of Ca-rich interstitial carbonate indicated by earlier studies (Ionov et al., 1996). Carbonate-poor sample 63-90-30 shows a very high molar Ca/Al

ratio of 1·65 compared with a range of 1·0–1·2 typical for the spinel lherzolites (Table 2). The composition of Fe-rich sample 39-86-1 is distinct from that of a duplicate sample (39-86; Figs 3a and b, and 4a) prepared from the same xenolith (Ionov et al., 1996) indicating rock heterogeneity.

Mineral compositions and temperature estimates

Major element compositions of minerals are given in Table 3. Values of Mg# in olivine ($Mg\#_{Ol}$) are tightly correlated with Mg# in whole rocks (Fig. 4a) and show a general positive trend with the Cr/(Cr + Al) ratios of spinel ($Cr\#_{Spl}$) (Fig. 4b). Most of the Spitsbergen samples on the latter diagram plot between the tight field of fertile (Mg# <0·90) xenoliths and highly depleted xenoliths from East Greenland and abyssal peridotites, consistent with partial melting relationships (Bernstein et al., 1998; Hellebrand et al., 2001). Sample 26a, which has the highest $Cr\#_{Spl}$, plots with off-cratonic xenoliths that show a wide range of $Cr\#_{Spl}$ at moderately high $Mg\#_{Ol}$ (0·90–0·915; Fig. 4b). In some xenoliths from Spitsbergen (and Samoa), the $Cr\#_{Spl}$ values are higher, at a given Cr_2O_3 content in clinopyroxene, than in other mantle peridotites (Fig. 4c).

The abundances of Ti, Al and Na in clinopyroxene are shown in Fig. 4d–f vs $Mg\#_{Ol}$. Olivine hosts 72–90% of Mg and Fe in the xenoliths and therefore its Mg# established during partial melting is less affected by posterior temperature-dependent sub-solidus inter-mineral Mg–Fe partitioning (Brey & Köhler, 1990) than the Mg# of pyroxenes. The abundances of Ti and Al in clinopyroxene in the majority of the samples are negatively correlated with the $Mg\#_{Ol}$ (Fig. 4d and e). By contrast, Na_2O contents are nearly the same (1·0–1·5%) and are higher than for abyssal peridotites and xenoliths from Samoa at similar $Mg\#_{Ol}$ (Fig. 4f). Clinopyroxene in 26a has much lower abundances of Na, Al and Ti than in the rest of the xenoliths. Amphibole wehrlite 4-90-1 plots away from spinel peridotites in Fig. 4 because of its low Mg# and high TiO_2 in clinopyroxene.

The Mg# values of amphibole show a near-linear correlation with the $Mg\#_{Ol}$. The Cr abundances in amphibole are positively correlated with the $Cr\#_{Spl}$ (Fig. 5a and b). These and other results indicate that amphibole in all of the samples is chemically equilibrated with the other minerals. In comparison, the abundances of K and Ti, minor elements strongly concentrated in the amphibole, are poorly correlated (Fig. 5d). Most amphiboles have low K_2O (<1%), particularly 315-6 (0·02%).

Equilibration temperature estimates calculated from the electron microprobe data using methods of Wells

Table 2: *Whole-rock compositions determined by XRF (wt %)*

	26a	311-9	315-6*	318	318-1*	39-86-1*	39-86-2	4-25-90	63-90-30	28b	4-36-90	63-90-18	Basalt
SiO_2	45·04	43·52	44·81	42·73	44·94	42·90	43·51	42·16	44·02	44·27	42·71	45·03	46·12
TiO_2	0·01	0·06	0·077	0·06	0·074	0·064	0·11	0·1	0·12	0·06	0·07	0·08	2·62
Al_2O_3	1·00	2·15	2·83	1·55	2·92	2·42	2·88	2·17	1·57	2·27	2·36	2·65	14·34
FeO	7·37	7·90	8·00	7·39	7·64	8·24	7·83	7·43	7·59	8·02	7·69	8·01	10·02
MnO	0·12	0·13	0·13	0·12	0·13	0·13	0·13	0·13	0·12	0·12	0·12	0·13	0·16
MgO	43·90	42·27	40·89	45·15	40·78	41·90	41·42	42·99	42·54	42·60	43·19	40·83	9·23
CaO	0·81	1·95	2·60	1·16	2·74	2·20	2·38	2·18	1·92	1·82	2·28	2·36	8·69
Na_2O	n.d.	n.d.	0·20	n.d.	0·22	n.d.	n.d.	n.d.	n.d.	n.d.	0·20	0·25	5·12
K_2O	0·02	0·01	0·004	0·02	0·006	0·010	0·00	0·01	0·00	0·00	0·01	0·00	1·78
P_2O_5	0·00	0·02	0·015	0·04	0·032	0·013	0·01	0·01	0·01	0·00	0·01	0·00	0·73
Cr_2O_3	n.d.	n.d.	0·36	n.d.	0·46	0·37	n.d.	n.d.	n.d.	n.d.	n.d.	n.d.	0·03
NiO	n.d.	n.d.	0·27	n.d.	0·26	0·29	n.d.	n.d.	n.d.	n.d.	n.d.	n.d.	0·01
Total	98·27	98·01	100·18	98·22	100·19	98·74	98·27	97·18	97·89	99·16	98·61	99·34	98·85
Mg#	0·914	0·905	0·901	0·916	0·905	0·901	0·904	0·912	0·909	0·904	0·909	0·901	0·621
Ca/Al_{at}	1·09	1·22	1·24	1·01	1·27	1·23	1·12	1·36	1·65	1·08	1·31	1·20	

Analyses of samples 28b, 4-36-90, and 63-90-18 are from Ionov *et al.* (1996); analysis of Sverre basalt is from Furnes *et al.* (1986). n.d., not determined.
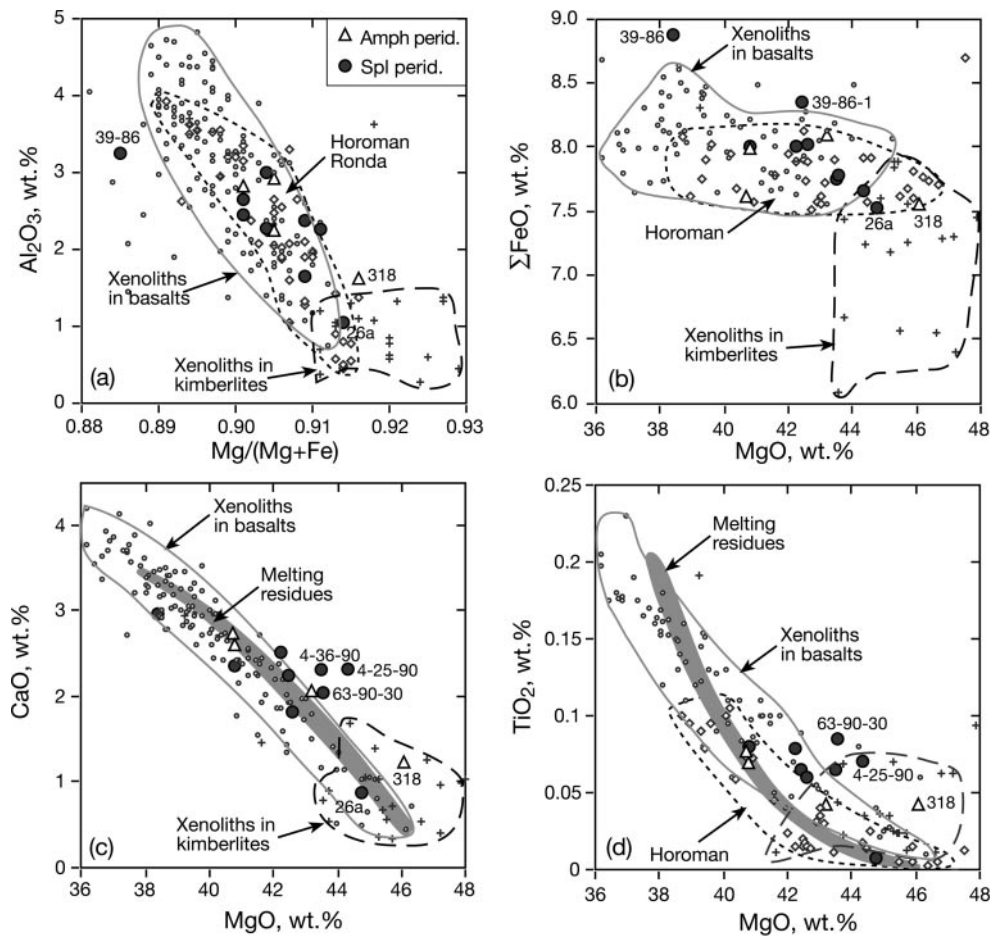*Niigata analyses.

Fig. 3. Major element variations in Spitsbergen whole-rock xenoliths. Oxide contents are in weight percent (normalized to 100% total). △, amphibole-bearing peridotites; ●, 'anhydrous' peridotites. Shown for comparison as grey symbols are xenoliths in basalts from Siberia and Mongolia (small open circles), xenoliths in Yakutian kimberlites (crosses) and peridotites from Horoman and Ronda massifs (small rhombs). Continuous grey line outlines typical compositions of xenoliths in basalts; dashed lines contour typical compositions of xenoliths in kimberlites and massif peridotites. Shaded fields in (c) and (d) show chemical trends calculated for residues from fractional partial melting of fertile spinel lherzolites (Niu, 1997). Data sources: Frey *et al.* (1985), Ionov (1986), Press *et al.* (1986), Ionov *et al.* (1993*a*, 1999*b*), Boyd *et al.* (1997), Wiechert *et al.* (1997), Takazawa *et al.* (2000) and unpublished data of D. A. Ionov (2000).

(1977) and Brey & Köhler (1990) are listed in Table 1. The values for the Halvdan xenoliths seem to be generally higher than those for the Sverre xenoliths, but this difference may not be meaningful considering the small number of samples analysed. Our T estimates (840–1030°C) are much lower than the range of 940–1170°C reported for Spitsbergen spinel lherzolites by Amundsen *et al.* (1987). We failed to obtain T values >1080°C applying the same thermometer (Sachtleben & Seck, 1981) to samples in this study or published data (Furnes *et al.*, 1986). Projection of our T estimates onto the geotherm for northwestern Spitsbergen after Amundsen *et al.* (1987) yields unrealistically low pressures of 7–11 kbar. We conclude that the above geotherm overestimates temperatures in the uppermost mantle, apparently because of the use of inappropriate thermometers. We

have roughly estimated equilibration pressures for the lherzolites in this study (11–15 kbar) by projecting their Ca-opx T range (890–1025°C) onto a P–T trend calculated by applying the same thermometer (Brey & Köhler, 1990) and relevant barometers to published electron microprobe analyses of garnet-bearing pyroxenites from Spitsbergen (Amundsen *et al.*, 1987).

Minerals in most samples show no, or only limited, chemical zoning. In several xenoliths, pyroxene rims have lower Al and Cr than the cores. Harzburgite 26a has particularly strong Al–Cr zoning and low Al in pyroxenes (coupled with Cr-rich spinel, Fig. 4b) and a very high Mg# in clinopyroxene relative to that in olivine and orthopyroxene. Because Fe–Mg partitioning between olivine and pyroxenes is temperature dependent, the high Mg# in clinopyroxene may be related to the very low

Table 3: Electron microprobe concentration data for minerals (in wt %); data are for mineral cores unless otherwise specified

4-90-9 (Halvdan)

	Opx c. av. of 3	Opx r. av. of 7	Cpx c. av. of 2	Cpx r. av. of 3	Ol av. of 2	Spl av. of 2	Amph av. of 4
SiO_2	55·07	54·91	52·15	52·11	40·71	0·03	42·70
TiO_2	0·04	0·06	0·16	0·19		0·07	1·30
Al_2O_3	4·10	4·22	5·56	5·72		50·92	14·34
Cr_2O_3	0·41	0·39	0·85	0·85		14·69	1·35
FeO	6·34	6·17	3·07	3·15	10·03	12·51	4·34
MnO	0·15	0·15	0·08	0·08	0·14		0·05
MgO	32·97	32·83	15·59	15·55	48·96	19·53	17·41
CaO	0·76	0·78	20·34	20·26	0·06		10·61
Na_2O	0·09	0·10	1·44	1·41			3·32
K_2O							0·80
NiO	n.d.	n.d.			n.d.	n.d.	
Total	99·93	99·59	99·23	99·32	99·90	97·74	96·21
Mg#	0·903	0·905	0·901	0·898	0·897	0·736	0·877

311-9 (Halvdan)

	Opx c. av. of 3	Opx r.	Cpx c. av. of 3	Ol av. of 3	Spl	Glass
SiO_2	56·23	55·67	52·89	41·32	0·01	65·21
TiO_2	0·05	0·01	0·19		0·08	0·39
Al_2O_3	3·51	3·61	4·98		50·10	18·92
Cr_2O_3	0·36	0·46	0·77		16·48	0·06
FeO	5·71	5·58	2·49	9·23	11·16	1·82
MnO	0·12	0·08	0·08	0·16		0·04
MgO	34·09	33·94	15·96	50·45	19·68	1·44
CaO	0·63	0·64	21·06			5·71
Na_2O	0·06	0·05	1·17			3·20
K_2O						1·75
NiO	0·12	0·12	0·05	0·38	0·27	0·00
Total	100·88	100·14	99·63	101·55	97·78	98·53
Mg#	0·914	0·916	0·920	0·907	0·759	0·585

315-6 (Halvdan)

	Opx c. av. of 3	Opx r. av. of 2	Cpx c. av. of 3	Cpx r.	Ol	Spl av. of 2	Amph av. of 4
SiO_2	54·10	54·57	51·71	51·55	40·25	0·04	42·99
TiO_2	0·07	0·07	0·29	0·24		0·05	1·31
Al_2O_3	4·03	3·45	4·77	4·79		54·50	14·48
Cr_2O_3	0·38	0·24	0·63	0·70		11·48	1·08
FeO	6·16	6·26	2·58	2·54	9·31	11·55	4·05
MnO	0·14	0·11	0·08	0·04	0·15		0·05
MgO	33·33	33·61	15·59	15·41	48·92	20·33	17·55
CaO	0·47	0·50	22·03	21·86	0·03		11·12
Na_2O	0·04	0·06	1·13	1·12			3·63
K_2O							0·02
NiO	n.d.				n.d.	n.d.	
Total	98·73	98·85	98·82	98·25	98·66	97·93	96·27
Mg#	0·906	0·905	0·915	0·915	0·904	0·758	0·885

4-25-90 (Halvdan)

	Opx c. av. of 3	Opx r. av. of 3	Cpx c.	Cpx r.	Ol c. av. of 2	Spl c. av. of 2
SiO_2	55·50	55·60	52·47	52·28	40·85	0·08
TiO_2	0·06	0·05	0·23	0·27	0·05	0·12
Al_2O_3	4·03	4·09	4·94	5·40	0·03	48·13
Cr_2O_3	0·52	0·50	0·78	0·96		18·41
FeO	5·62	5·62	2·70	2·94	8·97	12·26
MnO	0·12	0·10	0·04	0·10	0·08	
MgO	33·77	33·76	16·27	15·98	50·76	19·89
CaO	0·81	0·87	20·97	20·89	0·10	
Na_2O	0·08	0·09	1·23	1·30		
K_2O						
NiO	n.d.	n.d.			n.d.	n.d.
Total	100·52	100·68	99·63	100·12	100·84	98·89
Mg#	0·915	0·915	0·915	0·906	0·910	0·743

318 (Halvdan)

	Opx c. av. of 2	Opx r. av. of 2	Cpx c. av. of 2	Cpx r.	Ol av. of 2	Spl av. of 2	Amph av. of 2
SiO_2	55·54	55·37	52·19	52·30	40·48		42·40
TiO_2	0·02	0·02	0·13	0·13		0·05	0·76
Al_2O_3	2·91	3·05	4·32	4·22		44·81	14·10
Cr_2O_3	0·35	0·47	0·95	0·92		22·60	1·73
FeO	5·31	5·36	2·29	2·23	8·33	11·66	3·23
MnO	0·13	0·15	0·08	0·06	0·10		0·02
MgO	34·38	34·25	15·76	15·93	50·41	19·06	17·73
CaO	0·58	0·67	21·41	21·53	0·04		11·14
Na_2O	0·07	0·08	1·24	1·23			3·20
K_2O							0·75
NiO	n.d.	n.d.			n.d.	n.d.	
Total	99·26	99·42	98·35	98·53	99·35	98·17	95·03
Mg#	0·920	0·919	0·925	0·927	0·915	0·745	0·907

318-1 (Halvdan)

	Opx c.	Cpx c. av. of 3	Ol	Spl	Amph av. of 2
SiO_2	55·72	52·69	40·65	0·07	42·99
TiO_2	0·08	0·29		0·13	1·40
Al_2O_3	4·71	6·14		51·12	14·75
Cr_2O_3	0·54	0·95		14·91	1·41
FeO	5·76	2·92	9·07	11·47	3·81
MnO	0·16	0·05	0·13	0·00	0·04
MgO	33·17	15·83	50·32	20·30	17·65
CaO	0·90	19·79	0·08		10·92
Na_2O	0·12	1·44			2·67
K_2O					1·71
NiO	0·10	0·04	0·46	0·44	0·11
Total	101·25	100·15	100·72	98·40	97·48
Mg#	0·911	0·906	0·908	0·759	0·892

21-6 (Halvdan)

	Cpx av. of 3	Amph av. of 7
SiO_2	53·31	43·43
TiO_2	0·13	0·73
Al_2O_3	3·97	14·14
Cr_2O_3	0·74	1·43
FeO	2·10	3·19
MnO	0·06	0·05
MgO	16·06	17·95
CaO	21·70	11·04
Na_2O	1·06	3·32
K_2O		0·60
NiO		
Total	99·12	95·86
Mg#	0·932	0·909

Table 3: continued

Upper panel

	21-5 (Halvdan) Cpx c. av. of 4	21-5 Spl av. of 4	21-5 Amph av. of 4	Halvdan Amph in lava	4-90-1 (Sigurd) Cpx c. av. of 3	4-90-1 Ol av. of 2	4-90-1 Amph av. of 4	4-90-1 Phl av. of 3	25 (Sverre) Opx	25 Cpx	25 Ol	25 Spl	26a (Sverre) Opx c. av. of 2	26a Opx r. av. of 3	26a Cpx c. av. of 3	26a Cpx r. av. of 4	26a Ol av. of 2	26a Spl av. of 2	28b (Sverre) Opx	28b Cpx
SiO_2	53·09	0·02	43·37	40·57	50·85	40·48	41·47	36·55	55·14	51·91	40·91		55·62	56·43	52·41	53·44	40·77	0·01	53·84	51·59
TiO_2	0·13	0·08	0·84	4·33	0·72		3·13	4·85	0·11	0·49		0·15		0·03	0·02	0·02		0·05	0·09	0·33
Al_2O_3	4·06	47·02	14·78	14·40	5·64		13·99	16·63	3·43	5·89		57·07	2·29	1·49	2·16	1·20		32·66	3·80	5·47
Cr_2O_3	0·77	22·35	1·71	0·08	1·40		1·38	1·17	0·28	0·60		11·33	0·62	0·21	0·85	0·39	0·05	34·74	0·32	0·87
FeO	2·20	11·52	3·46	11·93	3·59	10·43	4·56	4·83	6·29	2·15	9·88	10·68	5·62	5·64	1·65	1·65	8·58	15·25	6·07	2·12
MnO	0·08		0·00	0·12		0·28				n.d.			0·13	0·10	0·04	0·07	0·08		0·19	0·12
MgO	16·13	19·20	18·07	11·74	15·26	47·33	16·22	20·01	33·67	15·19	49·58	21·40	34·20	35·09	16·83	17·43	49·87	15·33	33·86	15·31
CaO	21·80		11·50	9·79	20·94		11·26	0·00	0·56	20·80			0·80	0·28	24·17	24·48			0·61	21·96
Na_2O	1·09		3·35	3·22	1·38		2·62	0·83		0·98			0·02		0·41	0·27				1·38
K_2O			0·60	0·90			1·82	9·13												
NiO	n.d.	n.d.	0·06	0·06		0·54	0·00	0·00	n.d.	n.d.	n.d.	n.d.	n.d.	n.d.	n.d.	n.d.	n.d.	n.d.	n.d.	n.d.
Total	99·35	100·19	97·68	97·14	99·78	98·77	96·43	93·99	99·48	98·01	100·37	100·63	99·27	99·28	98·56	98·92	99·33	98·03	98·78	99·15
Mg#	0·929	0·748	0·903	0·637	0·883	0·890	0·864	0·881	0·905	0·926	0·899	0·781	0·916	0·917	0·948	0·950	0·912	0·642	0·909	0·928

Lower panel

	28b (Sverre) Ol	28b Spl	39-86-1 (Sverre) Opx c. av. of 2	39-86-1 Cpx c. av. of 3	39-86-1 Ol av. of 2	39-86-1 Spl av. of 2	39-86-2 (Sverre) Opx c. av. of 3	39-86-2 Cpx c. av. of 4	39-86-2 Ol av. of 3	39-86-2 Spl av. of 2	63-90-18 (Sverre) Opx c. av. of 4	63-90-18 Opx r. av. of 3	63-90-18 Cpx c. av. of 2	63-90-18 Cpx r. av. of 2	63-90-18 Ol av. of 2	63-90-18 Spl	63-90-30 (Sverre) Opx c. av. of 2	63-90-30 Cpx c. av. of 3	63-90-30 Ol av. of 3	63-90-30 Spl
SiO_2	40·48		55·44	51·85	40·95	0·05	56·07	52·58	40·88	0·10	54·70	55·23	51·09	52·05	40·26	0·04	57·02	52·39	40·82	0·02
TiO_2		0·05	0·05	0·24		0·08	0·08	0·37		0·07	0·10	0·07	0·45	0·29		0·06	0·15	0·49		0·08
Al_2O_3		56·64	3·45	5·19		55·76	3·71	5·23		55·25	3·83	3·38	5·39	4·73		53·77	2·18	4·82		43·31
Cr_2O_3		12·96	0·33	0·79		12·98	0·34	0·86		11·78	0·36	0·24	0·79	0·71		12·57	0·34	1·29		25·04
FeO	9·38	10·78	5·71	2·30	9·19	10·21	6·06	2·37	9·36	10·25	6·23	6·02	2·45	2·42	9·63	10·82	5·43	2·11	8·77	12·25
MnO	0·16	0·12	0·13	0·11	0·14	0·10	0·16	0·10	0·10	0·00	0·15	0·12	0·09	0·10	0·12	0·00	0·10	0·07	0·12	0·12
MgO	50·30	20·40	34·38	15·85	49·60	20·34	34·12	15·68	49·91	20·69	33·28	33·59	15·15	15·63	49·04	19·88	34·89	15·57	50·65	18·39
CaO			0·46	21·50	0·04	0·01	0·60	21·24	0·06		0·51	0·54	21·55	21·83	0·05		0·66	21·43	0·04	
Na_2O			0·07	1·37		0·00	0·07	1·22			0·05	0·05	1·23	1·15			0·04	1·34		
K_2O																				
NiO	n.d.	n.d.	0·09	0·04	0·35	0·27	0·11		0·37	0·40	n.d.	n.d.	n.d.	n.d.	n.d.	n.d.	0·07	0·02	0·42	0·27
Total	100·32	100·95	100·11	99·23	100·26	99·80	101·32	99·64	100·67	98·54	99·22	99·24	98·19	98·92	99·08	97·15	100·87	99·52	100·80	99·37
Mg#	0·905	0·771	0·915	0·925	0·906	0·780	0·909	0·922	0·905	0·783	0·905	0·909	0·917	0·920	0·901	0·766	0·920	0·929	0·911	0·728

Blank entries, below detection limits; n.d., not determined; r, rim; c, core. Mg#, atomic Mg/(Mg + Fe); Cr#, atomic Cr/(Cr + Al).
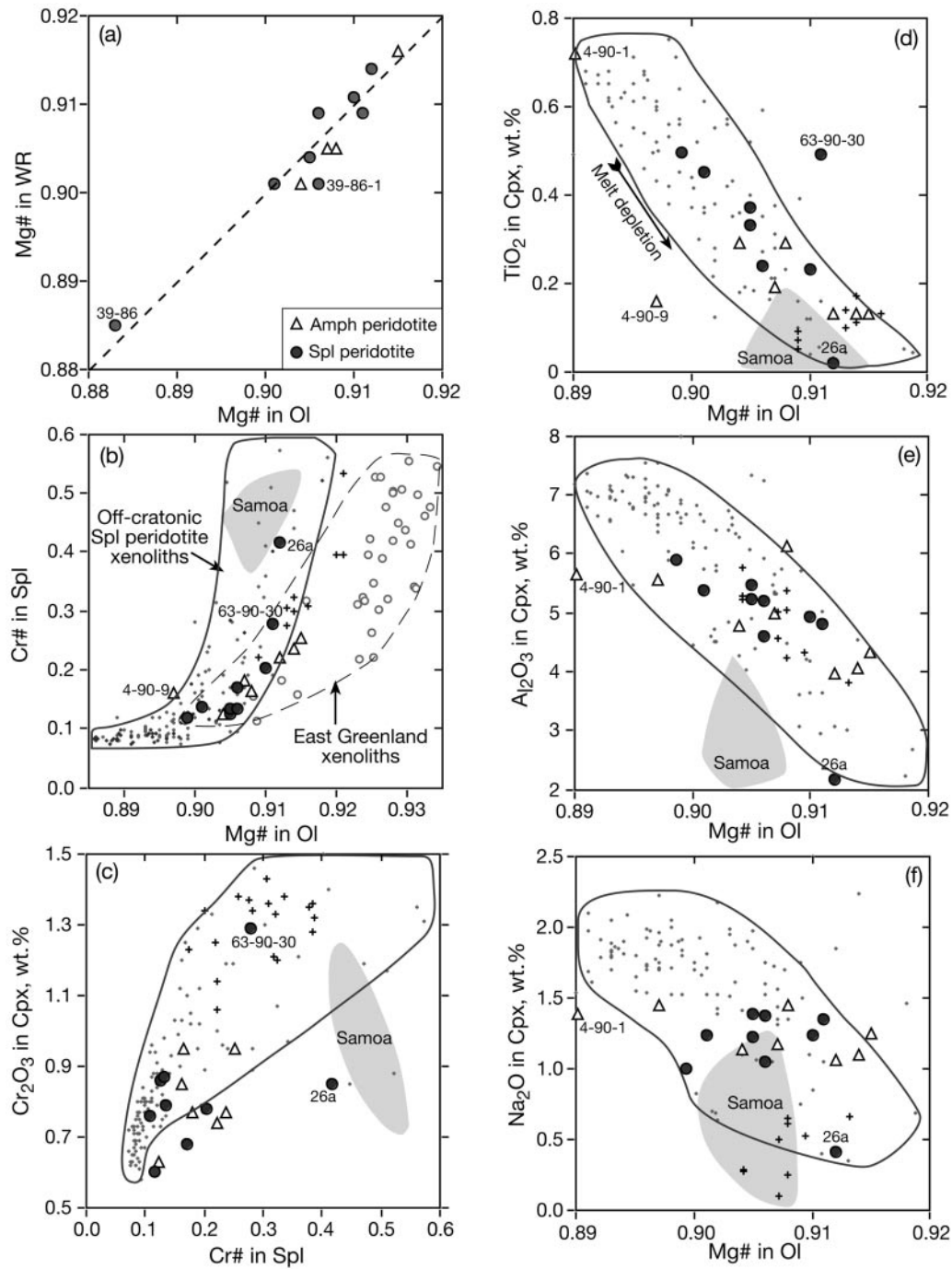
Fig. 4. Major element concentrations and ratios for minerals from Spitsbergen xenoliths (grain core compositions; symbols as in Fig. 3). Data for Fe-rich sample 39-86 are from Ionov *et al.* (1996). Also shown are xenoliths in basalts from Siberia and Mongolia (see Fig. 3 for data sources), Samoa (shaded field; Hauri & Hart, 1994) and East Greenland (open grey circles contoured by dashed line; Bernstein *et al.*, 1998) and abyssal peridotites (grey crosses; Hellebrand *et al.*, 2001).

equilibration temperatures estimated for that sample (740–800°C). The low *T* values indicate a relatively shallow depth of origin, compared with the other xenoliths, possibly near the crust–mantle boundary. The cores

of the largest orthopyroxene grains from sample 26a have exsolution lamellae and very high Ca abundances, indicating incomplete equilibration after cooling from *T* >1000°C.
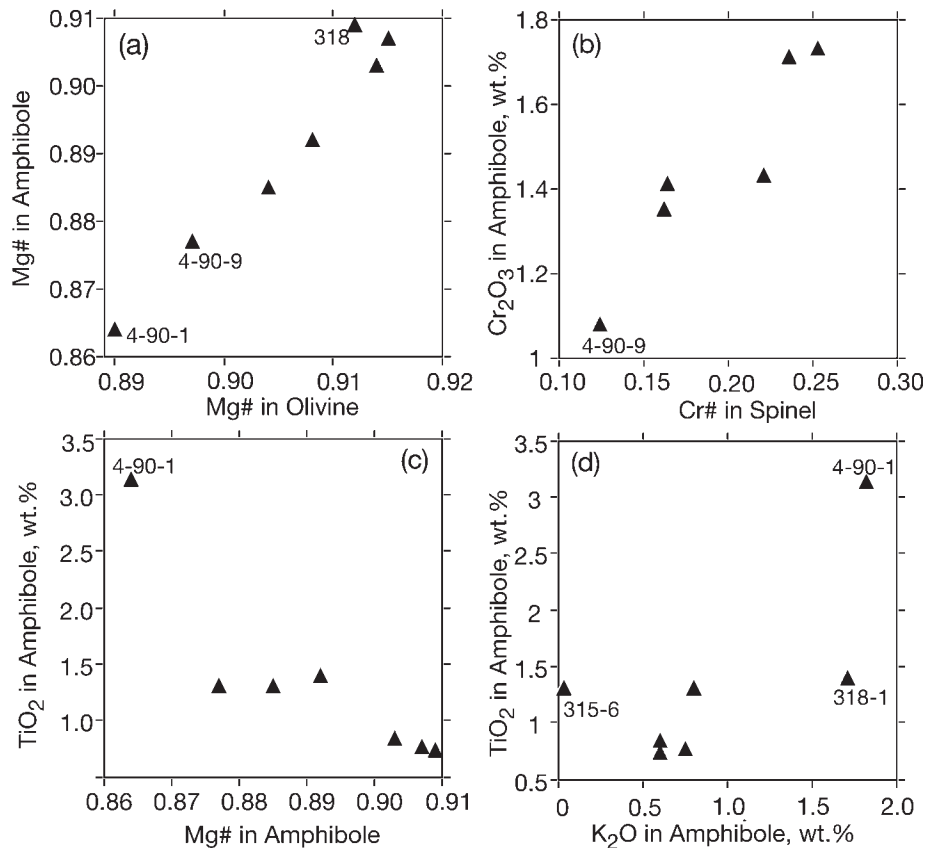
Fig. 5. Plots of amphibole compositions: $Mg\#_{Amph}$ vs $Mg\#_{Ol}$ (a), Cr_2O_3 in amphibole vs $Cr\#_{Spl}$ (b), and TiO_2 in amphibole vs $Mg\#$ (c) and K_2O (d). The regular trends for the major element contents in (a) and (b) indicate chemical equilibration of the amphibole with other minerals. Poor correlation in (c) and (d) suggests that the concentrations of K and Ti are controlled by metasomatic processes.

TRACE ELEMENT COMPOSITIONS OF MINERALS

Average trace element abundances for the cores of clinopyroxene, amphibole and mica grains determined by LAM-ICP-MS are given in Table 4. Differences between individual analyses of the same mineral were normally within analytical precision, except for highly variable Zr (28–97 ppm), Nb (0·4–1·1 ppm), Hf (1–2·5 ppm) and Ta (<0·02–0·18 ppm) in clinopyroxene 39-86-1, and Rb (5·6–10·5 ppm) and Ba (760–1350 ppm) in amphibole 318-1. Sample 39-86-1 is obviously heterogeneous and is not considered below. We also use LAM-ICP-MS analyses of minerals in four xenoliths from Ionov (1998). Several analyses of apatite were published earlier (Ionov *et al.*, 1996).

The abundances of moderately incompatible elements, such as the heavy rare earth elements (HREE) and Y, are lower in the Spitsbergen clinopyroxenes than for fertile lherzolites worldwide and decrease systematically with increasing $Mg\#_{Ol}$ (Fig. 6a). In contrast, the abundances of highly incompatible elements [Sr, light REE (LREE), Nb, Th, U] do not define coherent trends with $Mg\#$ variations (Fig. 6b and c) and for nearly all the samples are much higher than those expected for residues after partial melting (e.g. Johnson *et al.*, 1990). Similar observations were made earlier for many other suites of mantle peridotites and attributed to metasomatic enrichment in incompatible elements of residual rocks formed by earlier partial melting events (e.g. Frey & Green, 1974; Kempton, 1987; McDonough & Frey, 1989). Minerals from composite xenolith 4-90-1 and harzburgite 26a commonly plot off trends defined by the other xenoliths.

Two major types of clinopyroxene can be identified in the Spitsbergen xenoliths on the basis of their incompatible element abundances and ratios (Fig. 6b–f). Type-1 clinopyroxene is characterized by lower concentrations of the middle REE (MREE) and Sr (and therefore lower MREE/HREE ratios, e.g. Nd/Yb)
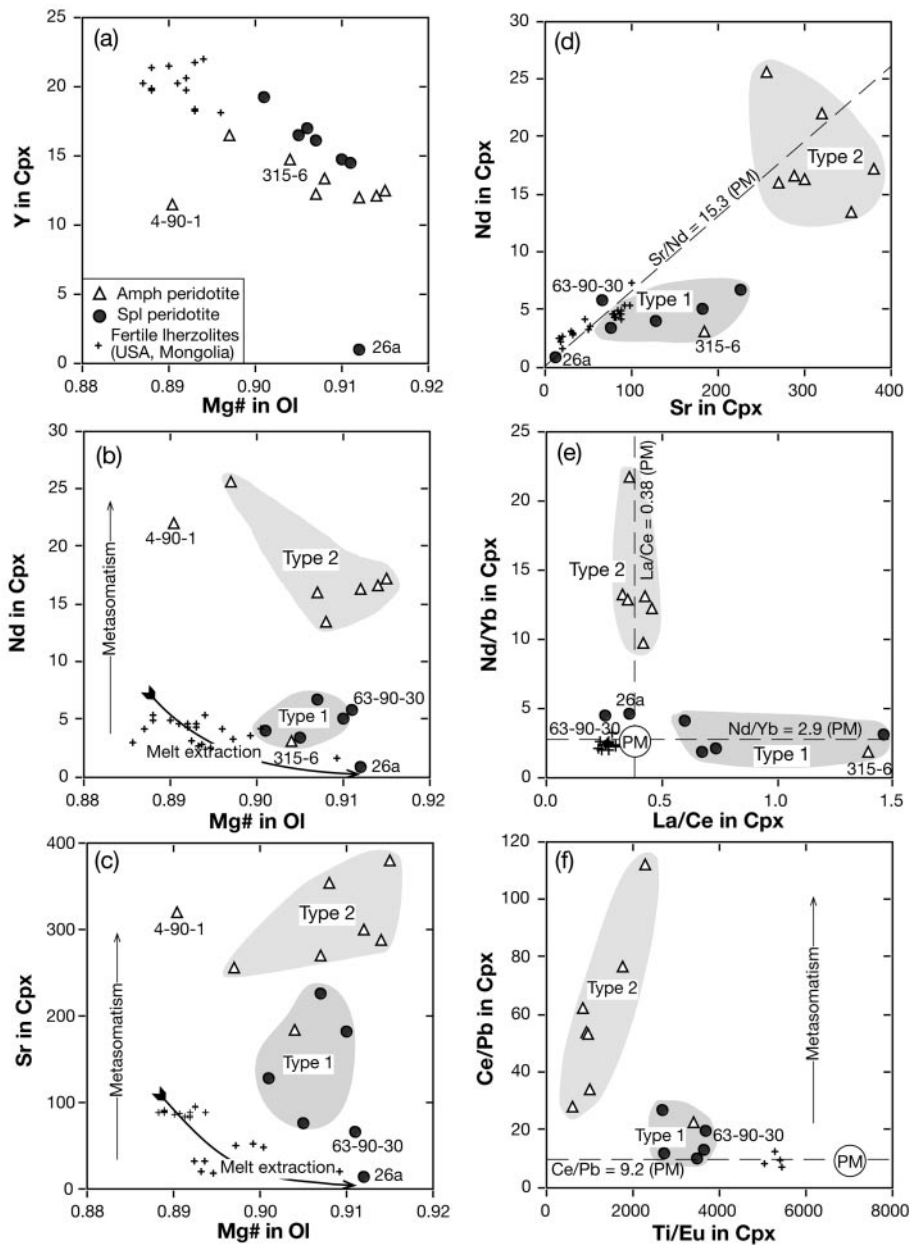
Table 4: Average LAM-ICP-MS trace element concentrations of minerals

Type:	2	1	2	1	2	2	1	1	1	1	2	vein	vein	vein	2	1	2	2
Sample:	21-5	26a	311-9	315-6	318	318-1	39-86-1	39-86-2	4-25-90	63-90-18	63-90-30	4-90-1	4-90-1	4-90-1	21-5	315-6	318	318-1
Mineral:	Cpx	Cpx	Cpx*	Cpx	Cpx	Cpx	Cpx*	Cpx	Cpx	Cpx*	Cpx	Cpx	Phl*	Amph*	Amph	Amph*	Amph*	Amph*
No. of analyses:	1	2	4	3	2	2	5	3	2	3	3	2	2	3	1	5	4	4
Sc	75	57	70	71	87	58	78	79	69	70	80	52	6.6	41	53	49	57	44
Ti	881	174	986	1833	725	1559	1367	2092	1910	2489	3450	4179	25428	18655	4436	7346	4380	8134
V	n.d.	171	238	252	231	242	266	271	252	285	297	244	299	356	n.d.	350	328	347
Rb													533	23.5	9.2	5.8	7.2	*8.1*
Sr	287	12.4	270	183	380	353	193	74.7	182	127	65.2	320	404	967	622	466	820	981
Y	12.1	0.92	12.2	14.7	12.4	13.3	17.0	16.4	14.7	19.2	14.4	11.5	*0.12*	14.5	16.1	23.5	18.4	16.4
Zr	21.3	2.03	16.6	20.1	31.0	16.3	59	25.9	29.0	29.3	47.1	160	27.5	195	21.2	20.6	35.8	19.4
Nb	<0.24	0.100	0.93	<0.014	0.23	0.77	*0.67*	0.024	0.08		<0.02	2.30	110.8	167	4.31	*0.92*	28.2	68.9
Cs													13.3	0.05		0.13	0.18	0.19
Ba	<0.3	0.04	0.17	0.13	0.21	0.29	0.11	0.041	0.34		0.04	0.22	8935	669	445	1366	842	950
La	8.7	0.47	9.2	16.1	12.7	12.1	11.8	3.03	21.0	5.24	1.30	12.6		17.9	13.9	20.8	17.7	15.9
Ce	27.2	1.32	26.7	11.6	29.8	28.9	19.6	4.49	14.4	7.15	5.08	35.5		47.8	42.1	15.6	43.2	38.2
Pr	3.95	0.15	3.63	0.71	3.78	3.33	2.13	0.60	1.22	0.78	0.92	4.87	0.009	6.48	5.86	0.98	5.54	4.44
Nd	16.5	0.87	15.9	3.10	17.2	13.4	9.0	3.42	4.96	3.98	5.77	22.0	0.006	28.4	23.9	4.2	23.8	17.2
Sm	2.19	0.20	3.35	1.14	3.44	2.28	2.23	1.43	1.65	1.38	2.29	4.84	0.063	5.61	3.42	1.57	4.67	2.89
Eu	0.88	<0.03	1.16	0.54	1.23	0.88	0.80	0.60	0.70	0.68	0.93	1.83		2.11	1.41	0.76	1.74	1.09
Gd	3.11	0.19	2.88	1.85	2.66	2.13	2.42	2.05	2.12	2.61	2.92	4.01		5.16	2.80	2.63	3.93	2.67
Tb		<0.02	0.45	0.38	0.39	0.37	0.42	0.41	0.40	0.48	0.49	0.52		0.72		0.56	0.59	0.45
Dy	2.45	0.19	2.36	2.67	2.50	2.46	2.84	2.87	2.74	2.98	3.03	2.81		3.06	2.93	3.77	3.32	2.74
Ho	0.51	0.037	0.47	0.60	0.52	0.53	0.66	0.65	0.56	0.68	0.60	0.48		0.55	0.59	0.87	0.68	0.62
Er	1.60	0.14	1.28	1.72	1.34	1.43	1.83	1.95	1.68	2.00	1.49	1.07		1.33	1.67	2.41	1.92	1.64
Tm	n.d.	n.d.	0.19	n.d.	n.d.	n.d.	0.29	0.27	n.d.	0.30	n.d.	n.d.		0.18	n.d.	0.40	0.29	0.23
Yb	<1.3	0.19	1.24	1.74	1.32	1.39	1.83	1.90	1.65	1.90	1.31	1.02		1.02	1.88	2.47	1.77	1.59
Lu	0.24	0.029	0.17	0.23	0.18	0.17	0.29	0.28	0.23	0.31	0.18	0.15		0.15	0.21	0.34	0.27	0.22
Hf	<0.66	<0.05	0.48	0.69	0.85	0.59	*1.27*	0.85	0.93	1.02	1.35	6.81	0.77	7.81	0.71	0.70	0.96	0.65
Ta			0.03				*0.12*	0.017			0.008	0.44	6.48	10.37		0.079	0.46	0.28
Pb	0.81	0.30	0.43	0.51	1.06	0.38	1.62	0.45	1.23	0.56	0.26	0.32	1.24	1.27	2.27	1.97	3.11	1.07
Th	0.90	<0.012	0.81	2.01	1.03	0.59	2.73	0.271	4.62	0.51	0.094	0.47	0.0043	0.59	1.26	2.38	1.40	0.63
U	<0.23	0.035	0.14	0.66	0.35	0.108	0.92	0.097	1.59	0.19	0.033	0.071	0.013	0.069	0.16	0.70	0.44	0.11
Sr/Nd	17.4	14.2	17.0	59.0	22.1	26.3	21.5	21.9	36.6	32.0	11.3	14.5		34.0	26	110.4	34.5	57.2
Ti/Zr	41	86	59	91	23	96	23	81	66	85	73	26	926	96	210	357	122	420
Zr/Hf			34	29	36	28	46	30	31	29	35	24	36	25	30	29	37	30
Nb/Ta			30.7				5.6	1.4				5.2	17.1	16.1		11.6	61.8	245.5
Zr/Sm	10	10	5	18	9	7	26	18	18	21	21	33		35	6	13	8	7
U/Pb		0.12	0.33	1.29	0.33	0.28	0.57	0.22	1.29	0.34	0.13	0.22		0.05	0.07	0.36	0.14	0.10
Th/U			5.8	3.1	2.9	5.5	3.0	2.8	2.9	2.7	2.8	6.6		8.5	7.7	3.4	3.2	5.7

*Analyses at CNR-CSCC, Pavia.
Blank entries, below detection limit; n.d., not determined. Values in italics indicate averages with significant differences (well above analytical precision) between individual analyses.

Fig. 6. Variation plots for abundances of Y, Nd and Sr in clinopyroxene vs Mg#$_{OI}$ and for abundances and ratios of trace elements in clinopyroxene (symbols as in Fig. 4). Crosses are compositions of clinopyroxene from unmetasomatized fertile lherzolites from the southwestern USA and Mongolia (Stosch & Lugmair, 1986; Galer & O'Nions, 1989) and unpublished data of D. A. Ionov (1998). PM, primitive mantle (Hofmann, 1988). Melt extraction trends are after Johnson *et al.* (1990). Plots (b)–(f) outline two major types of Spitsbergen clinopyroxenes based on abundances and/or elemental ratios of REE, Sr, Ti and Pb.

relative to Type-2 clinopyroxene, and by high La/Ce ratios (Fig. 6e). We emphasize that the terms Type-1 and Type-2 are used here simply to distinguish between the two most common trace element patterns in this xenolith suite. They are not related to the classification of Frey & Green (1974), which would identify all those samples as Type I (based on their high Mg#), or with types 1a (LREE depleted) and 1b (LREE enriched) of Kempton (1987).

The differences between the two types are further highlighted on primitive mantle (PM)-normalized trace element distribution diagrams (Fig. 7). Type-1 clinopyroxenes have nearly flat HREE–MREE patterns (at ~4 times the PM level) followed by moderate depletion
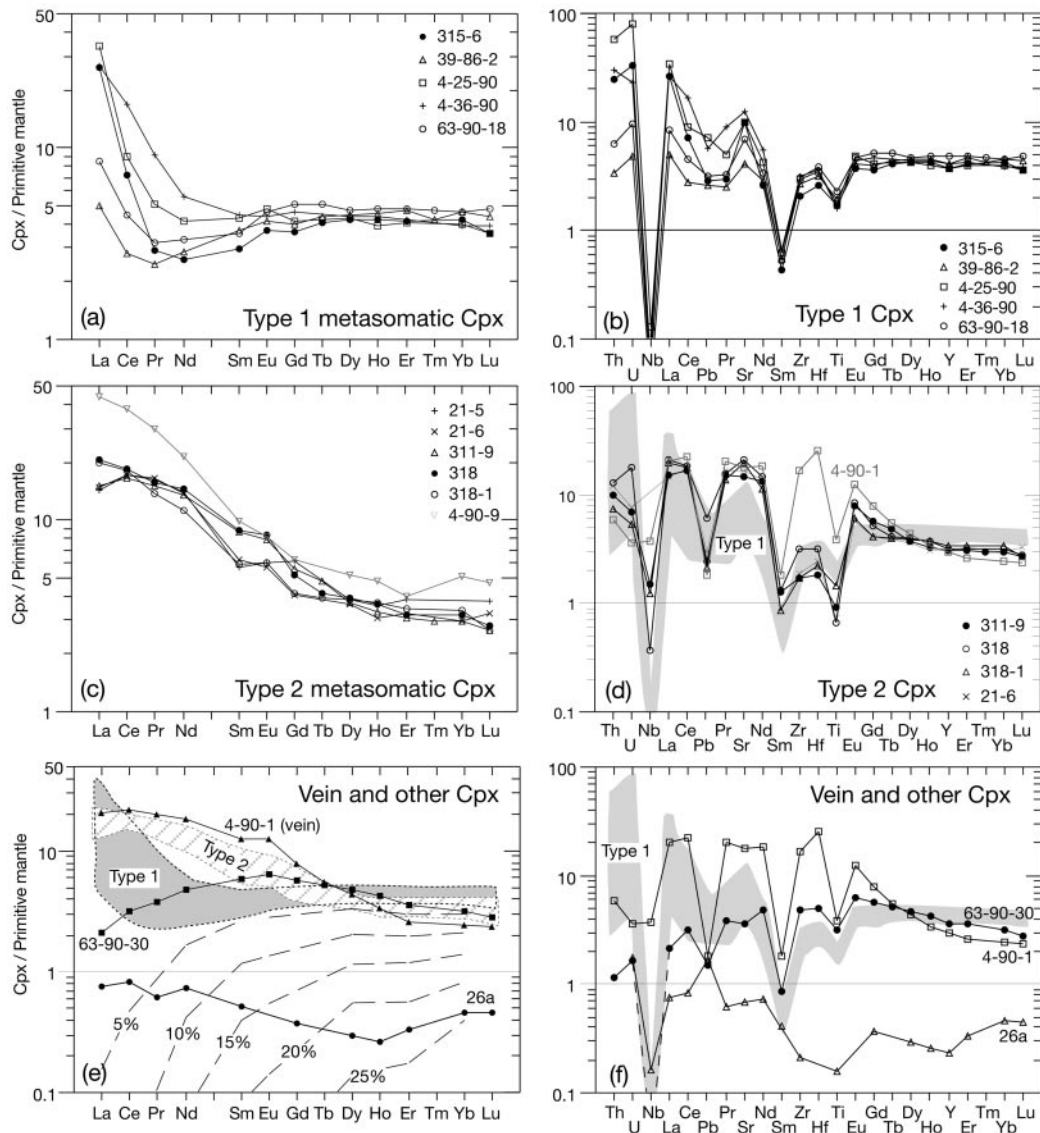
Fig. 7. Primitive mantle-normalized (Hofmann, 1988) REE and multi-element abundance patterns of clinopyroxene: (a) and (b) Type-1; (c) and (d) Type 2; (e) and (f) vein and other samples together with fields for Types 1 and 2. Cpx 4-90-9 (after Ionov, 1998) has higher HREE and LREE contents than any other Type-2 sample. Dashed lines are clinopyroxene compositions in residues of 5–25% of partial melting of primitive mantle, calculated using algorithm and partition coefficients from Takazawa *et al.* (2000). It should be noted that the residual clinopyroxene compositions were calculated for amphibole-free rocks. Comparisons between these model compositions and clinopyroxenes from amphibole-bearing xenoliths should take into account REE partitioning from clinopyroxene into the metasomatic amphibole (Fig. 8c).

from Eu to Nd (Pr) and a steep La–Ce–(Pr) inflection (Fig. 7a). Type-2 clinopyroxenes have somewhat lower HREE concentrations ($\sim 3 \times$ PM) followed by a continuous increase in normalized REE concentrations from Ho to Ce (Fig. 7c). Both types of clinopyroxene have strong negative Nb anomalies and small to moderate positive Sr anomalies (Fig. 7b and d). Type-2 clinopyroxenes have similar or only slightly lower concentrations of Ti, Zr and Hf compared with Type-1 clinopyroxenes, but their high MREE levels result in

pronounced negative anomalies of those elements (Fig. 7d) and low Ti/Eu ratios. Both clinopyroxene types also have a similar range of Pb concentrations, but high Nd and Ce in the Type-2 bring about conspicuous negative Pb anomalies (Fig. 7d). A Ce/Pb vs Ti/Eu diagram clearly distinguishes between the two types (Fig. 6f).

Clinopyroxenes 26a and 63-90-30 cannot be grouped with either Type-1 or Type-2: 26a has very low abundances of all lithophile trace elements and a nearly flat REE pattern; 63-90-30 has a convex-upwards REE
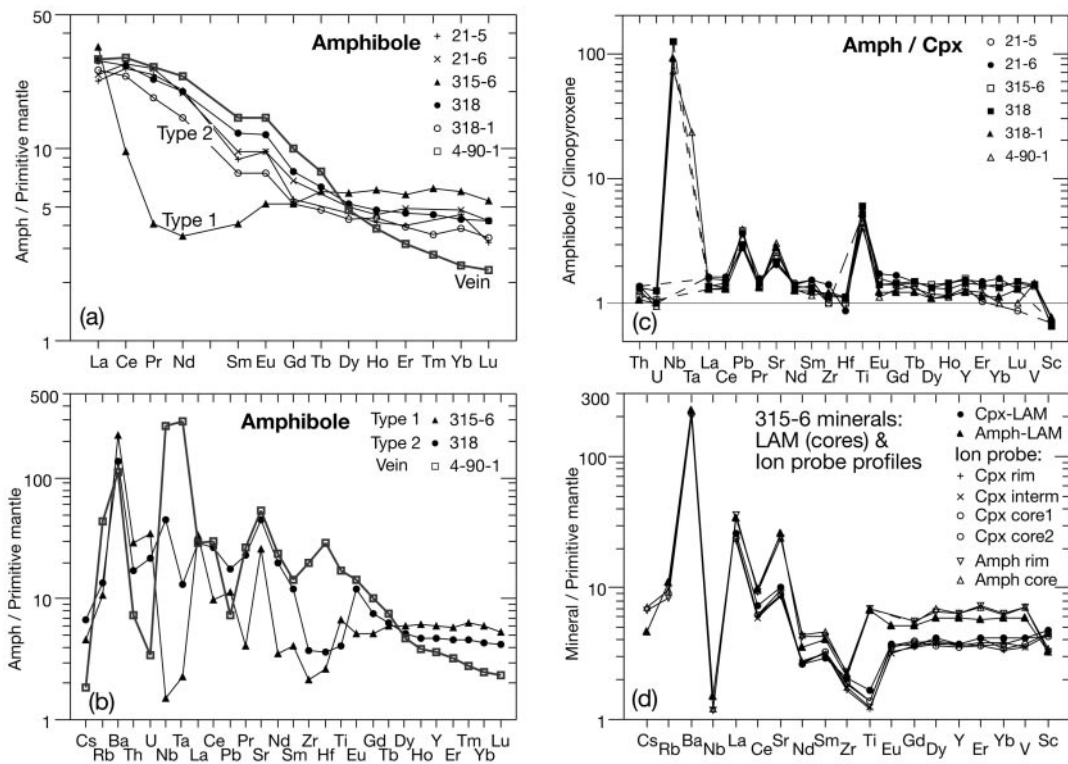
Fig. 8. Primitive mantle-normalized (Hofmann, 1988) REE (a) and multi-element (b) abundance patterns of amphiboles. Three samples representing the range of compositional variations are presented in (b). It should be noted that the only Type-1 amphibole has a pattern distinct from those in the rest of the samples (Type-2 and vein). (c) Amphibole/clinopyroxene trace element ratios. (d) Primitive mantle-normalized element abundances determined in the cores of clinopyroxene and amphibole by LAM-ICP-MS, and core–rim profiles by ion probe in sample 315-6. The lack of significant core–rim zoning and consistency of the LAM-ICP-MS and the ion probe data should be noted.

pattern (Fig. 7e and f). Vein clinopyroxene 4-90-1 has an REE pattern resembling those of Type-2 clinopyroxenes but differs from them largely by its much higher HFSE (high field strength element) abundances and lower HREE (Fig. 7d–f).

Only one Type-1 sample contains amphibole (315-6), whereas all Type-2 xenoliths are amphibole bearing. However, it is the elemental abundances and ratios rather than presence of 'hydrous' phases that define and characterize the two geochemical xenolith types. The REE pattern of Type-1 amphibole 315-6 is clearly distinct from that of Type-2 amphiboles (Fig. 8a); it also has unusually low abundances of K (Fig. 5d), Nb and Ta (Fig. 8b). REE patterns in amphiboles are very similar to those of coexisting clinopyroxenes; these two minerals also have very similar abundances of Th, U, Zr and Hf (Figs 8d and 9b). However, the amphiboles have much higher concentrations of the alkalis, Ba, Nb, Ta and Ti, and moderately higher concentrations of Pb and Sr (Fig. 8c), consistent with amph–cpx relationships observed in other mantle rocks (e.g. Ionov & Hofmann, 1995;

Kempton *et al.*, 1999; Tiepolo *et al.*, 2001). Vein amphibole has high Nb and Ta abundances, no negative anomalies for Ti and Zr, and a negative Pb anomaly (Fig. 8b). All the amphiboles are relatively low in Rb and Cs, with Rb/Ba and Rb/Sr ratios below those of the primitive mantle.

Ion probe analyses in profiles across mineral grains found slightly lower Ti and V in rims compared with cores of clinopyroxene (but not in the single amphibole grain analysed). Other elements show no significant differences in abundances between the cores and the rims (Table 5, Fig. 8d). The ion probe and LAM-ICP-MS data for the same samples agree well (Fig. 8d).

TRACE ELEMENT COMPOSITIONS OF BULK ROCKS

Trace element abundances in whole-rock samples are given in Table 6. Ionov *et al.* (1993*b*) and Ionov (1998) found high incompatible trace element concentrations in

Table 5: Ion microprobe trace element concentrations in ppm for minerals in thin sections (core–rim pairs)

| Sample: | 315-6 | | | | | | Amph | | | 63-90-18 | | | 39-86-2 | | | 4-36-90[*] | | | | |
| Grain: | Cpx (rim-to-core profile) | | | | | | | | | Cpx | | | Cpx | | | Cpx (rim-to-core profile) | | | | |
Position:	rim	int1	int2	core	core	av. of 5	rim	core	av. of 2	rim	core	av. of 2	rim	core	av. of 2	A	B	C	D	av. of 4
K							180	182	181							n.d.	n.d.	n.d.	n.d.	
Sc	65	66	69	68	64	66	49	51	50	66	66	66	70	76	73	n.d.	n.d.	n.d.	n.d.	
Ti	1305	1344	1528	1506	1498	1436	7576	7510	7543	1723	2361	2042	1760	2235	1997	n.d.	n.d.	n.d.	n.d.	
V	210	215	231	227	249	226	430	422	426	270	276	273	271	290	281	n.d.	n.d.	n.d.	n.d.	
Cr	3597	3800	4436	3940	3904	3935	7301	7314	7308	4909	4901	4905	4565	5141	4853	n.d.	n.d.	n.d.	n.d.	
Rb						4·5	5·1	4·8												
Sr	158	159	158	160	173	162	440	441	441	118	111	114	72	71	71	191	175	176	184	181
Y	14·6	14·3	14·7	14·7	13·8	14·4	25·1	25·2	25·1	15·2	16·3	15·7	16·4	17·6	17·0	14·2	14·7	14·9	14·6	14·6
Zr	16·4	17·3	18·1	18·7	17·9	17·7	22·1	21·9	22·0	25·5	26·1	25·8	22·9	24·4	23·6	33·8	28·0	30·0	35·6	31·8
Nb							0·73	0·75	0·74	0·03	0·03	0·033	0·04	0·07	0·054					
Cs							0·18	0·19	0·19							n.d.		n.d.	n.d.	
Ba							1215	1312	1264	0·03	0·06	0·05	0·04	0·09	0·07					
La	14·1	14·2	13·9	14·5	14·5	14·2	21·7	21·1	21·4	5·1	4·8	5·0	2·63	2·68	2·7	20·6	19·9	20·9	22·2	20·9
Ce	9·8	9·5	9·9	10·1	10·0	9·86	14·8	15·3	15·0	7·2	6·6	6·9	4·0	4·1	4·0	31·7	30·4	32·3	34·5	32·2
Nd	3·3	3·2	3·2	3·1	3·1	3·20	5·1	5·2	5·16	3·6	3·2	3·41	3·2	3·6	3·36	6·75	6·21	6·32	7·22	6·62
Sm	1·22	1·24	0·98	1·26	1·26	1·19	1·64	1·77	1·71	1·27	1·40	1·34	1·18	1·25	1·21	1·43	1·42	1·42	1·53	1·45
Eu	0·48	0·47	0·46	0·52	0·53	0·49				0·52	0·55	0·54	0·53	0·56	0·54	0·58	0·59	0·66	0·62	0·62
Gd	1·83	1·85	2·52	1·98	2·00	2·04	2·90	2·83	2·86	2·06	2·31	2·19	2·17	2·26	2·21	2·31	2·23	2·31	2·40	2·31
Dy	2·41	2·44	2·59	2·52	2·32	2·46	4·22	4·43	4·32	2·74	3·04	2·89	2·87	3·13	3·00	2·37	2·54	2·74	2·72	2·59
Er	1·53	1·61	1·68	1·73	1·51	1·61	3·02	2·98	3·00	1·55	1·76	1·66	1·87	1·90	1·89	1·64	1·72	1·72	1·80	1·72
Yb	1·40	1·60	1·39	1·42	1·56	1·47	2·67	2·57	2·62	1·51	1·60	1·56	1·65	1·72	1·69	1·38	1·44	1·42	1·50	1·43

Si was used as internal standard. n.d., not determined.
*Analysed at Montpellier.

Table 6: Trace element analyses of whole rocks by solution ICP-MS (ppm)

	BIR-1		JP-1		Leaching products		WR peridotites														Basalts†			
	R.V.	av. of 2	R.V.	av. of 2	25 leach*	25 resid*	25*	26a	28b	311-9	315-6	318	318-1	318-1*	39-86-1	39-86-2*	4-25-90	4-36-90	63-90-18	63-90-30	H1-25	H3-15	S35a	39-86-2
Sc	44	48·76	7·2	8·0	2·56	11·35	12·60	9·4	12·3	12·6	13·9	8·8	16·0	14·6	13·2	n.d.	2·1	10·3	14·3	13·1	14·6	15·1	16·1	14·3
V	313	365·2	27·6	18·1	n.d.	n.d.	n.d.	32	50	51	63	34	69	66	53	n.d.	49	39	63	49	n.d.	n.d.	n.d.	n.d.
Co	51	56·53	116	118	n.d.	n.d.	n.d.	121	119	120	111	118	112	105	118	n.d.	117	118	110	121	n.d.	n.d.	n.d.	n.d.
Rb	0·24	0·21	0·34	0·33	0·453	0·223	0·787	0·30	0·18	0·26	0·42	0·78	0·07	0·072	0·65	0·25	0·63	0·67	0·40	0·57	49·3	51·9	49·8	50·4
Sr	110	109·7	0·57	0·64	8·49	8·03	18·26	1·25	11·0	35·4	29·8	51·1	44·2	45·0	26·1	13·2	67·8	57·9	18·6	7·7	1118	1174	1076	1060
Y	16·5	17·35	0·10	0·107	n.d.	n.d.	n.d.	0·06	1·62	1·65	2·43	1·26	2·51	2·54	2·30	2·11	1·91	1·58	2·47	1·74	27·2	27·5	26·7	25·5
Zr	14·5	15·90	5·34	5·49	0·072	2·41	2·90	0·20	2·52	2·17	3·33	2·56	2·87	2·91	6·08	3·67	4·61	3·33	3·45	5·32	231	238	241	243
Nb	0·55	0·59	0·036	0·040	0·004	0·072	0·107	0·084	0·036	2·45	0·13	1·26	0·96	1·02	1·62	0·073	0·48	0·21	0·084	0·111	77·1	77·8	80·1	79·6
Cs	0·005	0·006	0·035	0·040	n.d.	n.d.	n.d.	0·10	0·017	0·026	0·040	0·11	0·007	0·006	10·20	0·022	0·099	0·067	0·16	0·13	1·05	1·15	0·91	0·93
Ba	6·4	6·8	9·8	9·9	1·32	1·05	3·89	0·83	11·0	14·9	22·7	31·7	13·6	13·4	11·1	6·0	16·7	20·9	4·4	3·0	930	988	962	960
La	0·58	0·63	0·030	0·028	0·016	0·151	0·207	0·042	0·60	1·06	1·99	1·31	1·54	1·52	1·32	0·36	2·03	1·30	0·45	0·155	71·0	74·8	67·6	67·1
Ce	1·85	1·95	0·054	0·066	0·031	0·284	0·411	0·065	0·74	2·76	1·43	2·65	3·74	3·68	2·10	0·56	1·71	2·14	0·66	0·49	116	121	111	110
Pr	0·37	0·39	0·0071	0·0083	0·0041	0·058	0·075	0·008	0·07	0·39	0·10	0·35	0·48	0·47	0·24	0·080	0·17	0·17	0·08	0·10	11·5	11·9	11·0	11·0
Nd	2·35	2·47	0·033	0·031	0·020	0·320	0·403	0·030	0·30	1·71	0·42	1·42	1·86	1·84	0·95	0·44	0·71	0·50	0·40	0·54	42·9	44·6	41·8	41·2
Sm	1·10	1·15	0·013	0·009	0·0066	0·134	0·162	0·006	0·12	0·36	0·15	0·27	0·35	0·33	0·23	0·17	0·19	0·13	0·16	0·22	8·28	8·62	8·12	8·13
Eu	0·52	0·53	0·0034	0·0025	0·0024	0·056	0·066	0·002	0·048	0·124	0·065	0·095	0·122	0·121	0·081	0·074	0·071	0·050	0·069	0·081	2·81	2·91	2·74	2·74
Gd	1·97	1·90	0·013	0·010	0·0098	0·217	0·237	0·007	0·17	0·33	0·25	0·24	0·35	0·34	0·29	0·27	0·24	0·18	0·26	0·29	7·34	7·46	7·27	7·29
Tb	0·38	0·38	0·0026	0·0022	0·0017	0·043	0·047	0·001	0·034	0·049	0·050	0·036	0·058	0·058	0·052	0·056	0·044	0·034	0·052	0·049	0·88	0·90	0·86	0·82
Dy	2·50	2·62	0·018	0·014	0·0124	0·311	0·338	0·008	0·24	0·27	0·35	0·20	0·38	0·37	0·34	0·39	0·29	0·24	0·36	0·29	5·36	5·43	5·17	4·96
Ho	0·57	0·61	0·0043	0·0035	0·0028	0·069	0·077	0·002	0·055	0·056	0·084	0·042	0·086	0·085	0·078	0·098	0·065	0·055	0·084	0·060	0·95	0·97	0·93	0·88
Er	1·70	1·80	0·014	0·013	0·0085	0·209	0·229	0·008	0·17	0·16	0·26	0·12	0·26	0·25	0·23	0·29	0·20	0·17	0·26	0·17	2·23	2·22	2·12	2·10
Tm	n.d.	n.d.	n.d.	n.d.	0·0014	0·032	0·036	n.d.	n.d.	n.d.	n.d.	n.d.	n.d.	n.d.	n.d.	0·044	n.d.	n.d.	n.d.	n.d.	n.d.	n.d.	n.d.	n.d.
Yb	1·60	1·71	0·021	0·020	0·0090	0·209	0·235	0·019	0·18	0·16	0·27	0·12	0·26	0·25	0·24	0·29	0·20	0·17	0·26	0·15	1·69	1·71	1·53	1·43
Lu	0·25	0·26	0·0047	0·0044	0·0016	0·037	0·039	0·004	0·029	0·026	0·042	0·020	0·040	0·041	0·038	0·049	0·031	0·028	0·042	0·022	0·22	0·23	0·20	0·19
Hf	0·56	0·59	0·12	0·113	0·0017	0·084	0·089	0·005	0·077	0·048	0·094	0·060	0·088	0·088	0·116	0·118	0·110	0·080	0·106	0·134	4·87	5·02	4·97	5·01
Ta	0·06	0·04	0·0036	0·0040	0·0002	0·0030	0·0046	0·002	0·004	0·026	0·005	0·024	0·007	0·020	0·089	0·005	0·017	0·005	0·004	0·003	3·49	3·68	3·45	3·39
Pb	3·0	2·26	0·090	0·108	0·059	0·082	0·282	0·027	0·055	0·11	0·07	0·13	0·39	0·58	0·18	0·207	0·12	0·08	0·06	0·04	5·6	6·2	5·6	5·5
Th	0·030	0·033	0·012	0·013	0·0013	0·0086	0·018	0·005	0·097	0·099	0·273	0·127	0·081	0·082	0·347	0·044	0·46	0·196	0·049	0·012	9·53	10·06	8·64	8·39
U	0·010	0·013	0·012	0·012	0·0033	0·0031	0·009	0·012	0·029	0·028	0·095	0·045	0·021	0·021	0·106	0·016	0·29	0·153	0·016	0·009	2·1	2·2	2·0	2·0
Nb/Ta	n.d.	n.d.	n.d.	n.d.	29·1	23·9	23·0			93·0		53·2	128·1	50·0	18·3	15·4	27·3	40·7	18·8	32·3	22·1	21·1	23·2	23·5
Zr/Hf					42·2	28·6	32·6	40·8	32·8	44·8	35·3	42·6	32·5	33·0	52·6	31·1	42·0	41·6	32·6	39·8	47·4	47·5	48·5	48·6
Th/U					0·38	2·77	2·02	0·48	3·40	3·54	2·88	2·85	3·90	3·86	3·29	2·71	1·58	1·28	3·03	1·39	4·60	4·56	4·33	4·22
Nb/Th					3·6	8·5	6·1	15·3	0·4	24·7	0·5	9·9	11·9	12·5	4·7	1·7	1·0	1·1	1·7	9·1	8·1	7·7	9·3	9·5
Ba/La					83·0	7·0	18·8	20·1	18·4	14·1	11·4	24·3	8·8	8·8	8·4	16·7	8·2	16·0	9·7	19·3	13·1	13·2	14·2	14·3
Nb/La					0·28	0·48	0·52	2·02	0·06	2·31	0·06	0·97	0·62	0·67	1·23	0·21	0·23	0·16	0·19	0·71	1·09	1·04	1·19	1·19
Sr/Nd					424·5	25·1	45·4	41·8	36·4	20·7	71·6	35·9	23·7	24·5	27·4	29·7	96·1	115·2	46·4	14·4	26·1	26·3	25·7	25·7
$Zr_{PM}/(Sm + Eu)_{PM}$					0·43	0·66	0·66	1·30	0·81	0·24	0·79	0·38	0·33	0·34	0·79	0·79	0·95	0·99	0·77	0·96	1·14	1·13	1·21	1·22

*Analysed at Montpellier.
†Analysed at Hobart.
Recommended values (R.V.) are from Eggins et al. (1997) for BIR-1 and from Makishima & Nakamura (1997) for JP-1. Contamination-corrected (Fig. 10) abundances are: 0·06 ppm U and 28 ppm Sr in 4-36-90; 0·2 ppm U and 23 ppm Sr in 4-25-90; 0·05 ppm Pb in 39-86-2; 0·08 ppm Pb in 318-1.

interstitial material within some Spitsbergen xenoliths, in particular high Sr, Ba and U in the carbonate. Because this study is concerned with the composition of Spitsbergen peridotites before the late-stage formation of the interstitial materials, it is clearly important to establish their relative role in the whole-rock budget. Table 6 and Fig. 9a give results of a leaching experiment on sample 25, similar to those reported by Ionov *et al.* (1993*b*). Xenolith 25 has abundant interstitial material and higher modal carbonate than most other samples studied in this work (Table 1) and represents a 'worst case' example of their combined effects on whole-rock compositions. The leachate (in 10% HNO₃) from the crushed rock has very low abundances of REE, HFSE and Th but is strongly enriched in Sr, Pb, U, Ba and Rb. It is obvious that the spikes for those elements in the whole-rock pattern are mainly related to the interstitial material (Fig. 9a). On the other hand, the residue after leaching has small but conspicuous positive anomalies for the same elements indicating qualitative similarities between trace element signatures of the late-stage interstitial material and metasomatic patterns in the rest of the rock, as discussed by Ionov *et al.* (1993*b*).

We further address the role of interstitial 'contaminants' by plotting abundances of incompatible trace elements in the bulk rocks versus those in clinopyroxene and amphibole (Fig. 10). The majority of the data points plot along well-defined trends consistent with enrichments in LREE, Sr, Pb, Th and U mainly hosted by clinopyroxene and amphibole. Anomalously high Sr in two whole-rock samples is clearly related to their high modal calcite (Table 1), as for sample 25 (Fig. 9a), also reflected in elevated CaO on the CaO–MgO plot (Fig. 3c). Overall, the cases of anomalous whole-rock enrichments as a result of eruption-related metasomatism or post-eruption alteration are rare and taken into account below. Whole-rock abundances calculated from mineral and modal compositions commonly are close to those directly measured by solution ICP-MS (Fig. 9c), except for elements that tend to reside in interstitial micro-phases (Eggins *et al.*, 1998; Bedini & Bodinier, 1999; Garrido *et al.*, 2000; Kalfoun *et al.*, 2002).

The REE patterns of whole-rock xenoliths are similar to those of their clinopyroxenes (compare Figs 11a and 7a, and 11c and 7c). The Type-1 and Type-2 patterns can be easily identified from LREE–MREE relationships for most of the xenoliths, including those from the earlier work (Ionov *et al.*, 1993*b*). For some elements, in particular HFSE, their whole-rock abundances relative to those of adjacent REE are distinct from those for clinopyroxene, whose composition is significantly affected by partitioning into coexisting amphibole (Fig. 8c) and/or orthopyroxene (Rampone *et al.*, 1991; Ionov *et al.*, 1995; Eggins *et al.*, 1998; Garrido *et al.*, 2000; Tiepolo *et al.*, 2001). Whole-rock Type-1 xenoliths, unlike their clinopyroxenes, have
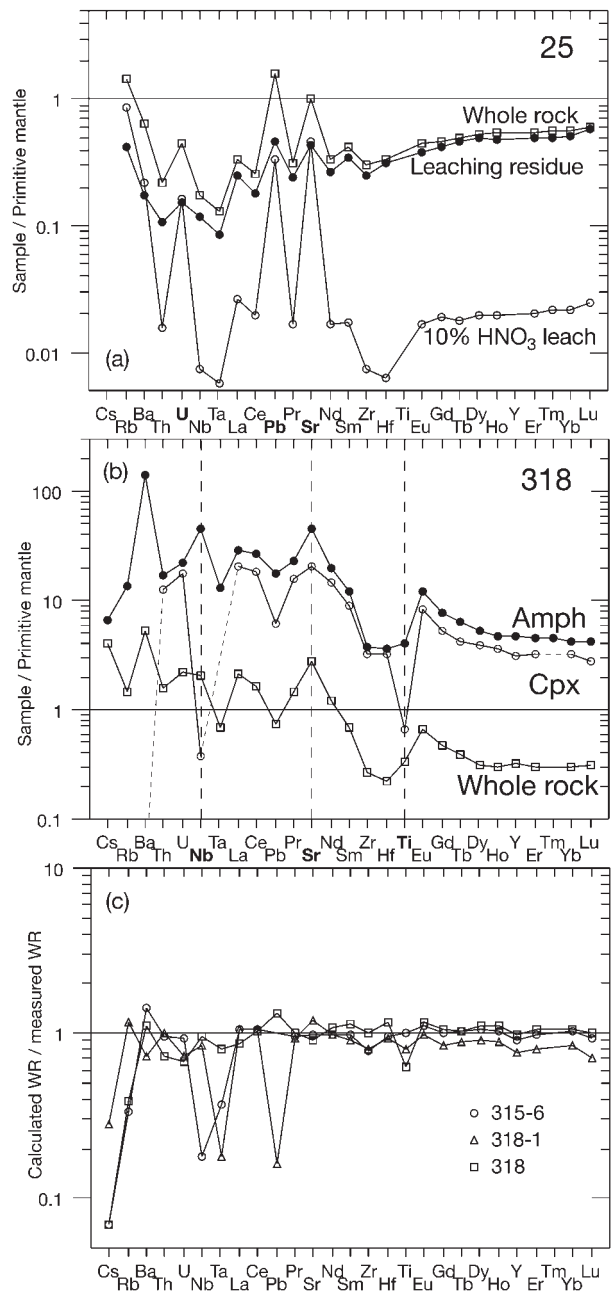
Fig. 9. Examples of trace element distribution between major minerals and interstitial material of the whole-rock xenoliths. (a) Whole-rock, residue after leaching and leachate (largely representing interstitial material) for carbonate-bearing sample 25. (b) Whole-rock, amphibole and clinopyroxene compositions for sample 318. (c) Ratios of trace element concentrations in three peridotites calculated from mineral analyses and modal compositions to the abundances obtained by whole-rock analyses. For most elements the ratios are within 1·0 ± 0·1, indicating that they largely reside in the major minerals. By contrast, a large proportion of Cs, Rb, Nb, Ta and Pb in some samples may reside in the interstitial material.

no or only minor negative Ti–Zr anomalies (compare Figs 7b and 11b). The low Ti/Zr values, common in
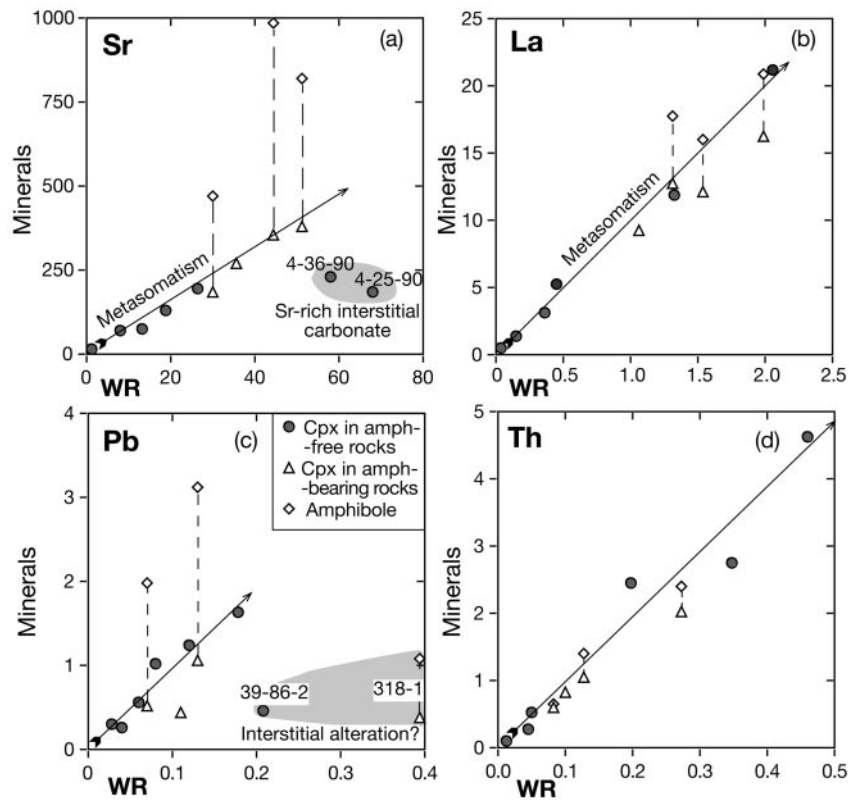
Fig. 10. Plots of Sr, La, Pb and Th concentrations in whole-rock xenoliths vs those in clinopyroxene and amphibole (minerals from the same sample are connected by dashed lines). Data points for most of the samples define trends (shown by arrows) consistent with element residence predominantly in clinopyroxene and amphibole. Outliers to the right of those trends are samples with high proportions of a given element in the interstitial material.

Type-2 clinopyroxenes (Fig. 7d) as a result of strong Ti partitioning into coexisting amphibole, are not seen in the bulk rocks. Similarly, whole-rock Type-2 xenoliths do not have negative Nb anomalies, and some yield high Nb/La and Nb/Th values. However, all Type-2 rocks have strong negative Ta anomalies, and therefore, high Nb/Ta ratios (Fig. 11d) consistent with data for amphiboles 318 (Fig. 9b) and 318-1, and clinopyroxene 311-9 (Table 4).

The abundances of moderately incompatible V, Sc, Y and HREE are lower than in fertile lherzolites worldwide and decrease with increasing MgO (Fig. 12). There are no differences in HREE and Y levels at similar MgO (or Mg#) between amphibole-bearing and amphibole-free peridotites, unlike for clinopyroxene (Fig. 6a). Similar to Ti, Zr abundances are much lower than in the primitive mantle (Fig. 13) and do not seem to be related to MgO (Figs 3d and 12). Abundances of Sr, LREE, Nb, Th, U, Ba and Rb vary widely and do not define coherent trends with MgO variations (Fig. 12). If samples with Sr-rich

interstitial material are discarded, Type-2 rocks show higher Sr (as well as Pr, Nd, Sm and Eu) than Type-1 rocks (Figs 12 and 13). The abundances of highly incompatible elements (La, Ce, Pb, Th and Ba) overlap in Types 1 and 2, but the two types are clearly discriminated on the La/Ce vs Nd/Yb plot; this demonstrates the strong LREE fractionation in Type-1 xenoliths. The two types are also distinguished on a plot of La vs Th (or U) because of higher Th at similar La in highly LREE-enriched Type-1 xenoliths (Fig. 13).

The distribution of Nb is distinct from that of Ti and Zr (Fig. 13). Ti and Zr are uniformly low in both rock types and do not seem to be affected by metasomatism. Nb abundances are usually much higher in Type-2 xenoliths, and show no correlation either with Zr or La and Th, elements that have relative peridotite–melt compatibility similar to that of Nb. The high Nb cannot be attributed to the presence of amphibole in the Type-2 xenoliths alone because amphibole-bearing xenolith 315-6 is as low in Nb as other Type-1 rocks. Zr/Hf and
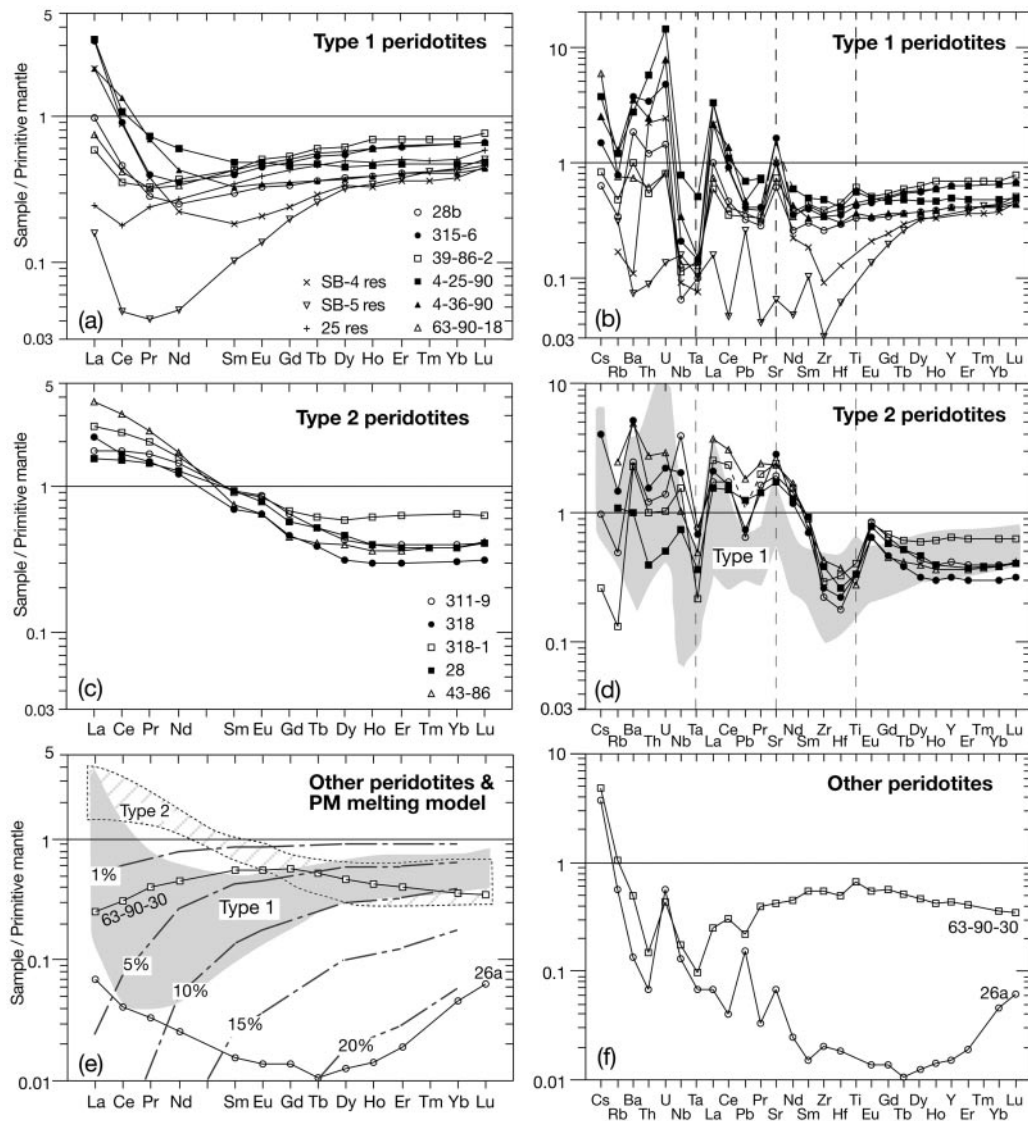
Fig. 11. Primitive mantle-normalized (Hofmann, 1988) REE and multi-element abundance patterns for whole-rock peridotites: (a) and (b) Type-1; (c) and (d) Type 2; (e) and (f) other samples and fields for Types 1 and 2. Dashed lines in (e) are compositions of residues of 1–20% of partial melting of primitive mantle (spinel lherzolite), calculated using algorithm and partition coefficients from Takazawa *et al.* (2000). Data for samples SB-4, SB-5, 28 and 43-86 are from Ionov *et al.* (1993*b*) (leached whole-rock compositions are shown for the Type-1 rocks to minimize effects of carbonate and other late-stage interstitial components).

Nb/Ta range from subchondritic in some Type-1 rocks to superchondritic in the rest of the xenoliths and are particularly high in Type-2 rocks (Fig. 13). Zr/Hf values are positively correlated with some incompatible elements, e.g. Nd, but vary broadly at similar Zr. By contrast, Nb/Ta increases with Nb abundances both in Type-1 and Type-2 rocks (Fig. 13). Ce/Pb is commonly below the PM value in both Type-1 and Type-2 rocks, which is also seen as negative Pb anomalies in Fig. 11d (when interstitial Pb contamination is taken into account).

CHEMICAL RECORD OF DEPLETION AND METASOMATISM
Evidence for partial melting and mineral–melt equilibria in chemical compositions

Abundances of major oxides and moderately incompatible elements in whole rocks and minerals vary systematically with variations in MgO contents and Mg# in most of the xenoliths (Figs 3, 4, 6a and 12). Such
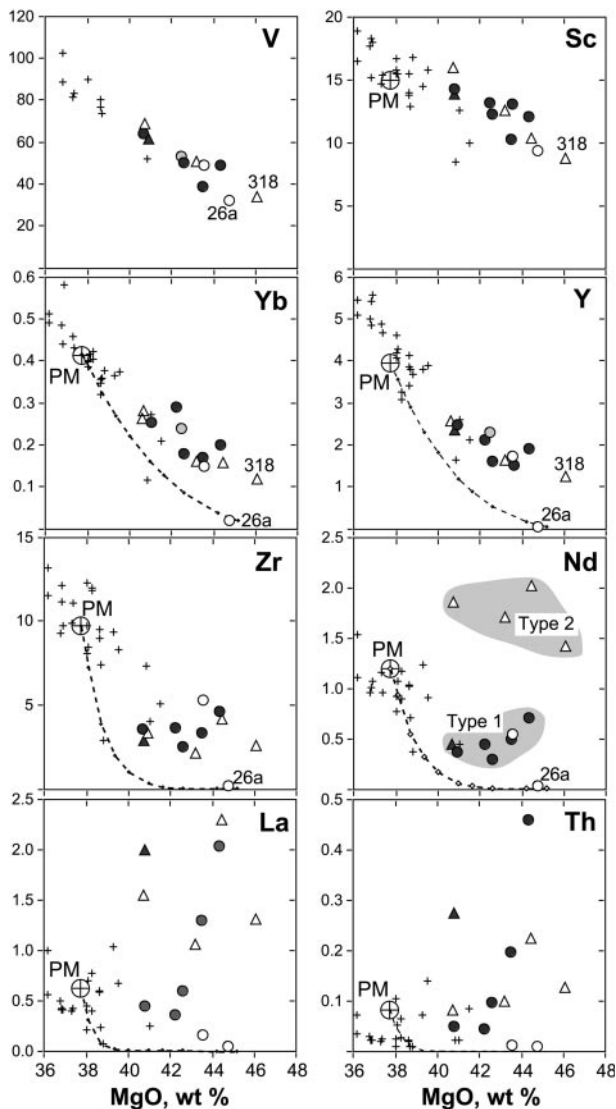
Fig. 12. Trace element abundances (in ppm) vs MgO (in wt %) in whole-rock peridotites: ●, Type-1 amphibole-free; ○, other amphibole-free; ▲, Type-1 amphibole-bearing; △, Type-2. +, compositions of unmetasomatized fertile lherzolites from central Mongolia (D. A. Ionov, unpublished data, 2000). PM, primitive mantle (Hofmann, 1988). Dashed lines are melt extraction trends at 1 GPa calculated using algorithm and partition coefficients from Takazawa et al. (2000).

trends are commonly interpreted as indicating that the peridotites formed as residues from variable degrees of partial melting and melt extraction from a fertile lherzolite source. This assertion is supported by abundant experimental and modelling results and data on natural peridotites [e.g. a recent review by Takazawa et al. (2000)].

Most of the Spitsbergen xenoliths plot close to calculated evolution lines for residual spinel peridotite at 1–2·5 GPa (Niu, 1997) on major oxide covariation diagrams (e.g. MgO vs CaO; Fig. 3c). Relatively high CaO

in several samples is due to late-stage precipitation of interstitial calcite. On Mg# vs Al_2O_3 and MgO vs FeO plots (Fig. 3a and b), the Spitsbergen peridotites fall within the compositional field of the Horoman peridotites inferred to have been derived by polybaric melting at 2·5–0·4 GPa. Takazawa et al. (2000) concluded from data on Mg–Fe partitioning that the Horoman peridotites with olivine Mg# and whole-rock MgO similar to those in the most depleted Spitsbergen xenoliths (26a and 318) have been produced by 19–25% of partial melting. Importantly, amphibole-bearing Spitsbergen peridotites plot within the compositional fields defined by the majority of the xenoliths and follow major oxide variation trends related to partial melting, indicating that amphibole precipitation was not accompanied by significant additions of 'basaltic' components (FeO, CaO, Al_2O_3, TiO_2). An apparent exception is sample 318 (with highest modal amphibole, >4%), which has Al, Ca and Ti abundances too high relative to MgO to be an unaltered melting residue; yet the very low FeO in sample 318 (Fig. 3b) rules out amphibole formation from an evolved, Fe-rich basaltic melt.

We calculated trace element abundances in residues after incremental (1% steps) partial melting of primitive spinel lherzolite using an algorithm and partition coefficients from Takazawa et al. (2000). Compositions of clinopyroxene and whole-rock samples from this study are compared with the calculation results in Figs 7e and 11e. The whole-rock abundances of HREE and MREE and Zr (elements least affected by metasomatism) are consistent with 3–11% of partial melting for Type-1 xenoliths and 5–12% for Type-2 xenoliths. The very low HREE values in harzburgite 26a cannot be reproduced by batch melting and require 20–25% of incremental partial melting (see also Fig. 12), consistent with its high whole-rock MgO, low whole-rock Ca, Al and Ti, low modal clinopyroxene (2·9%), and low Al, Ti and Na in the clinopyroxene (Fig. 4). Sample 318 has higher MgO and Mg# than 26a (Table 2). However, the degree of incremental melting estimated for amphibole-rich xenolith 318 from HREE abundances (∼12%) is much lower than for 26a, possibly as a result of REE enrichment by metasomatism.

Many Spitsbergen xenoliths plot off calculated partial melting trends on covariation diagrams of moderately incompatible elements vs MgO (Fig. 12). Similar features in other mantle peridotites were previously attributed to melting in the garnet stability field, variable amounts of trapped melt, changes in melting regime, etc. (e.g. Takazawa et al., 2000). Other processes, such as solid–melt mixing (Elthon, 1992) and solid–melt reaction (Kelemen et al., 1992; Van der Wal & Bodinier, 1996) may have accompanied or followed the partial melting and melt extraction. It is hardly possible, however, to better constrain melting conditions for the Spitsbergen peridotites
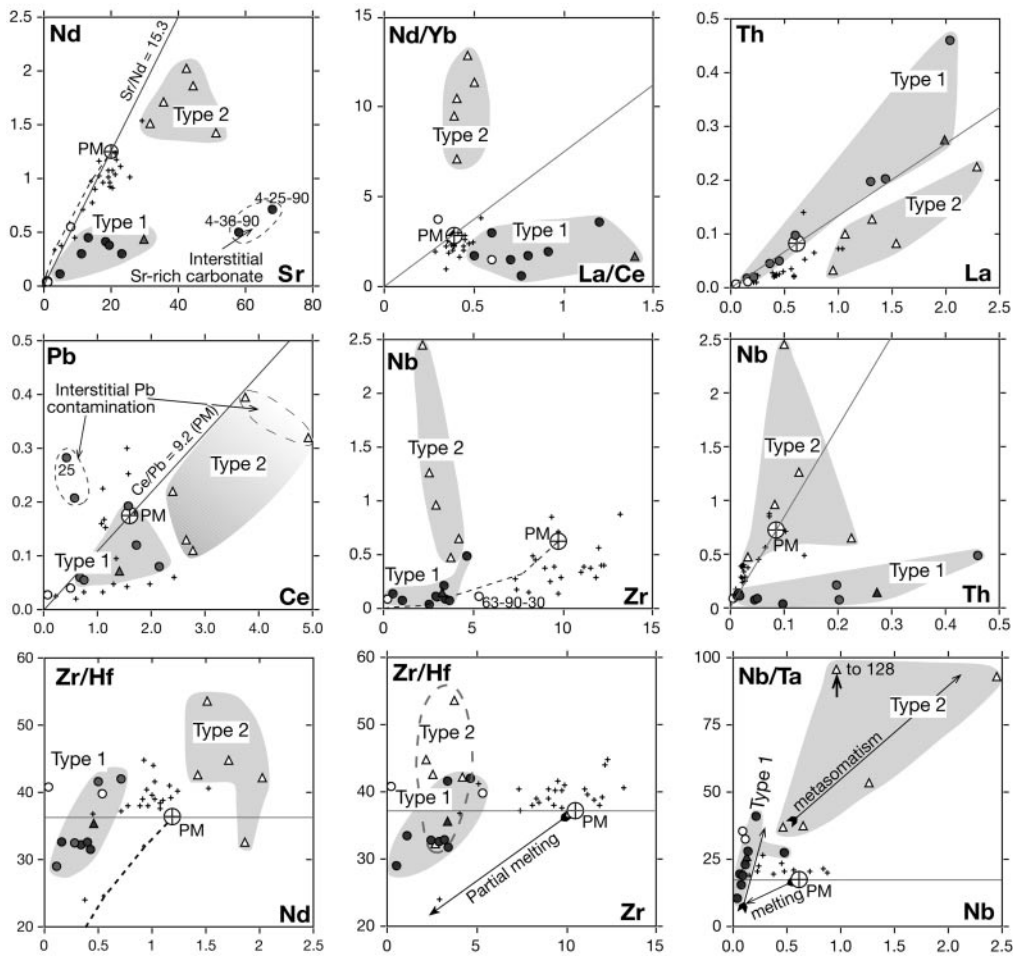
Fig. 13. Covariation plots for trace elements (in ppm) and their ratios in whole-rock peridotites. Symbols as in Fig. 12. Continuous grey lines show trace element ratios in primitive mantle. Arrows show possible trajectories of chemical change during melting and metasomatism.

because of widespread overprinting of the initial melting signatures by later metasomatism.

The convex-upward trace element patterns of whole-rock xenolith 63-90-30 (Fig. 11) and its clinopyroxene (Fig. 7) cannot be produced by partial melting and indicate equilibration with a melt that has lower Nb and LREE, and higher HREE than the host basalt (based on published $^{cpx/melt}D$; Fig. 14). Several other features also set that sample apart from the rest of the xenoliths: high whole-rock Ca/Al, high Ti in the bulk rock (Fig. 3d) and clinopyroxene (Fig. 4d), and high Cr# in clinopyroxene relative to spinel (Fig. 4c). However, the high Mg# in whole rock (0·909) and olivine (0·911) appear to rule out an origin from or equilibration with an evolved, Fe-rich basaltic melt.

Mineral compositions in composite xenolith 4-90-1 are distinct from those in the other xenoliths, in particular low Mg# and high Ti (Figs 4–7). That sample appears to be a fragment of a magmatic conduit system in the peridotite mantle. The modal gradient from dunite to wehrlite (Fig. 2c) may reflect different degrees of magma–host interaction in the cross-section of a magmatic channel (Kelemen, 1990), whereas abundant amphibole and phlogopite may be due to significant water and alkali contents of the magma and/or *in situ* crystallization of trapped fluid. Estimates of the trace element composition of a basaltic liquid in equilibrium with clinopyroxene 4-90-1 show strong enrichments in highly incompatible elements, with Th, U, Nb and LREE several times higher than in the basalts hosting the xenoliths (Fig. 14). The REE pattern of that hypothetical liquid is similar to calculated liquids for clinopyroxene from several Type-2 xenoliths (e.g. 311-9, Fig. 14a), except for somewhat higher LREE and MREE and lower HREE for cpx 4-90-1. The minor differences between the patterns calculated for clinopyroxene from the vein and from the Type-2 xenoliths could reflect local variations in metasomatic melt compositions. Alternatively, they can be explained assuming that the vein clinopyroxene equilibrated with an initial LREE-enriched melt (flowing
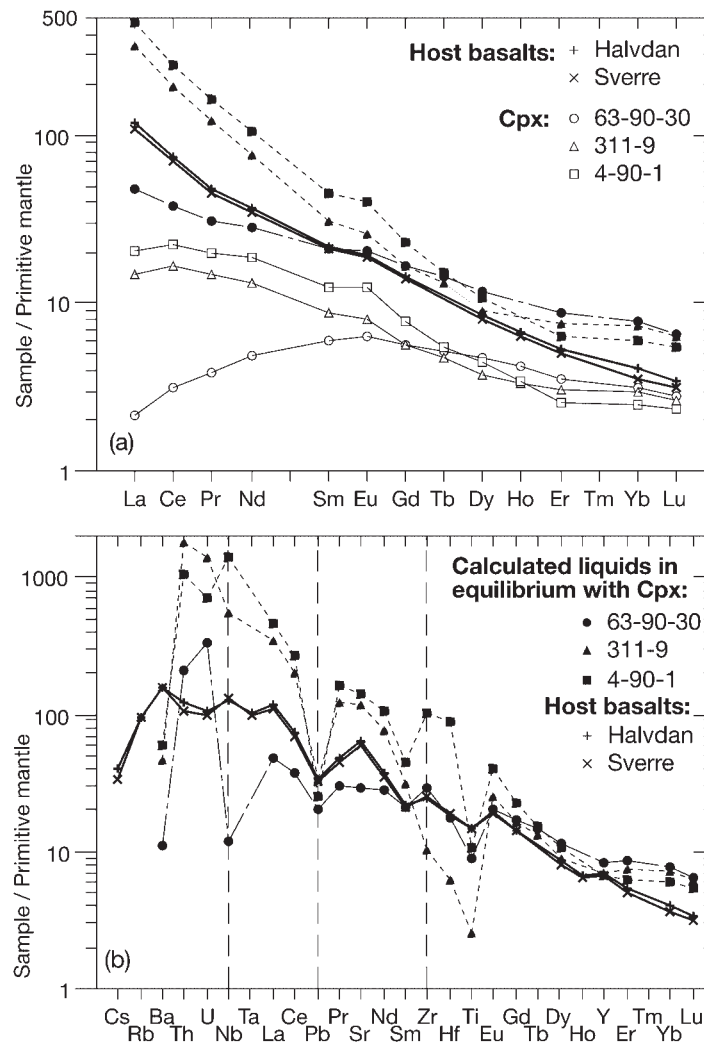
Fig. 14. Primitive mantle-normalized (Hofmann, 1988) trace element abundance patterns of average basalts from Halvdan and Sverre (black crosses and continuous lines). Also shown are: (a) clinopyroxene from three xenoliths (open grey symbols and lines) with REE patterns that indicate equilibration with melts; (a) and (b) hypothetical basaltic liquids in equilibrium with those clinopyroxenes (filled symbols and dashed lines) calculated using cpx–melt partition coefficients after Hart & Dunn (1993) and Vernières et al. (1997).

in a conduit), whereas clinopyroxenes in the peridotite xenoliths record equilibration (either partial or complete) with a melt modified during percolation from a conduit into the host peridotites. We conclude that a melt with REE abundances in equilibrium with vein cpx 4-90-1 could be an appropriate metasomatic agent for the Spitsbergen xenolith suite.

Mineral zoning and the timing of metasomatism

Strong compositional gradients between the depleted cores of minerals and their rims (in direct contact with an enriched melt) may develop during initial stages of metasomatism of melting residues. The lack of significant trace element zoning—even in large, porphyroblastic Type-1 clinopyroxenes (revealed by ion probe analyses, Table 5)—indicates that the mineral grains were internally homogenized by diffusion during or after metasomatism. The time required for homogenization is primarily dependent on diffusion coefficients and temperature as well as on the distance. We use here experimental data of Sneeringer et al. (1984) on Sr diffusion in natural diopside, which are consistent with Sr diffusion coefficients obtained on clinopyroxene (and amphibole) in other studies. Possible temperatures may range from $\geq 1200°C$ for metasomatism by a silicate melt to $\leq 1100°C$ for metasomatism by a carbonate-rich melt or fluid. The lower T values may be more appropriate in view of the experimentally determined amphibole

stability field in pyrolite compositions ($\leq 1050°C$) (Niida & Green, 1999) if it is applicable to less fertile Spitsbergen peridotites. The solution of Fick's equation given by Crank (1975) for Sr homogenization (from 45 to 181 ppm, to 95% of the final equilibrium level) to occur in a grain with a radius of 1–2 mm yields about 10^6 years for T in the range 1050–1100°C and $\geq 10^4$ years at 1200°C. These results further indicate that the metasomatism was not a very recent event related to formation of interstitial silicate glass and carbonate.

Trace element evidence for mechanisms and sources of metasomatism and its interpretation

Nearly all the xenoliths studied in this work show evidence for modal and/or cryptic metasomatism, which must have been widespread in the source regions of the xenoliths. In the discussion below we will focus on the nature of the metasomatism, leaving aside the few samples that do not bear well-defined enrichment signatures (26a, 63-90-30).

Geochemical evidence outlines two major types of the metasomatized rocks. One of them (Type-1) shows smaller and highly variable degrees of metasomatism, and only one xenolith from that group contains amphibole (with an unusually low K concentration). In contrast, all Type-2 xenoliths contain amphibole (some also have apatite) and show strong enrichments in some incompatible elements, with very similar enrichment patterns (Figs 6–8 and 11). Although trace element patterns and covariation plots (e.g. Fig. 13) clearly distinguish between the two groups, one cannot rule out that intermediate compositions also exist in the mantle beneath Spitsbergen, but are not represented in this sample series. Because both groups have similar equilibration temperatures, they appear to come from the same depth range in the uppermost mantle, but we have no information on specific spatial relationships between the two rock types, e.g. with relation to the sources of metasomatic media.

This study has to address two principal questions: (1) whether the two rock types were formed by two different mechanisms of metasomatism or, alternatively, reflect two distinct stages of the same mechanism (event); (2) whether distinct compositions (and sources) of metasomatic media were involved in the formation of the two rock types. The second question can be reworded as how to distinguish between metasomatic features produced by fractionation processes versus those that should be attributed to distinct metasomatic melt–fluid compositions.

These questions are addressed below using theoretical modelling of metasomatism. We first establish that simple mixing of depleted peridotites with melts enriched in incompatible trace elements cannot produce strong LREE fractionations and the diversity of enrichment patterns found in the Spitsbergen xenoliths. We then use numerical modelling to demonstrate that those features can be explained by chromatographic effects of melt percolation in peridotite matrix. Two modelling techniques are employed: (1) one-dimensional (1-D) melt percolation with fixed rock/melt ratios; (2) 'plate' models of reactive porous flow (percolative fractional crystallization). The results are presented in order of increasing model complexity, beginning with the REE distribution in spinel peridotites during melt percolation at constant rock/melt ratios. More complex models explore the effects of trapped melt, variable rock/melt ratios, distinct modal compositions of the peridotite, and the role of amphibole in element fractionation. These models are first run for REE to constrain their abundances in the initial metasomatic melt and outline the most likely physical parameters of melt percolation. We then introduce a broader range of elements (HFSE, Th, U and Pb) assuming that their ratios to adjacent REE in the initial melt are close to those in the primitive mantle. Finally, alternative melt compositions (with anomalies on PM-normalized diagrams for certain elements) are considered to provide the best fit between the models and the Spitsbergen xenoliths. For simplicity, a single set of mineral–melt partition coefficients ($^{\text{mineral/melt}}D_{\text{Element}}$) is used (Table 7), except for Nb and Ta in amphibole.

The origin of strong LREE enrichment and fractionation in the Spitsbergen xenoliths

The strongly fractionated LREE patterns of several Type-1 xenoliths with extremely high La/Ce, La/Pr and La/Nd ratios provide key evidence for their mode of origin. These extreme fractionations between individual REE do not appear to have analogues among any type of terrestrial magma. Therefore, such REE patterns in xenoliths cannot be modelled by simple mixing between LREE-depleted residues of partial melting and a magmatic liquid. Figure 15 demonstrates that mixtures of a model LREE-depleted peridotite with either host basalt or a hypothetical highly LREE-enriched liquid (in equilibrium with vein 4-90-1, Fig. 14) cannot reproduce high La/Ce or Sr/Nd ratios in typical Type-1 rocks. Furthermore, the ratios of highly incompatible elements in the mixing models are nearly uniform for moderately to highly enriched compositions (resulting in subparallel LREE–MREE patterns) because they are dominated by those in the liquid. By contrast, the LREE patterns and La/Ce, La/Nd and other ratios vary broadly among individual Type-1 xenoliths and seem to require a specific liquid composition for each sample in the mixing models. Finally, Navon & Stolper (1987) have demonstrated that

Table 7: Mineral–melt partition coefficients and initial peridotite and melt compositions (ppm) used in the modelling

| | Partition coefficients ($D^{mineral/melt}$) | | | | | Peridotite matrix | | Percolating melt | |
	cpx	opx	olivine	spinel	amph	fertile	refractory	vein model	'best fit'
Th	0.012	0.00003	1E − 07	1E − 08	0.0145	0.00038	0.00003	47.9	47.9
U	0.0103	0.00004	1E − 07	1E − 08	0.0125	0.00016	0.00001	11.8	11.8
Nb	0.0077	0.0005	0.0002	0.001	0.20	0.01	0.0007	299	299
Ta	0.02	0.001	0.0004	0.002	0.20	0.001	0.00007	17.2	5.7
La	0.054	0.0002	0.0001	0.0004	0.086	0.033	0.003	234	234
Ce	0.086	0.0004	0.0002	0.0005	0.138	0.160	0.013	391	391
Pb	0.072	0.0012	0.0002	0.0007	0.18	0.024	0.002	31.5	15.7
Pr	0.139	0.0006	0.0003	0.00065	0.222	0.045	0.0053	36.5	36.5
Sr	0.128	0.0003	0.0001	0.0001	0.32	4.22	0.57	2500	4853
Nd	0.187	0.001	0.0004	0.00058	0.299	0.34	0.054	118	118
Zr	0.13	0.005	0.004	0.005	0.156	3.36	0.672	784	280
Hf	0.2	0.01	0.006	0.01	0.24	0.105	0.025	21.6	4.6
Sm	0.291	0.003	0.00044	0.00048	0.466	0.16	0.044	16.6	16.6
Eu	0.35	0.004	0.00056	0.00045	0.56	0.067	0.023	4.2	4.2
Ti	0.33	0.07	0.007	0.15	1.32	520	195	27300	19500
Gd	0.4	0.0128	0.00076	0.00042	0.64	0.26	0.107	10.0	10.0
Tb	0.429	0.0186	0.00104	0.00041	0.686	0.051	0.025	1.21	1.21
Dy	0.442	0.0261	0.0014	0.0004	0.707	0.36	0.192	6.36	6.36
Ho	0.439	0.0356	0.00184	0.00041	0.702	0.088	0.047	1.09	1.09
Er	0.436	0.0474	0.00236	0.00042	0.698	0.267	0.144	2.45	2.45
Tm	0.433	0.0617	0.00296	0.00045	0.693	0.042	0.023	0.36	0.36
Yb	0.43	0.0787	0.00364	0.00048	0.688	0.28	0.158	2.37	2.37
Lu	0.427	0.0986	0.0044	0.00053	0.683	0.043	0.024	0.35	0.35

References: $D^{cpx/melt}$ values for REE, Nb, Pb and Sr are from Hart & Dunn (1993); $D^{cpx/melt}$ values for Zr, Hf and Ti are from Johnson (1998); $D^{cpx/melt}$ values for Th and U are from Hauri *et al.* (1994); $D^{cpx/melt}$ values for Pr, Eu, Gd, Tb, Ho and Tm were obtained by interpolation of data for adjacent REE; $D^{cpx/melt}$ for Ta is from Lundstrom *et al.* (1998), consistent with average D_{Nb}/D_{Ta} ratios from Forsythe *et al.* (1994) and Blundy *et al.* (1998). $D^{opx/melt}$, $D^{ol/melt}$ and $D^{spl/melt}$ values are based on the $D^{cpx/melt}$ combined with $D^{cpx/opx}$, $D^{cpx/ol}$ and $D^{cpx/spl}$ values from peridotite xenolith studies after Bedini *et al.* (1997) and Vernières *et al.* (1997). Some of the original $D^{mineral/melt}$ values were rounded up or slightly modified to provide a consistent and smooth set of peridotite–melt partition coefficients. $D^{amph/melt}$ values were obtained from $D^{cpx/melt}$ based on mean amph/cpx ratios in Spitsbergen xenoliths for different groups of elements: 1.2 for Th, U, Zr and Hf; 1.6 for REE; 2.5 for Pb and Sr; 4 for Ti; 10 for Ta; 26 for Nb.

plots of LREE vs MREE for peridotite suites with LREE enrichment patterns similar to those in this work do not form linear arrays expected in the case of simple mixing.

Similarly, it is unlikely that an exotic metasomatic fluid with extreme LREE fractionations and very high LREE/HREE (implied in mixing models) could form in equilibrium with any common mantle rock type. It follows that possible origins for the trace element patterns of Type-1 xenoliths may be related to enrichment processes rather than to unusual metasomatic source compositions. The key idea is that some metasomatic mechanisms may generate a range of fractionated REE patterns in the course of an enrichment event from a single initial LREE-enriched liquid.

The REE patterns of Type-1 xenoliths are very similar to those produced by modelling chromatographic effects during melt percolation (Navon & Stolper, 1987; Bodinier *et al.*, 1990; Vasseur *et al.*, 1991; Takazawa *et al.*, 1992) and appear to show evidence for interaction with percolating LREE-rich melts (Fig. 16). The 'chromatographic' models imply that the behaviour of elements during melt percolation in residual peridotites is controlled by mineral–melt partition coefficients. Elements with higher $^{rock/melt}D$ values, such as HREE, are selectively removed
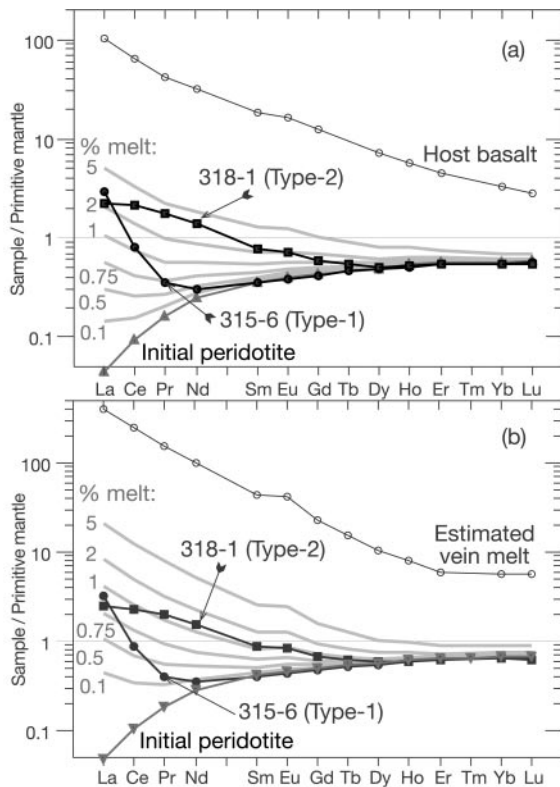
Fig. 15. Primitive mantle-normalized (Hofmann, 1988) REE abundance patterns of mixing products (grey lines) of a model LREE-depleted peridotite with: (a) average host basalt (melt proportion in wt %); (b) calculated melt in equilibrium with vein cpx 4-90-1 (see Fig. 14). Comparison with representative whole-rock xenoliths (continuous black lines and symbols) shows that peridotite–melt mixing models cannot reproduce either Type-1 or Type-2 patterns.

from the percolating melt by interaction with minerals in the host peridotite so that the melt at the percolation front becomes progressively enriched in the most incompatible elements relative to the less incompatible elements. As a consequence, an advancing metasomatic percolation front first produces enrichments in the most incompatible elements followed by enrichments in the less incompatible elements, thus creating transient metasomatic zoning with different enrichment patterns as a function of the distance from the magma source (Fig. 16b).

At an advanced stage of metasomatism, xenolith compositions approach chemical equilibrium with the migrating liquid (e.g. Navon & Stolper, 1987; Bodinier *et al.*, 1990; Vasseur *et al.*, 1991), with REE patterns similar to those of Type-2 xenoliths. It may be possible therefore to explain the whole range of REE patterns in the Type-1, Type-2 and vein samples by a single mechanism of metasomatism assuming that xenoliths with different REE

patterns 'sample' different zones in percolation systems (Fig. 16c). This hypothesis will be tested below using numerical modelling.

MECHANISMS AND SOURCES OF METASOMATISM IN THE CONTEXT OF NUMERICAL MODELLING

One-dimensional melt percolation models and the origin of Type-1 and Type-2 REE patterns

Were Type-1 and Type-2 metasomatic patterns formed in the same event and by the same process? To address that question we performed numerical simulation of REE and Sr distribution during 1-D porous melt flow in peridotite (Vasseur *et al.*, 1991) suited to the xenolith series in this work. The principles of the modelling are illustrated in Fig. 16a and b; modelling parameters and results are presented in Fig. 17 ('1-D.p' models). Two initial LREE-depleted peridotite compositions representative of the modal variation range in the Spitsbergen xenoliths were used (Table 7), one 'fertile' (11% cpx) and one 'refractory' (6% cpx), based on estimates of element abundances in partial melting residues (Fig. 11e). The presence of amphibole in the rocks does not significantly affect comparisons with modelling results for REE and can be simply considered equivalent to higher modal clinopyroxene because REE patterns in amphibole are nearly parallel to those in clinopyroxene (Figs 8c and d and 9b). For percolating melt compositions we used that of average host basalt and a hypothetical melt in equilibrium with vein clinopyroxene 4-90-1 (Fig. 14, Table 7). These two compositions have smooth, LREE-enriched patterns and cover a range of PM-normalized abundances (from 3–5 for Lu to 100–500 for La). Sr was included in some of these models because its residence and behaviour in peridotites is similar to that of the LREE and because nearly all xenoliths have positive Sr anomalies.

The modelling using the host basalt composition (not shown) failed to yield high LREE–MREE abundances, like those in Type-2 and many Type-1 samples. For example, a melt in equilibrium with typical Type-2 sample 311-9 (probably located close to the melt source) must have LREE–MREE abundances much higher than those in the host basalt (Fig. 14). This modelling outcome is not surprising because the 'constant porosity' model we used does not involve fractional crystallization of the percolating melt and therefore cannot yield an increase in its element abundances. The element fractionation in such models is produced because the abundances of more compatible elements in the melt near the percolation front decrease (because of their partitioning to the matrix)
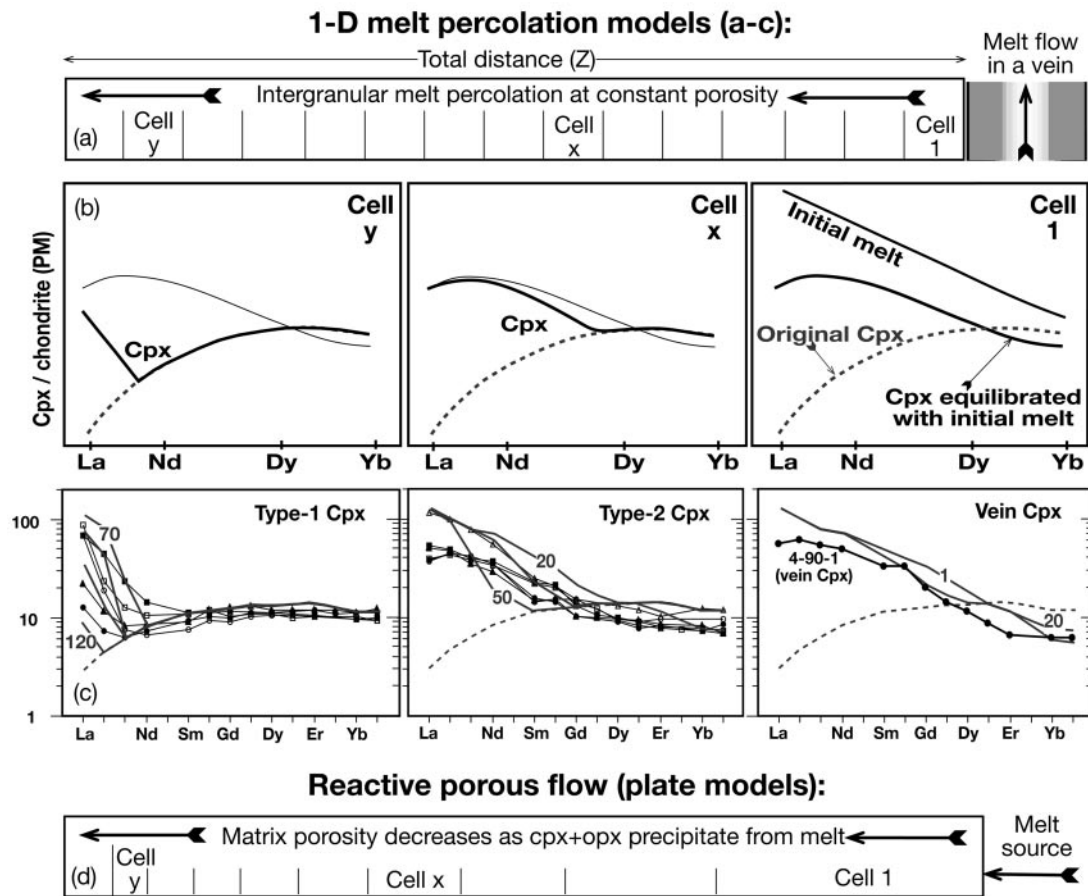
Fig. 16. A scheme and REE pattern diagrams illustrating the principles of one-dimensional (1-D) porous flow modelling. (a) Melt percolates away from its source (e.g. a vein) in the intergranular space of host peridotite, which is assumed to have constant porosity and modal composition. Melt and peridotite equilibrate by diffusion; no minerals precipitate from the melt. The model calculates average compositions of clinopyroxene, bulk matrix (peridotite without percolating melt) and percolating melt at a given time after the start of percolation in a given number of 'cells' (equal distance intervals) within a percolation 'column' of a given total length (Z). (b) Host peridotite near the melt source (cell 1) soon reaches trace element equilibrium with the initial melt, whereas far from the source (cell y) both percolating melt and host peridotite are selectively enriched in highly incompatible elements relative to elements with lower compatibility as a result of 'chromatographic' effects of mineral–melt interaction (see text). (c) Comparison of REE patterns in Type-1, Type-2 and vein clinopyroxene in Spitsbergen xenoliths with results of 1-D numerical simulation of porous melt flow (using a model LREE-enriched melt composition) in an LREE-depleted lherzolite (13·5% cpx) for selected cells (numbered) after Bedini *et al.* (1997). (d) A schematic illustration of the principles of the reactive porous flow model used in this work (Vernières *et al.*, 1997). Unlike in 1-D modelling, the matrix porosity decreases as pyroxenes precipitate as a result of melt–matrix reactions, the total distance and duration are not defined, and the cell size decreases from the melt source to the end of the 'column'.

faster than those of less compatible elements. It follows that the concentrations of least compatible elements (e.g. La) in the initial melt should be sufficient to yield, by mineral–melt equilibria, the strongest metasomatic enrichments in those elements far from the melt source.

The models using the 'vein melt' composition (with higher LREE and MREE) yield good results for the fertile initial matrix, producing (at different distances from the melt source) both REE pattern shapes and concentrations typical of Type-1 and Type-2 rocks (Fig. 17a). It should be noted that mineral compositions for cells next to the melt source (e.g. cells 1 and 2 in Fig.

17a) approach equilibrium with the initial melt for all REE and may correspond to vein mineral associations (as in xenolith 4-90-1) rather than to Type-2 peridotites. The models with the refractory matrix also yield Type-1 and -2 REE patterns, but the highest LREE abundances they produce are only half of those with the fertile matrix because of lower modal cpx in the refractory peridotite (Fig. 17b).

This fairly simple method of modelling melt porous flow does not address some aspects of that process, but nevertheless clearly demonstrates several fundamental consequences of melt percolation in peridotites. First, a single initial liquid fractionates to produce a range of
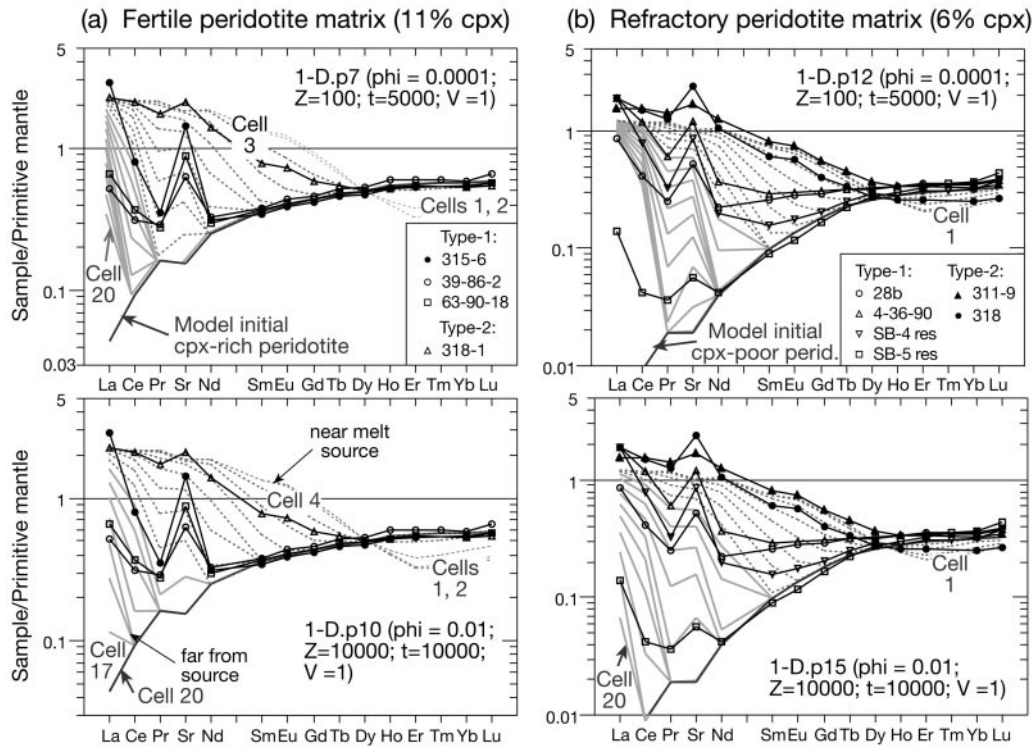
Fig. 17. Comparison of REE + Sr primitive mantle-normalized (Sun & McDonough, 1989) patterns in whole-rock xenoliths with results of 1-D numerical simulation of porous flow of an initial melt (similar to that in equilibrium with vein 4-90-1, as in Fig. 14) in a 'fertile' matrix (left: 11% cpx, 24% opx, 63% ol, 2% spl) and a 'refractory' matrix (right: 6% cpx, 22% opx, 70% ol, 2% spl). REE and Sr abundances in the matrix were calculated for appropriate residues after incremental partial melting (Fig. 11e). The mineral–melt partition coefficients are given in Table 7 and largely follow those from Vernières *et al.* (1997). Diffusivity in minerals is 10^{-14} cm^2/s; diffusivity in melt is 10^{-8} cm^2/s. Average radii of minerals are 0·05 cm for cpx and 0·2 cm for opx and olivine. Other model parameters are shown on each graph: φ, matrix porosity (melt fraction); Z, total percolation distance in cm; t, time after the start of percolation (in years); V, melt percolation velocity (in cm/year). Calculations in each model are performed for 20 distance increments (cells) within a given total distance, ranging from 5 cm (1-D.p7 and 12) to 500 cm (1-D.p10 and 15); some cells are numbered on the plots. Dashed grey lines show compositions of cells 1–10 (closest to melt source); continuous grey lines are compositions of cells 11–20 (far from melt source). (See Fig. 16 for explanations.)

element patterns, thus eliminating the need for multiple melt–fluid compositions in simple mixing models (Bodinier *et al.*, 1990). Second, highly fractionated element patterns are derived from 'conventional' initial melt compositions and do not imply the existence of exotic mantle sources capable of generating a highly fractionated liquid by equilibrium melting. Finally, strong element fractionation can be produced over relatively short distances, i.e. the same order of magnitude as metasomatic aureoles around magmatic veins in peridotite massifs (Bodinier *et al.*, 1990; Navon *et al.*, 1996; Zanetti *et al.*, 1996), contrary to the view that long percolation distances are required to produce significant 'chromatographic' effects (Nielson & Wilshire, 1993). Modelling percolation over distances from 1 to 100 m (Fig. 17a) has yielded similar results assuming that the distance to porosity ratio (Z/φ) remains the same. For instance, strong fractionation within 1 m is possible at ∼0·01% porosity, a low but physically realistic value (McKenzie, 1989).

Melt percolation over short distances, e.g. from a vein into host peridotite, is likely to involve partial melt crystallization and decreasing effective porosity along a temperature gradient. These effects cannot be fully reproduced in the 1-D porous flow model we used. However, an important step to more realistic modelling can be made assuming that percolation stops at a certain time and the fractionated melt present in the matrix is 'trapped', to be incorporated into the peridotite after recrystallization. Figure 18 presents modelling results analogous to those given in Fig. 17 except that the 'trapped melt' was added to whole-rock compositions ('1-D.tm' models). Because the trapped melt has much higher abundances of LREE and MREE than the matrix (because of low $^{cpx/melt}D$), these models may produce marked enrichments of these elements in the rocks compared with 1-D.p models, in particular for cpx-poor peridotites. The trapped melt effects are roughly proportional to matrix porosity and become significant
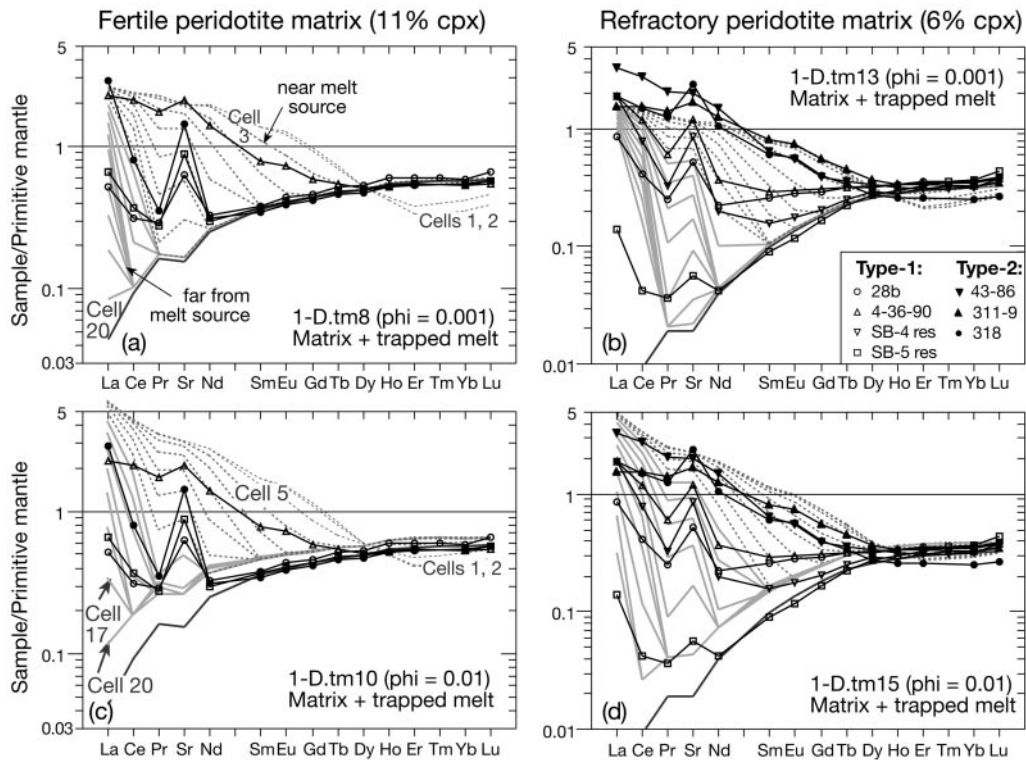
Fig. 18. Same as Fig. 17 except that modelling results were recalculated to obtain bulk compositions of the host matrix together with 'trapped' percolating melt ('1-D.tm' models). Data for Type-2 Spitsbergen xenolith 43-86 are from Ionov *et al.* (1993*b*).

at $\varphi \geq 0{\cdot}1\%$. 1-D porous flow models with trapped melt contents between 0·1 and <1% provide the best fit with REE data for the xenoliths in this work (Fig. 18). They can explain both strong LREE fractionation in Type-1 sample 315-6 (model 1-D.tm10) and a continuous increase in MREE and LREE abundances (model 1-D.tm15) in highly metasomatized Type-2 sample 43-86 (containing amphibole and apatite; Ionov *et al.*, 1993*b*) in a single event.

Reactive porous melt flow (plate models)

Vernières *et al.* (1997) developed a method of numerical simulation of porous melt flow, which they called a 'plate model', to account for variable matrix porosity, modal compositions and mineral precipitation or dissolution through matrix–melt reactions. The method assumes instantaneous melt equilibration as it moves from one matrix cell to another and therefore, by comparison with the 1-D models, disregards melt velocity, time and distance. A simplified version of that method is used here (Fig. 16d) as an alternative to the 1-D 'trapped melt' models. The plate modelling presented in Fig. 19 for the fertile and refractory matrices implies a decrease in porosity from 1% near the melt source to near zero

through precipitation of clinopyroxene and orthopyroxene as a result of olivine–melt reaction. Compared with 11% cpx and 24% opx in the initial fertile matrix, the reaction products contain 11·3–12% cpx and 24·4–25·4% opx, implying only very moderate changes in bulk-rock major oxide contents (e.g. increasing CaO by $\leq 0{\cdot}2\%$ and Al_2O_3 by $\leq 0{\cdot}12\%$).

The plate models produce both LREE enrichments and strong LREE fractionation far from the melt source as a result of 'percolative fractional crystallization' of the initial melt (Godard *et al.*, 1995; Bedini *et al.*, 1997), even for liquids with relatively moderate LREE abundances like the host Spitsbergen basalts. However, as in the 1-D modelling, combined LREE–MREE enrichments typical for Type-2 rocks are not likely to be generated with the host basalt as the initial melt. By contrast, the modelling using the hypothetical vein melt yields compositions that match very well those of both Type-1 and Type-2 rocks (Fig. 19). We conclude that the initial metasomatic melt was probably strongly enriched in LREE and MREE, with REE abundances similar to those in our 'vein model'. That inference only refers to the REE abundances and does not imply that the major and trace element composition of the metasomatic medium was identical to that of the parental melt of the vein 4-90-1.
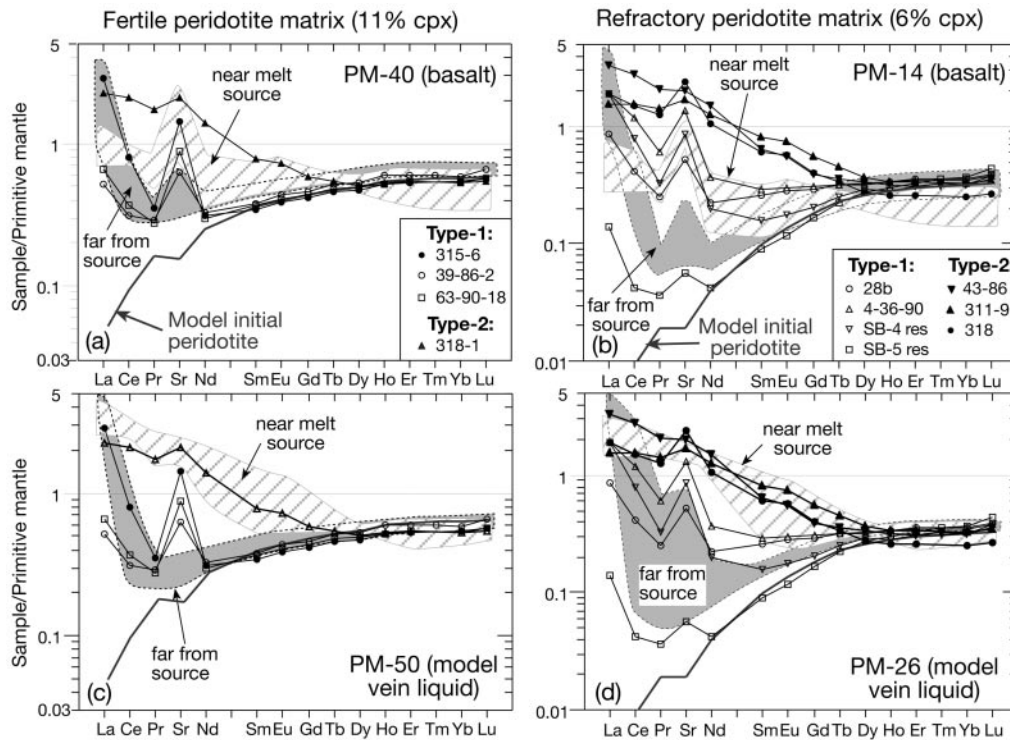
Fig. 19. Results of numerical simulation of reactive porous flow (plate model of Vernières *et al.*, 1997) in comparison with REE + Sr primitive mantle-normalized (Sun & McDonough, 1989) patterns in whole-rock xenoliths. Calculations are performed for 100 increments (cells), with cell size decreasing from ∼10% of the column length in cell 1 to ∼0·008% in cell 100. Initial matrix porosity of 1% decreases to near-zero as melt is consumed in the sliding reactions ranging from {1 melt + 0·18 olivine = 0·91 melt + 0·162 opx + 0·108 cpx} at the base of the column (cell 1) to {1 melt + 0·52 olivine = 0·74 melt + 0·468 opx + 0·312 cpx} at the top of the column (cell 100). The changing mineral proportions in these reactions were selected to provide for an evenly distributed decrease in porosity along the column. Initial melt and matrix compositions and mineral–melt partition coefficients are same as in Figs 17 and 18. For simplicity, results for cells 1–4 are grouped together as 'near melt source' field, results for cells 15–80 are grouped as 'far from source' field.

The cell size in the plate model we used decreases away from the melt source and therefore the number of cells with strong fractionation near the end of the percolation column is not representative of their fairly small volume. To illustrate relative proportions of corresponding rock types in the column, we calculated average compositions of clinopyroxene in 10% intervals of the total percolation column for model PM-50 (Fig. 19). The results (Fig. 20) show that some 40% of the column near the melt source (compositions 1–4) has a Type-2 REE pattern, whereas the far half of the column (compositions 6–10) has a Type-1 pattern. This is roughly consistent with the proportions of the two rock types in our xenolith suite.

Overall, either 1-D porous flow models with trapped melt or plate models (percolative fractional crystallization) can satisfactorily match the principal REE pattern types and enrichment levels in the Spitsbergen xenoliths. We conclude that REE patterns in the majority of the xenoliths can be explained by a single event and the same process: reactive porous flow. That process probably operated beneath an area on a scale of at least several

kilometres ('sampled' by two volcanoes) and may have ultimately produced metasomatism in a large portion of the lithospheric mantle. The metasomatic medium was strongly LREE enriched (with higher LREE and MREE abundances than in the host basalts).

Various 1-D and plate percolation models for REE and Sr yield minor positive Sr anomalies far from the melt source but cannot reproduce high Sr spikes common in Spitsbergen xenoliths (Figs 17 and 18). One possible explanation is that the $^{cpx/melt}D$ for Sr is close to that of Ce (rather than Pr in our modelling) as suggested by some experimental studies (Skulski *et al.*, 1994; Foley *et al.*, 1996). That inference implies a more incompatible behaviour of Sr during metasomatism than follows from compilations based on trace element systematics in oceanic basalts (Hofmann, 1988; Sun & McDonough, 1989) and appears to be supported by data on some cryptically metasomatized mantle peridotites (e.g. Ionov *et al.*, 1994; Vannucci *et al.*, 1998; Lenoir *et al.*, 2000). Plotting Sr between La and Ce on PM-normalized diagrams eliminates the Sr anomaly in many Type-1 samples. Regardless of
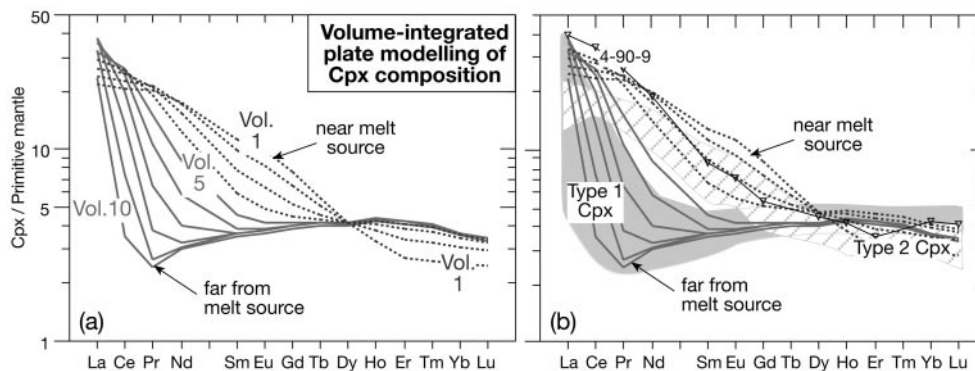
Fig. 20. (a) Results of numerical simulation of reactive porous flow (same as in Fig. 19) followed by calculation of average clinopyroxene compositions for 10 successive equal column volumes each making up 10% of the total. Volume 1 is closest to the melt source and approaches equilibration with the melt, volume 10 is farthest from the melt source. (b) Comparison of modelling results from (a) with fields of REE primitive mantle-normalized (Sun & McDonough, 1989) patterns in Type-1 and Type-2 clinopyroxene (see Fig. 7). LREE-rich cpx 4-90-9 is shown separately from other Type-2 samples. Model compositions 1–4 are similar to those of Type-2 cpx; compositions 5–10 match those of Type-1 cpx. It should be noted that REE abundances in some Type-2 clinopyroxenes may be lower than in the model results because of (1) preferential REE partitioning into coexisting amphibole and (2) the use of fertile initial matrix in this model whereas many Type-2 xenoliths are more refractory.

whether that observation is relevant, consistently high Sr/Nd values in strongly metasomatized Type-2 xenoliths (Fig. 13) appear to require a superchondritic Sr/Nd in the initial metasomatic liquid because Type-2 rocks approach equilibrium with that liquid. Lower $^{cpx/melt}D_{Sr}$ values than those used in our modelling would yield even higher Sr/Nd in the metasomatic liquid. Alternatively, $^{cpx/melt}D_{Sr}$ values could have been higher during the formation of Type-2 rocks than of Type-1 rocks (for example, as a result of changes in melt composition). However, variations in $^{mineral/melt}D$ values, e.g. those related to evolving melt compositions or temperature changes, were not considered in our modelling, to keep the models as simple as possible.

Effects of amphibole on REE–HFSE relationships

The example of Sr highlights multiple problems involved in modelling the behaviour of elements during metasomatism in comparison with REE of similar compatibility. Whereas REE patterns in initial melts are expected to be smooth, other elements may define anomalies relative to adjacent REE. Furthermore, partition coefficients of some elements are less precisely constrained or may vary with melt composition or other parameters in a different manner than those for REE (Lundstrom *et al.*, 1998). Metasomatic minerals may be strongly enriched in certain elements and therefore control their budget even when present only in small quantities (Kalfoun *et al.*, 2002). In particular, amphibole, a common metasomatic mineral in Spitsbergen xenoliths, has much higher abundances of Nb, Ta, Ti, Pb and Sr (but not

Zr, Hf, Th and U) than clinopyroxene (Fig. 8c). To explore the role of various factors in the behaviour of these elements in percolation metasomatism, we ran several 1-D porous flow models with and without amphibole. Element abundances in the fertile and refractory peridotite matrix were derived from those of adjacent REE to yield smooth depleted patterns on PM-normalized diagrams. Similarly, the composition of the percolating liquid was fixed to yield smooth enrichment patterns on PM-normalized diagrams, with Th/U, Nb/Ta and Zr/Hf values equal to those in the primitive mantle (Sun & McDonough, 1989) and no anomalies relative to adjacent REE. The matrix and melt compositions and partition coefficients are listed in Table 7.

The models without amphibole based on mineral–melt equilibria alone (no trapped melt) yield only moderate enrichments in Th, U and Nb (*a1* and *b1*; Fig. 21), which cannot match the high contents of these elements in strongly metasomatized xenoliths. The mismatch is even higher than for LREE (discussed in previous section) because of very low $^{cpx/melt}D$ values for Th, U and Nb. This problem is partially resolved if the interstitial melt is incorporated into the matrix, providing a good fit with the xenolith data for Th and U at matrix porosity 0·1–0·5% (*a2* and *b2*; Fig. 21). Nevertheless, the 'trapped melt' models cannot produce negative HFSE anomalies because, first, the initial liquid does not have them and, second, the behaviour of elements during percolation is largely controlled by their $^{cpx/melt}D$ values, which consistently decrease from HREE to Th and are not very different from those of adjacent REE (Table 7).

The only obvious way to fractionate HFSE from elements with similar $^{cpx/melt}D$ values by porous melt flow
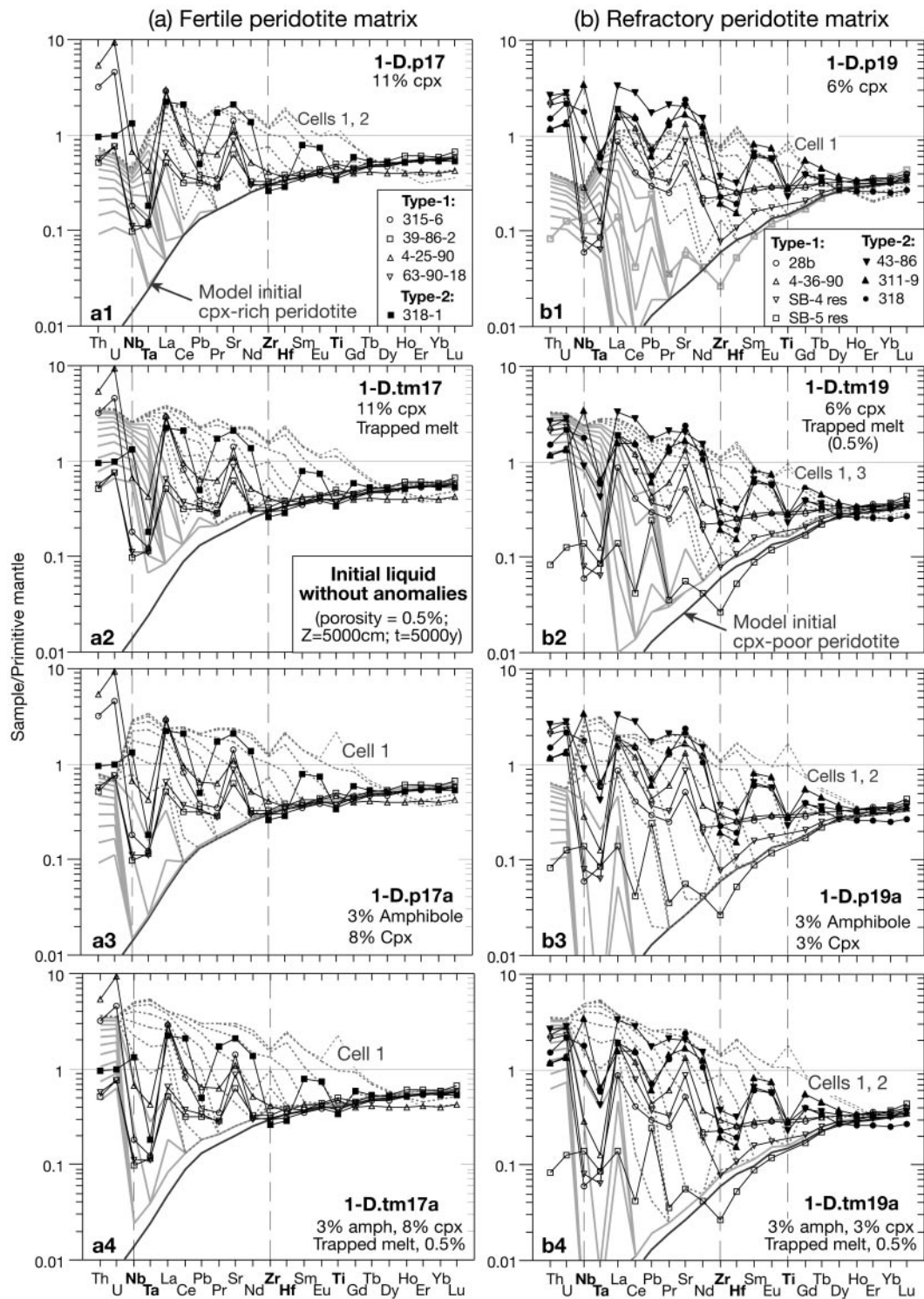
Fig. 21. Results of 1-D numerical simulation of reactive porous flow in comparison with primitive mantle-normalized (Sun & McDonough, 1989) trace element patterns (REE, Sr, HFSE, Th, U, Pb) in whole-rock xenoliths. Models 2 and 4 include trapped melt. Peridotite matrix in models 3 and 4 contains amphibole: 3% amph, 8% cpx in 'fertile' and 3% amph, 3% cpx in 'refractory'. Modelling parameters: porosity, 0·5%; distance, 50 m; time, 5000 years; melt velocity, 1 cm/year. (See Table 7 for partition coefficients.) Symbols are the same as in Figs 17 and 18. It should be noted that mineral compositions for cells next to the melt source (commonly cells 1 and 2) approach equilibrium with the initial melt for all REE and may correspond to vein mineral associations (as in xenolith 4-90-1) rather than to Type-2 peridotites.

(assuming smooth distribution patterns in both initial matrix and melt) is by means of a mineral with higher D_{HFSE} values than for clinopyroxene. Recent experimental work (Tiepolo *et al.*, 2000*b*) has yielded generally higher $^{amph/melt}D$ values for Nb and Ta (0·1–1·6) than for La and Th and also confirmed that $D_{Nb,Ta}$ and D_{Ti} are much higher for amphibole than for clinopyroxene, as indicated earlier by natural amph–cpx pairs in mantle rocks (Ionov & Hofmann, 1995). We derived $^{amph/melt}D$ values (Table 7) from those for clinopyroxene based on mean amph/cpx ratios in Spitsbergen xenoliths for different groups of elements: 1·2 for Th, U, Zr and Hf, 1·6 for REE, 2·5 for Pb and Sr, and 4 for Ti. $^{amph/melt}D$ values for Nb and Ta were both fixed at 0·2. These values are 10–26 times higher than for clinopyroxene, yet are conservative in view of the generally very high amph/cpx ratios (Fig. 8c). The bulk $^{matrix/melt}D$ values are somewhat higher for Ta than for Nb, both in amphibole-bearing and in amphibole-free peridotites, because of higher $^{cpx/melt}D$ values for Ta than for Nb.

We prefer to derive $^{amph/melt}D$ values from $^{cpx/melt}D$ values and the amph/cpx ratios in the xenoliths (rather than use experimental $^{amph/melt}D$ data), so as to have an internally consistent set of partition coefficients for these two minerals that host most of the REE and the HFSE in the peridotites. This work aims to constrain general features of trace element behaviour during melt percolation (based on a generalized set of $^{mineral/melt}D$ values) rather than to evaluate $^{amph/melt}D$ values from specific experimental studies. Experimental $^{amph/melt}D$ values vary broadly as a function of SiO_2 in the melt and Mg# and TiO_2 in amphibole (Tiepolo *et al.*, 2000*a*, 2000*b*). Few data are available for amphiboles with high Mg# and, in particular, low TiO_2 as in the Spitsbergen xenoliths. Nevertheless, the $^{amph/melt}D$ values we used are within the ranges reported by Tiepolo *et al.* (2001) for amphiboles with Mg# $\geq 0·74$: 0·2 vs 0·06–0·23 for Nb and Ta ($D_{Nb/Ta}$ 0·7–1·2); 0·16 vs 0·15–0·51 for Zr; 0·24 vs 0·24–0·95 for Hf. The higher D_{HFSE} values of Tiepolo *et al.* (2001) are for Ti-rich (>6% TiO_2) amphiboles, whereas the amphiboles in the Spitsbergen peridotite xenoliths have <1·5% TiO_2.

The 1-D models were rerun with 3% amphibole and 8% clinopyroxene in the fertile matrix and 3% amphibole and 3% clinopyroxene in the refractory matrix. The models with amphibole (*a3*, *a4*, *b3* and *b4*; Fig. 21) show little difference for LREE, Th and U but indicate a dramatic change in the behaviour of Nb and Ta. Because $D_{Nb,Ta}$ values for amphibole are higher than for clinopyroxene, the bulk matrix–melt partition coefficients for Nb and Ta increase and 'slow down' the Nb–Ta enrichment front in the percolating melt relative to other highly incompatible elements. This produces negative Nb anomalies far from the melt source, similar to those in Type-1 xenoliths, and moderate to high Nb/Th and

Nb/La ratios (i.e. positive Nb–Ta anomalies) close to the source, as in Type-2 rocks. Models with higher modal amphibole (5%) and higher $^{amph/melt}D_{Nb,Ta}$ values (0·5) yield similar results (not shown). We emphasize that the negative Nb–Ta anomalies far from the melt source are a signature of the fractionated melt produced by percolation through the amphibole-bearing matrix closer to the source and are not related to the presence or absence of amphibole in that zone. Therefore, both amphibole-bearing and amphibole-free peridotites far from the source should have low Nb/Th and Nb/La, as in the Type-1 xenoliths.

The modelling of Nb–Ta behaviour during porous melt flow hinges critically on assumptions about the partitioning of these elements (in comparison with LREE, Th and U) between mantle minerals and metasomatic media. Experimental work has shown that D_{HFSE} values may be strongly affected by major element composition of minerals and the silicate melt (Lundstrom *et al.*, 1998; Tiepolo *et al.*, 2000*b*), proportion of carbonate component in the melt (Blundy & Dalton, 2000) or a transition from a silicate melt to a supercritical fluid. Combined effects of these factors are hard to assess but there is little doubt that $^{amph/melt}D$ values for Nb and Ta are significantly higher than $^{cpx/melt}D$. Notably, xenolith studies consistently report very high amph/cpx ratios for Nb and Ta (indicating high $^{amph/melt}D_{Nb,Ta}$), whereas experimental work yields moderate $D_{Nb,Ta}$ values, at least for Mg-rich amphiboles typical for mantle peridotites (Green, 1995). Ionov & Hofmann (1995) suggested that precipitation of Nb,Ta-rich vein amphibole (and phlogopite) from migrating melts may produce negative Nb–Ta anomalies in residual liquids whereas Tiepolo *et al.* (2000*b*) argued that experimentally determined $^{amph/melt}D_{Nb}$ values for Mg-rich systems are not high enough relative to $^{amph/melt}D_{La}$ to effectively fractionate these elements by peridotite–melt equilibria. Our modelling shows that melt percolation in amphibole-bearing peridotites can fractionate Nb from La and Th even at small differences in bulk matrix–melt partition coefficients (in the same manner as La–Ce–Pr are fractionated, Figs 17–19). This happens because chromatographic effects enhance the effects of differences in $^{matrix/melt}D$ values and thus produce a wide range of Nb/(La, Th) values at different distances from the melt source (*a3–b4*; Fig. 21). Similarly, Bedini *et al.* (1997) showed that porous melt flow may create negative Nb–Ta anomalies far from the melt source if accessory minerals with high $D_{Nb,Ta}$ values (e.g. rutile) are present, even in very small amounts, in the percolation column. We conclude that melt percolation through amphibole-bearing rocks will inevitably decrease the abundances of Nb relative to those of Th and La and thus is likely to produce negative Nb anomalies in the melt.

Trace element composition of the initial metasomatic melt

The modelling with amphibole yields relatively high values for all HFSE and Pb in peridotites close to the melt source (cells 1–5 in Fig. 21). By contrast, most Type-2 xenoliths have negative anomalies for Ta, Zr, Hf, Ti and Pb, and only few samples have moderately high Nb/Th ratios. We have failed to reproduce the negative anomalies for these elements in Type-2 xenoliths with models that assume a fixed initial melt composition and vary other parameters within reasonable limits, even though these models yield a good match for other elements. If the initial melt has no anomalies for given elements, the only way to produce the negative anomalies close to melt source in the percolation models is to assume low $^{matrix/melt}D$ values for those elements (relative to adjacent REE). As discussed above, that is not likely for HFSE in amphibole-bearing rocks and, furthermore, low $^{matrix/melt}D_{HFSE}$ values may result in positive HFSE anomalies far from the melt source, which are not observed in the Type-1 rocks. More complex models, involving intermittent precipitation of various accessory minerals (Bedini *et al.*, 1997), variable partition coefficients, transition from a melt to fluid within a percolation column (Ionov & Hofmann, 1995), etc. are beyond the scope of this paper.

However, 1-D percolation models using a liquid with negative Ta, Zr, Hf, Ti and Pb anomalies, a positive Sr anomaly and high Zr/Hf and Nb/Ta ('best-fit' in Table 7) have reproduced both Type-1 and Type-2 patterns for nearly all elements (Fig. 22). This leads us to conclude that the simplest way to explain the negative anomalies in Type-2 rocks is for the initial melt to be markedly depleted (relative to adjacent REE) in Ta, Zr, Hf, Ti and Pb and to assume that they approached equilibrium with that liquid (e.g. 311-9 in Fig. 14b). In other words, the distribution of Ti, Zr, Hf, Ta and Pb in Type-1 and Type-2 xenoliths can be explained if one assumes that these elements are not significantly affected by metasomatism (because of their low abundances in the percolating liquid). In such a case, increasing REE contents imposed by an REE-rich liquid would result in negative anomalies of Ti, Zr, Hf, Ta and Pb (whose contents do not increase), typical of Type-2 rocks, and even deeper anomalies in clinopyroxene (as a result of partial redistribution to amphibole).

The assumption of high Zr/Hf in the initial melt can also explain the positive Nd–Zr/Hf correlation and the lack of Zr–Zr/Hf correlation in Fig. 13. Zr/Hf must be subchondritic in partial melting residues (as in some Type-1 rocks) because of lower $^{cpx/melt}D$ values for Zr than for Hf (Lundstrom *et al.*, 1998; Takazawa *et al.*, 2000; Kalfoun *et al.*, 2002) and is increasingly buffered by the metasomatic liquid with superchondritic Zr/Hf in more strongly metasomatized Type-2 rocks without significant increases in Zr abundance. The situation is different for the Nb–Ta pair because Nb has negative anomalies in Type-1 xenoliths but positive anomalies in some Type-2 rocks. Moreover, Nb abundances and Nb/Ta values are positively correlated (Fig. 13), consistent with both high Nb and very high Nb/Ta in the melt.

The assumption of very high Sr and Sr/Nd in the initial melt does not provide a completely satisfactory match of modelling results with the xenolith data. The models yield positive Sr anomalies close to the melt source (Fig. 22) and therefore provide a better match with Type-2 samples than models in Fig. 21. However, they typically yield higher Sr abundances and Sr/Nd values than in Type-2 xenoliths, indicating that the Sr/Nd in the initial melt was overestimated. On the other hand, even those high Sr/Nd values in the initial melt fail to result in marked positive anomalies far from the melt source to match the very high Sr/Nd in most Type-1 rocks. In general, positive anomalies for a highly incompatible element both near and far from the melt source do not appear to be a likely feature of the metasomatism by melt percolation.

Overall, the theoretical modelling strongly suggests that both Type-1 and Type-2 trace element patterns in the Spitsbergen xenoliths may have been produced by the same metasomatic mechanism and possibly in the same event. The Type-1 REE patterns may have been derived by small-scale reactive porous flow metasomatism at the percolation front, whereas large-scale rock–melt interaction close to the melt source, probably approaching equilibration with the percolating melt, produced Type-2 patterns. Evidence from other elements is quantitatively consistent with such a model, assuming amphibole precipitation and an initial melt depleted in Ta, Zr, Hf, Ti and Pb and enriched in Sr (relative to adjacent REE). It is likely that crystallization of amphibole in wall-rock peridotite (Type-2) exhausted water from the percolating liquid so that at larger distances from the melt source the water-poor liquid or fluid produced largely 'anhydrous' Type-1 metasomatic assemblages. The melt/rock ratio may have continuously decreased as well.

The nature of the metasomatic media and their fingerprints in the metasomatic rocks

The nature of the percolating melts can be constrained from the mineralogical and chemical compositions of the xenoliths. It is unlikely that the melt or fluid responsible for the formation of Type-1 rocks was rich in alkalis and water because 'hydrous' phases are normally not present and the only amphibole from a Type-1 sample is very low in K. An Fe–Ti-rich silicate melt is not a likely option
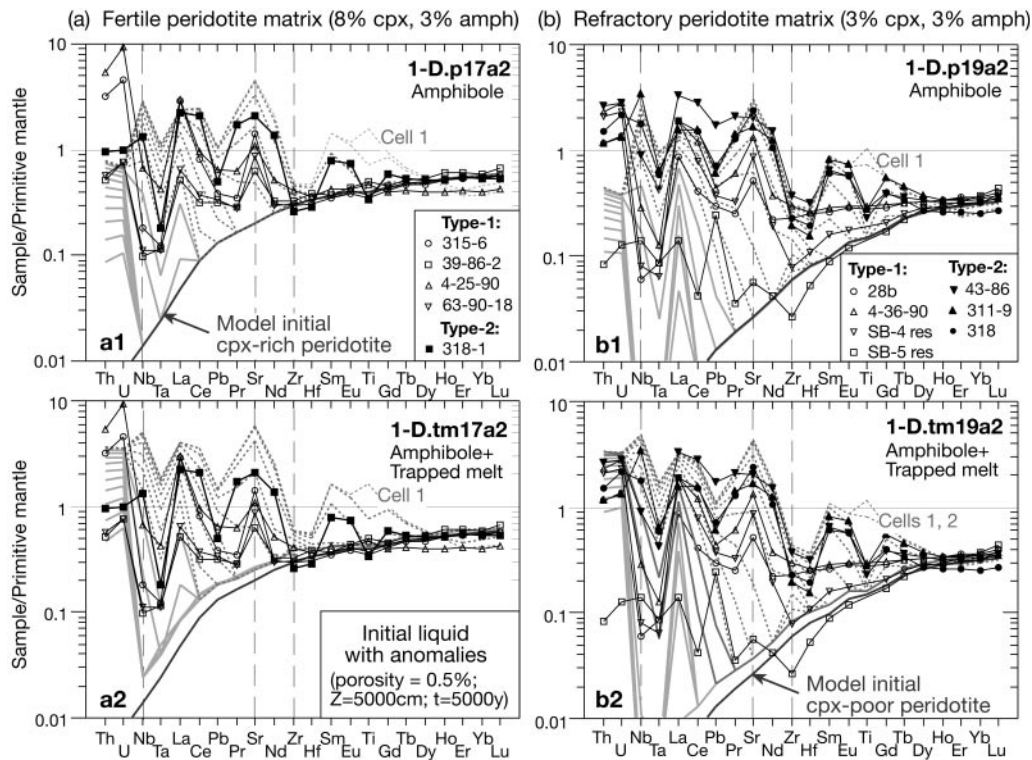
Fig. 22. One-dimensional percolation models for amphibole-bearing peridotite matrix with and without trapped melt for the 'best-fit' initial melt composition (with anomalies). Other modelling parameters are the same as in Fig. 21.

either because rocks with the highest LREE enrichments and high modal amphibole do not show concomitant enrichment in Fe and Ti (Fig. 3b and d). In particular, Type-2 rocks contain a high incompatible element contribution from the metasomatic media and must have been formed by deep interaction of peridotitic residues with melts. The lack of Fe–Ti enrichments in these rocks is a strong argument for carbonate-rich metasomatic media because primary carbonatites are characterized by elevated Mg# values in the range 0·8–0·9 (Dalton & Wood, 1993; Sweeney, 1994). Carbonate-rich melts are believed to be very efficient metasomatizing agents (Green & Wallace, 1988) because of a combination of high mobility (Hunter & McKenzie, 1989) and high incompatible element abundances imparted by low degrees of partial melting during their generation. For a silicate–carbonate liquid, a consequence of its reaction with host peridotite would be continuous exhaustion of its silicate component and increasing proportion of the carbonate component in its composition (Mattielli *et al.*, 1999), because carbonates are not stable in the shallow spinel peridotite mantle at moderate to high temperatures (Dalton & Wood, 1993).

Carbonate-rich melts, which may be strongly enriched in LREE and Sr and depleted in HFSE, were earlier proposed as likely metasomatic agents for peridotite xenoliths worldwide (Green & Wallace, 1988; Yaxley *et al.*, 1991; Dautria *et al.*, 1992; Hauri *et al.*, 1993; Rudnick *et al.*, 1993) including those from Spitsbergen (Ionov *et al.*, 1993b). Those inferences were based on comparisons of trace element patterns in metasomatized xenoliths with those of carbonatites exposed in the crust (Nelson *et al.*, 1988; Woolley & Kempe, 1989), experimental evidence on element partitioning between immiscible carbonate and silicate liquids (Hamilton *et al.*, 1989; Veksler *et al.*, 1998) and compositional variations in mantle-derived volcanic rocks (Dupuy *et al.*, 1992). Some of these constraints are poorly defined (Laurora *et al.*, 2001), e.g. the compositions of the crustal carbonatites may differ from those of primary carbonate liquids generated by mantle melting (Eggler, 1989; Ionov *et al.*, 1993b; Ionov & Harmer, 2002), and liquid immiscibility may not be a major factor in the carbonatite genesis (Lee & Wyllie, 1998). Direct evidence for trace element fingerprints of mantle-derived carbonate-rich melts was recently provided by experimental results of Blundy & Dalton (2000) and Adam & Green (2001). Their work demonstrated that cpx–melt partition coefficients for HREE, Ti, Zr and Rb are higher by factors of 5–200 for carbonate melts than for silicate melts, whereas partition coefficients

for LREE, Sr and Nb show less fractionation. Those workers inferred that low degrees of partial melting of carbonated mantle lherzolite should produce carbonate-rich melts with elevated incompatible element concentrations, steep REE patterns and marked depletions of Ti and Zr (but not necessarily Nb), consistent with signatures inferred for the initial metasomatic liquid in this study.

We would like to emphasize that the reactive porous flow is an essential mechanism to produce strong LREE fractionation (high La/Ce, La/Nd) and highly variable enrichment patterns in metasomatic peridotites (regardless of whether the metasomatic melt was carbonatite or silicate). As discussed above, no known type of mantle-derived melt, including carbonatites, is likely to produce REE + Sr patterns similar to those in Spitsbergen Type-1 xenoliths, either by simple mixing or equilibrium mineral–melt partitioning, without the chromatographic effects of melt percolation (see also Ionov *et al.*, 2002). Conversely, porous melt flow can fractionate silicate basaltic liquids to produce extremely high La/Ce and La/Nd ratios (Fig. 19). Therefore, it is more correct to attribute the U-shaped or 'spoon-shaped' REE patterns in mantle rocks [fig. 5g and h of Downes (2001)] to 'percolation' metasomatism rather than 'carbonatite' metasomatism even if carbonate-rich melts are considered the most likely candidates for the metasomatic media. Similarly, negative HFSE anomalies (e.g. low Nb/Th and Nb/La in Type-1 Spitsbergen xenoliths) can be related to chromatographic effects of porous melt flow (as a result of precipitation of amphibole near the melt source) and not be direct signatures of the initial melt (compare high Nb/Th in Type-2 xenoliths, Figs 11 and 13). These examples further demonstrate that fractionation processes may be as important as melt compositions in determining trace element signatures of the metasomatized mantle (Laurora *et al.*, 2001).

In general, the relative effects of the source composition and fractionation mechanisms in the metasomatism may change with distance from the melt source in a generalized 'metasomatic column': (1) peridotites hosting the feeder channel may undergo strong transformation (e.g. dissolution of orthopyroxene and formation of wehrlites as a result of reaction with carbonatites); (2) rocks in the vicinity of the feeder will approach trace element equilibrium with the melt or fluid and therefore acquire strong chemical fingerprints of the metasomatic agent (Type-2 Spitsbergen xenoliths); (3) trace element patterns farther in the metasomatic 'column' will be increasingly controlled by metasomatic fractionation mechanisms (Type-1 Spitsbergen xenoliths). Overall, different signatures of the metasomatic medium in a percolation column may be spatially detached, depending on relative matrix–melt element partition coefficients. We have

shown that marked trace element variations in the Type-1 peridotites could have been accompanied by only minor mineralogical and major element effects (precipitation of <1% clinopyroxene). It follows, for example, that the absence of characteristic major element (high Ca/Al) or trace element (low Ti/Eu or Zr/Sm) signatures inferred for high degrees of 'carbonatite' metasomatism in rocks far from the melt source (like Spitsbergen Type-1 xenoliths) does not rule out a carbonate-rich composition of the initial metasomatic medium.

LREE enrichments and negative HFSE anomalies in mantle rocks can possibly be implanted by subduction-related silicate melts or water-rich fluids (Zanetti *et al.*, 1999). These melts or fluids, in particular, are believed to be strongly depleted in Nb and Ta (high Th/Nb and La/Nb ratios) and enriched in Pb, Sr, Ba and alkalis (Nakamura *et al.*, 1985; Hofmann, 1988; Woodhead, 1989). However, negative Pb anomalies (high Ce/Pb) and high Nb abundances in Type-2 xenoliths (Figs 11 and 13) appear to argue against such an alternative. Peridotites enriched by subduction-related fluids should probably also show stronger enrichments in Rb and Cs (Churikova *et al.*, 2001) than most of the Spitsbergen xenoliths (note fairly low Rb and Cs contents in the amphiboles, Tables 4 and 5, Fig. 8b and d). Notably, a combination of depletion in Pb and enrichment in Nb is an unlikely feature to be found in mantle rocks metasomatized by subduction-related fluids.

SUMMARY

(1) The protolith for the lithospheric mantle beneath Spitsbergen was created by moderate to high degrees of partial melting and melt extraction from a fertile source. The melting residues were then metasomatized with melts or fluids that intruded the upper levels of the lithospheric mantle via a network of veins and high-porosity zones in the wall-rock peridotite.

(2) The initial melt was probably a carbonate-rich silicate liquid, strongly enriched in highly incompatible trace elements, with negative anomalies of Zr, Hf, Ta, Ti and Pb and a small positive anomaly of Sr relative to adjacent REE, and with high Nb/Ta and Zr/Hf ratios. An involvement of subduction-related melt source is not likely.

(3) The reactive porous flow in the vicinity of conduits that involved crystallization of amphibole created metasomatic patterns approaching equilibrium with the initial melt. Melt composition evolved continuously as its fraction decreased as a result of percolative fractional crystallization. At larger distances from the local melt sources the evolved liquid or fluid produced largely 'anhydrous'

assemblages with highly fractionated LREE. The metasomatic zoning in wall-rocks was 'frozen' when local sources of percolating melt were exhausted.

(4) Very high and variable La/Ce, La/Nd and possibly Sr/Nd ratios in LREE-enriched metasomatic peridotites worldwide are consistent with 'chromatographic' fractionation during reactive porous melt flow rather than simple mixing with an enriched melt (either silicate or carbonatite). Negative Nb–Ta anomalies far from the melt source can be produced by melt percolation through amphibole-bearing peridotites.

(5) Chemical and mineralogical fingerprints of a metasomatic medium are strongest near its source (e.g. a vein), whereas trace element patterns farther in the metasomatic 'column' are increasingly controlled by metasomatic fractionation mechanisms.

ACKNOWLEDGEMENTS

REFERENCES

Adam, J. & Green, T. (2001). Experimentally determined partition coefficients for minor and trace elements in peridotite minerals and carbonatitic melt, and their relevance to natural carbonatites. *European Journal of Mineralogy* **13**, 815–827.

Amundsen, H. E. F. (1987). Evidence for liquid immiscibility in the upper mantle. *Nature* **327**, 692–695.

Amundsen, H. E. F., Griffin, W. L. & O'Reilly, S. Y. (1987). The lower crust and upper mantle beneath northwestern Spitsbergen: evidence from xenoliths and geophysics. *Tectonophysics* **139**, 169–185.

Beccaluva, L., Bianchini, G., Coltorti, M., Perkins, W. T., Siena, F., Vaccaro, C. & Wilson, M. (2001). Multistage evolution of the European lithospheric mantle: new evidence from Sardinian peridotite xenoliths. *Contributions to Mineralogy and Petrology* **142**, 284–297.

Bedini, R. M. & Bodinier, J.-L. (1999). Distribution of incompatible trace elements between the constituents of spinel peridotite xenoliths: ICP-MS data from the East African rift. *Geochimica et Cosmochimica Acta* **63**, 3883–3900.

Bedini, R. M., Bodinier, J.-L., Dautria, J.-M. & Morten, L. (1997). Evolution of LILE-enriched small melt fractions in the lithospheric mantle: a case study from the East African Rift. *Earth and Planetary Science Letters* **153**, 67–83.

Bernstein, S., Kelemen, P. B. & Brooks, C. K. (1998). Depleted spinel harzburgite xenoliths in Tertiary dykes from East Greenland: restites from high degree melting. *Earth and Planetary Science Letters* **154**, 219–233.

Blundy, J. D. & Dalton, J. A. (2000). Experimental comparison of trace element partitioning between clinopyroxene and melt in carbonate and silicate systems, and implications for mantle metasomatism. *Contributions to Mineralogy and Petrology* **139**, 356–371.

Blundy, J. D., Robinson, J. A. C. & Wood, B. J. (1998). Heavy REE are compatible in clinopyroxene on the spinel lherzolite solidus. *Earth and Planetary Science Letters* **160**, 493–504.

Blythe, A. E. & Kleinspehn, K. L. (1998). Tectonically versus climatically driven Cenozoic exhumation of the Eurasian plate margin, Svalbard: fission track analysis. *Tectonics* **17**, 621–639.

Bodinier, J. L., Vasseur, G., Vernières, J., Dupuy, C. & Fabriès, J. (1990). Mechanisms of mantle metasomatism: geochemical evidence from the Lherz orogenic peridotite. *Journal of Petrology* **31**, 597–628.

Bottazzi, P., Ottolini, L., Vannucci, R. & Zanetti, A. (1994). An accurate procedure for the quantification of rare earth elements in silicates. In: Benninghoven, A., Nihei, Y., Shimizu, R. & Werner, H. V. (eds) *Secondary Ion Mass Spectrometry, SIMS IX*. Chichester: John Wiley, pp. 413–416 and 927–930.

Bottazzi, P., Tiepolo, M., Vannucci, R., Zanetti, A., Brumm, R., Foley, S. F. & Oberti, R. (1999). Distinct site preferences for heavy and light LREE in amphibole and the prediction of $^{Amph/L}D_{REE}$. *Contributions to Mineralogy and Petrology* **137**, 36–45.

Boyd, F. R., Pokhilenko, N. P., Pearson, D. G., Mertzman, S. A., Sobolev, N. V. & Finger, L. W. (1997). Composition of the Siberian cratonic mantle: evidence from Udachnaya peridotite xenoliths. *Contributions to Mineralogy and Petrology* **128**, 228–246.

Brey, G. P. & Köhler, T. (1990). Geothermobarometry in four-phase lherzolites II. New thermobarometers, and practical assessment of existing thermobarometers. *Journal of Petrology* **31**, 1353–1378.

Churikova, T., Dorendorf, F. & Wörner, G. (2001). Sources and fluids in the mantle wedge below Kamchatka, evidence from across-arc geochemical variation. *Journal of Petrology* **42**, 1567–1593.

Crank, J. (1975). *Mathematics of Diffusion*, 2nd edn. Oxford: Oxford University Press.

Dalton, J. A. & Wood, B. J. (1993). The compositions of primary carbonate melts and their evolution through wallrock reaction in the mantle. *Earth and Planetary Science Letters* **119**, 511–525.

Dautria, J. M., Dupuy, C., Takherist, D. & Dostal, J. (1992). Carbonate metasomatism in the lithospheric mantle: the peridotitic xenoliths from a melilititic district of the Sahara Basin. *Contributions to Mineralogy and Petrology* **111**, 37–52.

Downes, H. (2001). Formation and modification of the shallow sub-continental lithospheric mantle: a review of geochemical evidence from ultramafic xenolith suites and tectonically emplaced ultramafic massifs of western and central Europe. *Journal of Petrology* **42**, 233–250.

Dupuy, C., Liotard, J. M. & Dostal, J. (1992). Zr/Hf fractionation in intraplate basaltic rocks: carbonate metasomatism in the mantle source. *Geochimica et Cosmochimica Acta* **56**, 2417–2423.

Eggins, S. M., Woodhead, J. D., Kinsley, L. P. J., Mortimer, G. E., Sylvester, P., McCulloch, M. T., Hergt, J. M. & Handler, M. R. (1997). A simple method for the precise determination of ≥40 trace elements in geological samples by ICP-MS using enriched isotope internal stardardisation. *Chemical Geology* **134**, 311–326.

Eggins, S. M., Rudnick, R. L. & McDonough, W. F. (1998). The composition of peridotites and their minerals: a laser ablation ICP-MS study. *Earth and Planetary Science Letters* **154**, 53–71.

Eggler, D. H. (1989). Carbonatites, primary melts, and mantle dynamics. In: Bell, K. (ed.) *Carbonatites: Genesis and Evolution.* London: Unwin Hyman, pp. 561–579.

Elthon, D. (1992). Chemical trends in abyssal peridotites: refertilization of depleted suboceanic mantle. *Journal of Geophysical Research* **97**, 9015–9025.

Foley, S. F., Jackson, S. E., Fryer, B. J., Greenough, J. D. & Jenner, G. A. (1996). Trace element partition coefficients for clinopyroxene and phlogopite in an alkaline lamprophyre from Newfoundland by LAM-ICP-MS. *Geochimica et Cosmochimica Acta* **60**, 629–638.

Forsythe, L. M., Nielsen, R. L. & Fisk, M. R. (1994). High-field-strength element partitioning between pyroxene and basaltic to dacitic magmas. *Chemical Geology* **117**, 107–125.

Frey, F. A. & Green, D. H. (1974). The mineralogy, geochemistry and origin of lherzolite inclusions in Victorian basanites. *Geochimica et Cosmochimica Acta* **38**, 1023–1059.

Frey, F. A. & Prinz, M. (1978). Ultramafic inclusions from San Carlos, Arizona: petrologic and geochemical data bearing on their petrogenesis. *Earth and Planetary Science Letters* **38**, 129–176.

Frey, F. A., Suen, C. J. & Stockman, H. W. (1985). The Ronda high temperature peridotite: geochemistry and petrogenesis. *Geochimica et Cosmochimica Acta* **49**, 2469–2491.

Furnes, H., Pedersen, R. B. & Maaloe, S. (1986). Petrology and geochemistry of spinel peridotite nodules and host basalt, Vestspitsbergen. *Norsk Geologisk Tidsskrift* **66**, 53–68.

Galer, S. J. G. & O'Nions, R. K. (1989). Chemical and isotopic studies of ultramafic inclusions from the San Carlos volcanic field, Arizona: a bearing on their petrogenesis. *Journal of Petrology* **30**, 1033–1064.

Garrido, C. J., Bodinier, J.-L. & Alard, O. (2000). Incompatible trace element partitioning and residence in anhydrous spinel peridotites and websterites from the Ronda orogenic peridotite. *Earth and Planetary Science Letters* **181**, 341–358.

Genshaft, Y. S. & Ilupin, I. P. (1987). Mineralogy of Quaternary volcanic rocks from Spitsbergen. *Transactions (Doklady) USSR Academy of Sciences: Earth Science Section* **295**, 168–173.

Genshaft, Y. S., Dashevskaya, D. M., Yevdokimov, A. M. & Kopylova, M. G. (1992). Abundance and shape of plutonic ultramafic inclusions in alkalic basalt from Spitsbergen. *Transactions (Doklady) Russian Academy of Sciences: Earth Science Section* **326**, 116–122.

Godard, M., Bodinier, J.-L. & Vasseur, G. (1995). Effects of mineralogical reactions on trace element redistributions in mantle rocks during percolation processes: a chromatographic approach. *Earth and Planetary Science Letters* **133**, 449–461.

Green, D. H. & Wallace, M. E. (1988). Mantle metasomatism by ephemeral carbonatite melts. *Nature* **336**, 459–462.

Green, T. H. (1995). Experimental versus natural two-mineral partition coefficients: a 'high-tech' controversy. *International Geology Review* **37**, 851–865.

Hamilton, D. L., Bedson, P. & Esson, J. (1989). The behaviour of trace elements in the evolution of carbonatites. In: Bell, K. (ed.) *Carbonatites: Genesis and Evolution.* London: Unwin Hyman, pp. 405–427.

Hart, S. R. & Dunn, T. (1993). Experimental cpx/melt partitioning of 24 trace elements. *Contributions to Mineralogy and Petrology* **113**, 1–8.

Hauri, E. H. & Hart, S. R. (1994). Constraints on melt migration from mantle plumes: a trace element study of peridotite xenoliths from Savai'i, Western Samoa. *Journal of Geophysical Research* **99**, 24301–24321.

Hauri, E. H., Shimizu, N., Dieu, J. J. & Hart, S. R. (1993). Evidence for hotspot-related carbonatite metasomatism in the oceanic upper mantle. *Nature* **365**, 221–227.

Hauri, E. H., Wagner, T. P. & Grove, T. L. (1994). Experimental and natural partitioning of Th, U, Pb and other trace elements between garnet, clinopyroxene and basaltic melts. *Chemical Geology* **117**, 149–166.

Hellebrand, E., Snow, J. E., Dick, H. J. B. & Hofmann, A. W. (2001). Coupled major and trace elements as indicators of the extent of melting in mid-ocean-ridge peridotites. *Nature* **410**, 677–681.

Hofmann, A. W. (1988). Chemical differentiation of the Earth: the relationship between mantle, continental crust, and oceanic crust. *Earth and Planetary Science Letters* **90**, 297–314.

Hunter, R. H. & McKenzie, D. (1989). The equilibrium geometry of carbonate melts in rocks of mantle composition. *Earth and Planetary Science Letters* **92**, 347–356.

Ionov, D. A. (1986). Spinel peridotite xenoliths from the Shavaryn-Tsaram volcano, northern Mongolia: petrography, major element chemistry and mineralogy. *Geologicky Zbornik—Geologica Carpathica* **37**, 681–692.

Ionov, D. A. (1998). Trace element composition of mantle-derived carbonates and coexisting phases in peridotite xenoliths from alkali basalts. *Journal of Petrology* **39**, 1931–1941.

Ionov, D. A. & Harmer, R. E. (2002). Trace element distribution in calcite–dolomite carbonatites from Spitskop: inferences for differentiation of carbonatite magmas and the origin of carbonates in mantle xenoliths. *Earth and Planetary Science Letters* **198**, 495–510.

Ionov, D. A. & Hofmann, A. W. (1995). Nb–Ta-rich mantle amphiboles and micas: implications for subduction-related metasomatic trace element fractionations. *Earth and Planetary Science Letters* **131**, 341–356.

Ionov, D. A., Ashchepkov, I. V., Stosch, H.-G., Witt-Eickschen, G. & Seck, H. A. (1993*a*). Garnet peridotite xenoliths from the Vitim volcanic field, Baikal region: the nature of the garnet–spinel peridotite transition zone in the continental mantle. *Journal of Petrology* **34**, 1141–1175.

Ionov, D. A., Dupuy, C., O'Reilly, S. Y., Kopylova, M. G. & Genshaft, Y. S. (1993*b*). Carbonated peridotite xenoliths from Spitsbergen: implications for trace element signature of mantle carbonate metasomatism. *Earth and Planetary Science Letters* **119**, 283–297.

Ionov, D. A., Hofmann, A. W. & Shimizu, N. (1994). Metasomatism-induced melting in mantle xenoliths from Mongolia. *Journal of Petrology* **35**, 753–785.

Ionov, D. A., Prikhod'ko, V. S. & O'Reilly, S. Y. (1995). Peridotite xenoliths from the Sikhote-Alin, south-eastern Siberia, Russia: trace element signatures of mantle beneath a convergent continental margin. *Chemical Geology* **120**, 275–294.

Ionov, D. A., O'Reilly, S. Y., Kopylova, M. G. & Genshaft, Y. S. (1996). Carbonate-bearing mantle peridotite xenoliths from Spitsbergen: phase relationships, mineral compositions and trace element residence. *Contributions to Mineralogy and Petrology* **125**, 375–392.

Ionov, D. A., Grégoire, M. & Prikhod'ko, V. S. (1999*a*). Feldspar–Ti-oxide metasomatism in off-cratonic continental and oceanic upper mantle. *Earth and Planetary Science Letters* **165**, 37–44.

Ionov, D. A., O'Reilly, S. Y. & Griffin, W. L. (1999*b*). Off-cratonic garnet and spinel peridotite xenoliths from Dsun-Bussular, SE Mongolia. In: Gurney, J. J., Gurney, J. L., Pascoe, M. D. & Richardson, S. H. (eds) *Proceedings of the 7th International Kimberlite Conference.* Cape Town: Red Roof Design, pp. 383–390.

Ionov, D. A., Mukasa, S. B. & Bodinier, J.-L. (2002). Sr–Nd–Pb isotopic compositions of peridotite xenoliths from Spitsbergen: numerical modelling indicates Sr–Nd decoupling in the mantle by melt percolation metasomatism. *Journal of Petrology* **43**, 2261–2278.

Ionov, D. A., Savoyant, L. & Dupuy, C. (1992). Application of the ICP-MS technique to trace element analysis of peridotites and their minerals. *Geostandards Newsletter* **16**, 311–315.

Johnson, K. E., Davis, A. M. & Bryndzia, L. T. (1996). Contrasting styles of hydrous metasomatism in the upper mantle: an ion probe investigation. *Geochimica et Cosmochimica Acta* **60**, 1367–1385.

Johnson, K. T. M. (1998). Experimental determination of partition coefficients for rare earth and high-field-strength elements between clinopyroxene, garnet, and basaltic melt at high pressures. *Contributions to Mineralogy and Petrology* **133**, 60–68.

Johnson, K. T. M., Dick, H. J. B. & Shimizu, N. (1990). Melting in the oceanic upper mantle: an ion probe study of diopsides in abyssal peridotites. *Journal of Geophysical Research* **95**, 2661–2678.

Kalfoun, F., Ionov, D. A. & Merlet, C. (2002). HFSE residence and Nb–Ta ratios in metasomatised, rutile-bearing mantle peridotites. *Earth and Planetary Science Letters* **199**, 49–65.

Kelemen, P. B. (1990). Reaction between ultramafic wall rock and fractionating basaltic magma: Part I, Phase relations, the origin of calc-alkaline magma series, and the formation of discordant dunite. *Journal of Petrology* **31**, 51–98.

Kelemen, P. B., Dick, H. J. & Quick, J. E. (1992). Formation of harzburgite by pervasive melt/rock reaction in the upper mantle. *Nature* **358**, 635–641.

Kempton, P. D. (1987). Mineralogic and geochemical evidence for differing styles of metasomatism in spinel lherzolite xenoliths: enriched mantle source regions of basalts? In: Menzies, M. A. & Hawkesworth, C. J. (eds) *Mantle Metasomatism.* London: Academic Press, pp. 45–89.

Kempton, P. D., Hawkesworth, C. J., Lopez-Escobar, L., Pearson, D. G. & Ware, A. J. (1999). Spinel ± garnet lherzolite xenoliths from Pali Aike, Part 2: Trace element and isotopic evidence on the evolution of lithospheric mantle beneath southern Patagonia. In: Gurney, J. J., Gurney, J. L., Pascoe, M. D. & Richardson, S. H. (eds) *Proceedings of the 7th International Kimberlite Conference.* Cape Town: Red Roof Design, pp. 415–428.

Laurora, A., Mazzucchelli, M., Rivalenti, G., Vannucci, R., Zanetti, A., Barbieri, M. A. & Cingolani, C. A. (2001). Metasomatism and melting in carbonated peridotite xenoliths from the mantle wedge: the Gobernador Gregores case (southern Patagonia). *Journal of Petrology* **42**, 69–87.

Lee, W.-J. & Wyllie, P. J. (1998). Processes of crustal carbonatite formation by liquid immiscibility and differentiation, elucidated by model systems. *Journal of Petrology* **39**, 2005–2013.

Lenoir, X., Garrido, C. J., Bodinier, J.-L. & Dautria, J.-M. (2000). Contrasting lithospheric mantle domains beneath the Massif Central (France) revealed by geochemistry of peridotite xenoliths. *Earth and Planetary Science Letters* **181**, 359–375.

Lundstrom, C. C., Shaw, H. F., Ryerson, F. J., Williams, Q. & Gill, J. (1998). Crystal chemical control of clinopyroxene–melt partitioning in the Di–Ab–An system: implications for elemental fractionations in the depleted mantle. *Geochimica et Cosmochimica Acta* **62**, 2849–2862.

Makishima, A. & Nakamura, E. (1997). Suppression of matrix effects in ICP-MS high power operation of ICP: application to precise determination of Rb, Sr, Y, Cs, Ba, REE, Pb, Th, and U at ng g^{-1} levels in milligram silicate samples. *Geostandards Newsletter* **21**, 307–319.

Mattielli, N., Weis, D., Scoates, J. S., Shimizu, N., Mennessier, J.-P., Grégoire, M., Cottin, J.-Y. & Giret, A. (1999). Evolution of heterogeneous lithospheric mantle in a plume environment beneath the Kerguelen Archipelago. *Journal of Petrology* **40**, 1721–1744.

McDonough, W. F. (1990). Constraints on the composition of the continental lithospheric mantle. *Earth and Planetary Science Letters* **101**, 1–18.

McDonough, W. F. & Frey, F. A. (1989). Rare earth elements in upper mantle rocks. In: Lipin, B. R. & McKay, G. A. (eds) *Geochemistry and Mineralogy of Rare Earth Elements.* Washington, DC: Mineralogical Society of America, pp. 99–145.

McKenzie, D. (1989). Some remarks of the movement of small melt fractions in the mantle. *Earth and Planetary Science Letters* **95**, 53–72.

Menzies, M. A. & Hawkesworth, C. J. (1987). Upper mantle processes and composition. In: Nixon, P. H. (ed.) *Mantle Xenoliths.* Chichester: John Wiley, pp. 725–738.

Mukasa, S. B. & Wilshire, H. G. (1997). Isotopic and trace element compositions of upper mantle and lower crustal xenoliths, Cima volcanic field, California: implications for evolution of the subcontinental lithospheric mantle. *Journal of Geophysical Research* **102**, 20133–20148.

Nakamura, E., Campbell, I. H. & Sun, S.-S. (1985). The influence of subduction processes on the geochemistry of Japanese alkaline basalts. *Nature* **316**, 55–58.

Navon, O. & Stolper, E. (1987). Geochemical consequences of melt percolation: the upper mantle as a chromatographic column. *Journal of Geology* **95**, 285–307.

Navon, O., Frey, F. A. & Takazawa, E. (1996). Magma transport and metasomatism in the mantle: a critical review of current geochemical models—Discussion. *American Mineralogist* **81**, 754–759.

Nelson, D. R., Chivas, A. R., Chappell, B. W. & McCulloch, M. T. (1988). Geochemical and isotopic systematics in carbonatites and implications for the evolution of ocean-island sources. *Geochimica et Cosmochimica Acta* **52**, 1–17.

Nielson, J. E. & Wilshire, H. G. (1993). Magma transport and metasomatism in the mantle: a critical review of current geochemical models. *American Mineralogist* **78**, 1117–1134.

Niida, K. & Green, D. H. (1999). Stability and chemical composition of pargasitic amphibole in MORB pyrolite under upper mantle conditions. *Contributions to Mineralogy and Petrology* **135**, 18–40.

Niu, Y. (1997). Mantle melting and melt extraction processes beneath ocean ridges: evidence from abyssal peridotites. *Journal of Petrology* **38**, 1047–1074.

Norman, M. D., Pearson, N. J., Sharma, A. & Griffin, W. L. (1996). Quantitative analysis of trace elements in geological materials by laser ablation ICPMS: instrumental operating conditions and calibration values of NIST glasses. *Geostandards Newsletter* **20**, 247–261.

Press, S., Witt, G., Seck, H. A., Ionov, D. A. & Kovalenko, V. I. (1986). Spinel peridotite xenoliths from the Tariat Depression, Mongolia. I: Major element chemistry and mineralogy of a primitive mantle xenolith suite. *Geochimica et Cosmochimica Acta* **50**, 2587–2599.

Rampone, E., Bottazzi, P. & Ottolini, L. (1991). Complementary Ti–Zr anomalies in orthopyroxene and clinopyroxene in mantle peridotites. *Nature* **354**, 518–520.

Rudnick, R. L., McDonough, W. F. & Chappell, B. C. (1993). Carbonatite metasomatism in the northern Tanzanian mantle. *Earth and Planetary Science Letters* **114**, 463–475.

Sachtleben, T. & Seck, H. A. (1981). Chemical control of Al-solubility in orthopyroxene and its implications on pyroxene geothermometry. *Contributions to Mineralogy and Petrology* **78**, 157–165.

Skulski, T., Minarik, W. & Watson, E. B. (1994). High-pressure experimental trace-element partitioning between clinopyroxene and basaltic melts. *Chemical Geology* **117**, 127–147.

Sneeringer, M., Hart, S. R. & Shimizu, N. (1984). Strontium and samarium diffusion in diopside. *Geochimica et Cosmochimica Acta* **48**, 1589–1608.

Stosch, H.-G. & Lugmair, G. W. (1986). Trace element and Sr and Nd isotope geochemistry of peridotite xenoliths from the Eifel (West Germany) and their bearing on the evolution of the subcontinental lithosphere. *Earth and Planetary Science Letters* **80**, 281–298.

Streckeisen, A. (1976). To each plutonic rock its proper name. *Earth-Science Reviews* **12**, 1–33.

Sun, S. S. & McDonough, W. F. (1989). Chemical and isotopic systematics of oceanic basalts: implications for mantle composition and processes. In: Saunders, A. D. & Norry, M. J. (eds) *Magmatism*

in the Ocean Basins. Geological Society, London, Special Publications **42**, 313–345.

Sweeney, R. J. (1994). Carbonatite melt compositions in the Earth's mantle. *Earth and Planetary Science Letters* **128**, 259–270.

Takazawa, E., Frey, F. A., Shimizu, N. & Obata, M. (2000). Whole rock compositional variations in an upper mantle peridotite (Horoman, Hokkaido, Japan): are they consistent with a partial melting process? *Geochimica et Cosmochimica Acta* **64**, 695–716.

Takazawa, E., Frey, F. A., Shimizu, N., Obata, M. & Bodinier, J. L. (1992). Geochemical evidence for melt migration and reaction in the upper mantle. *Nature* **359**, 55–58.

Tiepolo, M., Vannucci, R., Bottazzi, P., Oberti, R., Zanetti, A. & Foley, S. (2000*a*). Partitioning of rare earth elements, Y, Th, U, and Pb between pargasite, kaersutite, and basanite to trachyte melts: implications for percolated and veined mantle. *Geochemistry, Geophysics, Geosystems* **1**, Paper 2000GC000064.

Tiepolo, M., Vannucci, R., Oberti, R., Foley, S., Bottazzi, P. & Zanetti, A. (2000*b*). Nb and Ta incorporation and fractionation in titanian pargasite and kaersutite: crystal-chemical constraints and implications for natural systems. *Earth and Planetary Science Letters* **176**, 185–201.

Tiepolo, M., Bottazzi, P., Foley, S., Oberti, R., Vannucci, R. & Zanetti, A. (2001). Fractionation of Nb and Ta from Zr and Hf at mantle depths: the role of titanian pargasite and kaersutite. *Journal of Petrology* **42**, 221–232.

Van der Wal, D. & Bodinier, J.-L. (1996). Origin of the recrystallisation front in the Ronda peridotite by km-scale pervasive porous melt flow. *Contributions to Mineralogy and Petrology* **122**, 387–405.

Vannucci, R., Bottazzi, P., Wulff-Pedersen, E. & Neumann, E.-R. (1998). Partitioning of REE, Y, Sr, Zr and Ti between clinopyroxene and silicate melts in the mantle under La Palma (Canary Islands): implications for the nature of the metasomatic agents. *Earth and Planetary Science Letters* **158**, 39–51.

Vasseur, G., Vernières, J. & Bodinier, J.-L. (1991). Modeling of trace element transfer between mantle melt and heterogranular peridotite matrix. *Journal of Petrology Special Volume*, 41–54.

Veksler, I. V., Petibon, C., Jenner, G. A., Dorfman, A. M. & Dingwell, D. B. (1998). Trace element partitioning in immiscible silicate–

carbonate liquid systems: an initial experimental study using a centrifuge autoclave. *Journal of Petrology* **39**, 2095–2104.

Vernières, J., Godard, M. & Bodinier, J.-L. (1997). A plate model for the simulation of trace element fractionation during partial melting and magma transport in the Earth's upper mantle. *Journal of Geophysical Research* **102**, 24771–24784.

Wells, P. R. A. (1977). Pyroxene thermometry in simple and complex systems. *Contributions to Mineralogy and Petrology* **62**, 129–139.

Wiechert, U., Ionov, D. A. & Wedepohl, K. H. (1997). Spinel peridotite xenoliths from the Atsagin-Dush volcano, Dariganga lava plateau, Mongolia: a record of partial melting and cryptic metasomatism in the upper mantle. *Contributions to Mineralogy and Petrology* **126**, 345–364.

Woodhead, J. D. (1989). Geochemistry of the Mariana arc (western Pacific): source composition and processes. *Chemical Geology* **76**, 1–24.

Woolley, A. R. & Kempe, D. R. C. (1989). Carbonatites: nomenclature, average chemical composition, and element distribution. In: Bell, K. (ed.) *Carbonatites: Genesis and Evolution*. London: Unwin Hyman, pp. 1–14.

Yaxley, G. M., Crawford, A. J. & Green, D. H. (1991). Evidence for carbonatite metasomatism in spinel peridotite xenoliths from western Victoria, Australia. *Earth and Planetary Science Letters* **107**, 305–317.

Yaxley, G. M., Kamenetsky, V., Green, D. H. & Falloon, T. J. (1997). Glasses in mantle xenoliths from western Victoria, Australia, and their relevance to mantle processes. *Earth and Planetary Science Letters* **148**, 433–446.

Yaxley, G. M., Green, D. H. & Kamenetsky, V. (1998). Carbonate metasomatism in the southeastern Australian lithosphere. *Journal of Petrology* **39**, 1917–1931.

Yevdokimov, A. N. (2000). *Volcanoes of Spitsbergen*. St Petersburg: VNIIOkeangeologija (in Russian with English abstract).

Zanetti, A., Vannucci, R., Bottazzi, P., Oberti, R. & Ottolini, L. (1996). Infiltration metasomatism at Lherz as monitored by systematic ion-microprobe investigations close to a hornblendite vein. *Chemical Geology* **134**, 113–133.

Zanetti, A., Mazzucchelli, M., Rivalenti, G. & Vannucci, R. (1999). The Finero phlogopite–peridotite massif: an example of subduction-related metasomatism. *Contributions to Mineralogy and Petrology* **134**, 107–122.